Telecom Wavelength Quantum Devices

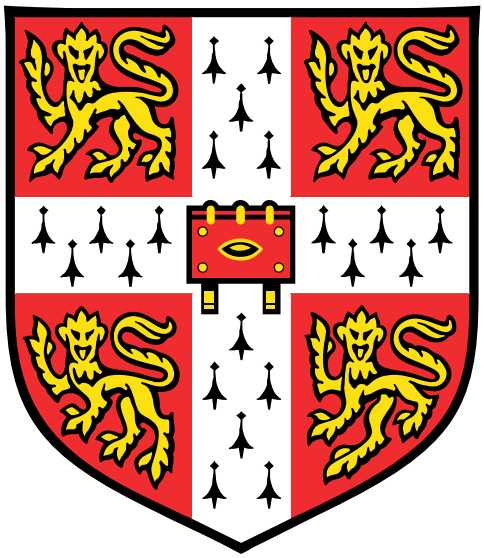

Martin Connor Patrick Felle

Darwin College

This dissertation is submitted for the degree of *Doctor of Philosophy* June 2017

Declaration

This thesis describes work carried out in the Semiconductor Physics Group at the Cavendish Laboratory of the University of Cambridge and the Cambridge Research Laboratory of Toshiba Research Europe Limited, as a member of the Centre for Photonic Systems of the University of Cambridge and the EPSRC Doctoral Training Centre for Photonic Systems Development, from October 2013 to November 2016.

This dissertation is the result of my own work and contains nothing which is the outcome of work done in collaboration except where specifically indicated in the text. It has not been submitted in part, or as a whole, for any degree at this, or any other, university. It does not exceed 60,000 words.

Publications

Articles

M. Felle, J. Huwer, R. M. Stevenson, J. Skiba-Szymanska, M. B. Ward, I. Farrer, R. V. Penty, D. A. Ritchie, and A. J. Shields, *Interference with a quantum dot single-photon source and a laser at telecom wavelength*, Applied Physics Letters, vol. 107, no. 13, 2015.

J. Huwer, M. Felle, R. M. Stevenson, J. Skiba-Szymanska, M. B. Ward, I. Farrer, R. V. Penty, D. A. Ritchie, and A. J. Shields, *Quantum-Dot-Based Telecommunication-Wavelength Quantum Relay*, Physical Review Applied 8, 024007, 2017.

J. Skiba-Szymanska, R. M. Stevenson, C. Varnava, M. Felle, J. Huwer, T. Müller, A. J. Bennet, J. Lee, I. Farrer, A. Krysa, P. Spencer, L. Goff, D. A. Ritchie, J. Heffernan, A. J. Shields, *Universal Growth Scheme for Quantum Dots with Low Fine-Structure Splitting at Various Emission Wavelengths*, Physical Review Applied 8, 014013, 2017.

T. Müller, J. Skiba-Szymanska, A. B. Krysa, J. Huwer, M. Felle, M. Anderson, R. M. Stevenson, J. Heffernan, D. A. Ritchie, and A. J. Shields, *A quantum light emitting diode for the standard telecom window around 1550 nm*, accepted for publication in Nature Communications, 2017.

R. Al-Khuzheyri, A. C. Dada, J. Huwer, T. S. Santana, J. Skiba-Szymanska, M. Felle, M. B. Ward, R. M. Stevenson, I. Farrer, M. G. Tanner, R. H. Hadfield, D. A. Ritchie, A. J. Shields, B. D. Gerardot, *Resonance fluorescence from a telecom-wavelength quantum dot*, Applied Physics Letters, vol. 109, no. 16, 2016.

M. Sharma, M. K. Sanyal, I. Farrer, D. A. Ritchie, A. B. Dey, A. Bhattacharyya, O. H. Seeck, J. Skiba-Szymanska, M. Felle, A. J. Bennett, A. J Shields, *Density dependent composition of InAs quantum dots extracted from grazing incidence x-ray diffraction measurements*, Scientific Reports, vol. 5, 2015.

Conference contributions

M. Felle, J. Huwer, R. M. Stevenson, J. Skiba-Szymanska, C. Varnava, M. B. Ward, I. Farrer, R. V. Penty, D. A. Ritchie, and A. J. Shields, *Quantum dots as sources of coherent entangled photons at telecommunication wavelengths*, International Conference on the Physics of Semiconductors, 1-5 August 2016, Beijing, China (Talk).

M. Felle, J. Huwer, R. M. Stevenson, J. Skiba-Szymanska, M. B. Ward, I. Farrer, R. V. Penty, D. A. Ritchie, and A. J. Shields, *Interference between a Quantum Dot Single-Photon Source and a Telecom-Wavelength Laser*, Conference on Modulated Semiconductor Structures, 26-31 July 2015, Sendai, Japan (Poster).

M. Felle, J. Huwer, R. M. Stevenson, C. Varnava, J. Skiba-Szymanska, M. B. Ward, I. Farrer, D. A. Ritchie, R. V. Penty, and A. J. Shields, *Quantum Devices at Telecom Wavelengths*, Quantum Cambridge Winter School, 21-22 March 2015, Oxford, UK (Talk).

Acknowledgements

There are a great number of people to whom I owe a debt of gratitude for the material of this thesis. Firstly, I'd like to thank Dr. Jan Huwer of Toshiba Research Europe Ltd (TREL) for his ongoing support and guidance. It was a pleasure to work with Jan on the quantum relay project and I doubt we would have had a tenth of the success we had without his contagious work ethic and broad expertise. To Dr. Mark Stevenson, also of TREL, with his depths of research experience and bottomless curiosity, I thank for teaching me a great deal and always steering our projects towards success. To my Supervisors, Dr. Andrew Shields of TREL and Prof. Richard Penty of the University of Cambridge, I thank for providing overarching support of and guidance of my research, and Prof. David Ritchie of the University of Cambridge, I thank for happily opening the doors to the Semiconductor Physics Group's labs and cleanroom.

I also owe considerable thanks to Dr. Joanna Skiba-Szymanska, Dr. Martin Ward, and Dr. Tina Müller of TREL for being ever-present sources of knowledge and support. Christiana Varnava, I thank for coaching me in the early days of my PhD, and for being a notably above-par desk mate in later days. To the rest of the researchers and PhD students of the Cambridge Research Lab, including Lucian, Fred, Jamie, Yarden, George, Bruno, and Alex K., thanks for all the help and interesting conversations that made the labs a great place to work.

Naturally, without the support of friends and family, the years of a PhD would be very difficult. I give thanks to my mother, Teresa, whose pride has fueled me to complete this work, and my siblings Tessa, Emma, and Declan, who all took it on faith that I was doing interesting and important work. I must thank Nathan and Alex M., for being spectacularly easy-going housemates for the course of our respective projects. Finally, I offer special thanks to my partner Anne Miquel, who, apart from teaching me some of the basic life skills that aren't learned in a PhD, was a constant source of support throughout the writing of this thesis.

Summary

Semiconductor quantum dots (QDs) are well established as sub-Poissonian sources of entangled photon pairs. To improve the utility of a QD light source, it would be advantageous to extend their emission further into the near infrared, into the low absorption wavelength windows utilised in long-haul optical telecommunication.

Initial experiments succeeded in interfering O-band (1260—1360 nm) photons from an InAs/GaAs QD with dissimilar photons from a laser, an important mechanism for quantum teleportation. Interference visibilities as high as 60 ± 6 % were recorded, surpassing the 50 % threshold imposed by classical electrodynamics. Later, polarisation-entanglement of a similar QD was observed, with pairs of telecom-wavelength photons from the radiative cascade of the biexciton state exhibiting fidelities of 92.0 ± 0.2 % to the Φ^- Bell state.

Subsequently, an O-band telecom-wavelength quantum relay was realised. Again using an InAs/GaAs QD device, this represents the first implementation of a sub-Poissonian telecom-wavelength quantum relay, to the best knowledge of the author. The relay proved capable of implementing the famous four-state BB84 protocol[1], with a mean teleportation fidelity as high as 94.5 ± 2.2 %, which would contribute 0.385 secure bits per teleported qubit. After characterisation by way of quantum process tomography[2,3], the performance of the relay was also evaluated to be capable of implementing a six-state QKD protocol.

In an effort to further extend the emitted light from a QD into the telecom C-band (1530—1565 nm), alternative material systems were investigated. InAs QDs on a substrate of InP were shown to emit much more readily in the fibre-telecom O- and C-bands than their InAs/GaAs counterparts, largely due to the reduced lattice mismatch between the QD and substrate for InAs/InP (~3 %) compared to InAs/GaAs (~7 %). Additionally, to minimize the fine structure splitting (FSS) of the exciton level, which deteriorates the observed polarisation-entanglement, a new mode of dot growth was investigated. Known as droplet epitaxy (D-E), QDs grown in this mode showed a fourfold reduction in the FSS compared to dots grown in the Stranski-Krastanow mode. This improvement would allow observation of polarisation-entanglement in the telecom C-band. In subsequent work performed by colleagues at the Toshiba Cambridge Research Labs, these D-E QDs were embedded in a *p-i-n* doped optical cavity, processed with electrical contacts, and found to emit entangled pairs of photons under electrical excitation.

The work of this thesis provides considerable technological advances to the field of entangled-light sources, that in the near future may allow for deterministic quantum repeaters operating at megahertz rates, and in the further future could facilitate the distribution of coherent multipartite states across a distributed quantum network[4].

List of abbreviations

APD	Avalanche photodiode
(P)BS	(Polarising) Beamsplitter
BSM	Bell state measurement
C-band	Conventional band (1530-1565 nm)
CHSH	Clauser-Horne-Shimony-Holt
CW	Continuous-wave
D-E	Droplet epitaxy
DM	Dichroic mirror
(μ)EL	(micro-)Electroluminescence
EPC	Electronic polarisation controller
FSS	Fine structure splitting
GaAs	Gallium Arsenide
HBT	Hanbury Brown and Twiss
HWP	Half-wave plate
InAs	Indium Arsenide
InP	Indium Phosphide
(μ)L	(micro-)Luminescence
(E)LED	(Entangled-)Light emitting diode
LP	Linear polarizer
MBE	Molecular beam epitaxy
MM	Movable mirror
MOVPE	Metalorganic vapour phase epitaxy
MZ	Mach-Zehnder
NA	Numerical aperture
O-band	Original band (1260-1360 nm)
(μ)PL	(micro-)Photoluminescence
QC	Quantum channel
QD	Quantum Dot
QND	Quantum non-demolition
QKD	Quantum key distribution
QWP	Quarter-wave plate
S-K	Stranski-Krastanow
SNSPD	Superconducting nanowire single photon detector
TDG	Transmission diffraction grating

TPI	Two-photon interference
WDM	Wavelength-division multiplexing
X	Neutral exciton
XX	Neutral biexciton
$X^{*/+/-}$	Charged exciton (with charge +e, -e, or unknown [*])

Contents

1 Introduction 1

1.1 Motivation 1

1.2 Statistics of single photon sources 3

1.3 Semiconductor quantum dots 6

1.4 Experimental techniques 9

1.4.1 Micro-luminescence 9

1.4.2 Spectroscopy 11

1.4.3 Time-correlated measurements 11

1.5 Thesis Outline 12

2 Two-Photon Interference 13

2.1 Introduction 13

2.2 Modelling interference 15

2.2.1 Single-photon interference 15

2.2.2 Two-photon interference 17

2.3 Experimental preparation 22

2.3.1 Quantum dot single photon source 22

2.3.2 The Mach-Zehnder interferometer 23

2.3.3 Single photon interferometry 26

2.3.4 Two-photon interference circuit 28

2.4 Results 30

2.5 Conclusions 33

3 Entanglement at Telecom Wavelengths 35

3.1 Introduction 35

3.2 Background 37

3.2.1 Modelling Entanglement 37

3.2.2 Measuring Entanglement 39

3.2.3 Quantifying entanglement 41

3.3 Entanglement source 42

3.3.1 Measuring fine structure splitting 43

3.3.2 Quantum dot selection 46

3.4 Observing Entanglement 48

3.4.1 Experimental setup 48

3.4.2 Entanglement excitation conditions 49

3.5 Time-evolving entanglement 52
3.5.1 Second-order polarisation cross-correlations 52
3.5.2 Entanglement fidelity 53
3.5.3 Violating Bell's theorem 55
3.6 Conclusions 56

4 Telecom-Wavelength Quantum Relay 57
4.1 Introduction 57
4.2 Background 59
4.2.1 Quantum teleportation 59
4.2.2 Realistic teleportation 60
4.2.3 Teleportation with a QD entanglement source 62
4.3 The Quantum Relay 66
4.4 BB84 Protocol 69
4.4.1 Teleporting control states 69
4.4.1.1 Teleporting eigenstates 70
4.4.1.2 Teleporting superposition states 72
4.4.1.3 Analysis 75
4.4.2 Teleporting detuned control states 77
4.5 Quantum Process Tomography 81
4.5.1 General prescription 81
4.5.2 Basis choices 82
4.5.3 Quantum state tomography 82
4.5.4 The process matrix 87
4.6 Conclusions 89

5 Quantum Dot Entangled-LED at 1.55 μm 91
5.1 Current state of the art 91
5.2 Stranski-Krastanow InAs/InP QDs 93
5.2.1 Growth optimization 93
5.3 Droplet Epitaxy Quantum Dots 96
5.3.1 Growth optimization 97
5.4 Intra-cavity quantum dots 99
5.4.1 Characterisation 100
5.5 Towards entanglement 102
5.5.1 Fine structure splitting survey 102
5.6 Electrical excitation 105

5.7 Entanglement from an LED 107
5.8 Conclusions 111
6 Conclusions 113
6.1 O-band quantum relay 113
6.2 C-band entangled LED 114
6.3 Future work 114
6.3.1 Improved entanglement 114
6.3.2 Improved Bell state analyser 116
6.3.3 A practical quantum relay 116
6.3.4 Entanglement swapping 117
Bibliography 119

1 Introduction

1.1 Motivation

The internet, most people will agree, is a pretty wonderful thing. It connects people across the globe, and promotes the spread of knowledge and collaboration at unprecedented levels. The strong sense of connectivity, however, is at odds with the necessity to privately share information. Recent years have seen an increase in the strength and complexity of cybercrime, ranging from theft of citizens' private health records, to stifling journalists around the globe.

The backbone of the internet's secret-sharing ability is the RSA scheme of public-key encryption[5], named for its inventors Ron Rivest, Adi Shamir, and Leonard Adleman, which allows messages encrypted by a publicly announced key to be decryptable only by the intended recipient. Communication channels of a classical network, with sufficient technical resources, can always be passively monitored, and attempts can be made to extract the secret key from the public key. However, with a key length of 2048 bits or longer the secrecy of your messages is all but guaranteed for the foreseeable future. As such, modern cybercrime techniques tend to rely on denial-of-service attacks, such as with a network of suborned devices, known as a "botnet", or tricking a user into revealing private information, a tactic known commonly as "phishing". Although advances in cryptanalysis and computing power may reduce the security of an RSA-encrypted message, secrecy can again be arbitrarily strengthened simply by increasing the length of the key.

A quantum computer[6,7] would be capable of utilising superposed and entangled combinations of computational basis states, known as quantum bits (qubits), allowing it access to a richer repertoire of algorithms than its classical counterpart. A quantum algorithm was put forth by Peter Shor in 1994[8], successfully tested experimentally[9–11], to find the prime factors of a number in polynomial time, rather than the roughly exponential time required for a classical algorithm. The security of RSA relies on the asymmetric computational difficulty between multiplying and factoring two numbers, so the implementation of a scalable quantum computer would fast render this scheme obsolete. This is not to say that the only use of a quantum computer is to hack into encrypted data. Another famous quantum algorithm proposed by Lov Grover in 1996[12], for example, allows a list of length n to be searched in time $\propto\sqrt{n}$, compared to time $\propto n$

classically, and has been tested experimentally[13,14], which would be of incredible use in sifting through large databases.

The science of quantum information, while introducing new difficulties to cryptography, also provides a range of new possibilities. Quantum systems, famously, cannot be observed without being disturbed[15]. If the bits of data are transmitted one quantum at a time in a randomly chosen basis, such a communication channel cannot be passively observed without the eavesdropper being discovered by the intended recipient. This family of schemes is known as quantum key distribution (QKD)[1], and allows for the provably secure sharing of a secret encryption key, guaranteed by the laws of physics[16,17]. Unfortunately, the no-cloning theorem[15] that guarantees this security also precludes the possibility of a signal amplifier, required for long-haul telecommunications, limiting the length of a realistic quantum channel to tens of kilometres[18,19], although lower key-rate quantum channels as long as 260 km[20] have been implemented.

A possible solution to this problem, by improving the signal-to-noise ratio of the transmitted quanta, could be through the implementation of quantum relays and quantum repeaters[21,22]. These components would require additional resources, namely sources of entangled and coherent photons, and for a repeater, a high-efficiency quantum memory. Additionally, to take advantage of the low attenuation C-band (~1550 nm[23]) and zero dispersion O-band (~1300 nm[24]) transmission windows in standard optical fibre, the photons would need to be at these wavelengths. Quantum metrology[25,26] would also benefit from such a source, especially in characterising the dynamics behind a distributed quantum network[4], where interaction between coherent and/or entangled telecommunication-wavelength photons and massive qubits are of particular interest.

Building on prior work at the Cambridge Research Labs of Toshiba Research Europe Ltd[27–29] the hope of this thesis was to develop and implement such a telecom-wavelength quantum relay. Through the use of optically excited semiconductor quantum dots as sources of entangled coherent telecom-wavelength photon pairs, a sub-Poissonian quantum relay operating at 1300 nm was successfully implemented for the first time. Quantum dots grown by an alternate mode of growth in a different semiconductor matrix, with morphology enabling the emission of entangled photon-pairs, were developed and demonstrated to emit in the telecom C-band with sub-Poissonian statistics. Both of these results represent significant technological advancements in telecom-wavelength quantum light sources.

1.2 Statistics of single photon sources

Important in a quantum channel are the statistics of the quanta being utilised. Consider a coherent continuous-wave (CW) light source, operating at constant intensity. Under standard operation, it would not be possible to resolve the arrival time of individual photons, since even for an optical power of 1 nW and a wavelength of 1000 nm, there would still be a photon flux of 5000 photons per nanosecond, and the technology behind THz-rate detection is in its infancy. However, by attenuating the source, and with a sufficiently time-resolved detector, one would start to see quantised events rather than a continuously large flux of photons. In a classical light source such as this, the creation of a photon is completely independent to the creation of any other photons before or after it, so the arrival time of photons will obey Poissonian statistics. That is, in a time interval where a mean number of photons μ would be expected, there is a probability P of there being n photons present, given by

$$P(n) = \frac{\mu^n e^{-\mu}}{n!} \tag{1.1}$$

Considering a 1 ns time interval in the above example. With an expected 5000 photons, there would be a one-sigma uncertainty of 70.7 photons. That is, 69 % of the time the photon flux will be within 1.4% of the desired number, which is reasonably precise. Smaller numbers increase the uncertainty, however. Having 1 photon per interval gives a $1/e \simeq 36.7$ % chance of observing no photons, and a $1\text{-}2/e \simeq 26.4$ % chance of observing two or more photons. In many quantum technologies, it is possible and sufficient to circumvent this problem of statistical uncertainty by using heralded single photon sources[30–32], where measurement of one half of a correlated photon pair signifies the existence of a single photon, without destroying the photon state. In general, however, deterministic light sources will be required, providing on-demand photon states with well-defined photon numbers [33].

In the absence of sufficiently fast photon number resolving detectors, a standard measure of a light source's statistical properties is the second-order autocorrelation function ($g^{(2)}$). This function is a measure of the probability of observing a photon at time τ after having observed a first photon.

$$g^{(2)}(\tau) = \frac{\langle I(t)I(t+\tau)\rangle}{\langle I(t)\rangle\langle I(t+\tau)\rangle} \tag{1.2}$$

where $I(t)$ is the time-dependent intensity of the light. Experimentally, this quantity can be observed by measuring a histogram of start-stop times between the output modes of a beamsplitter, where the light enters one of the input modes, in a setup such as described in Figure 1.1. Such an experiment was proposed by Hanbury Brown and Twiss in 1956[34], and allows the degree of 'bunching' in a beam of light to be quantized.

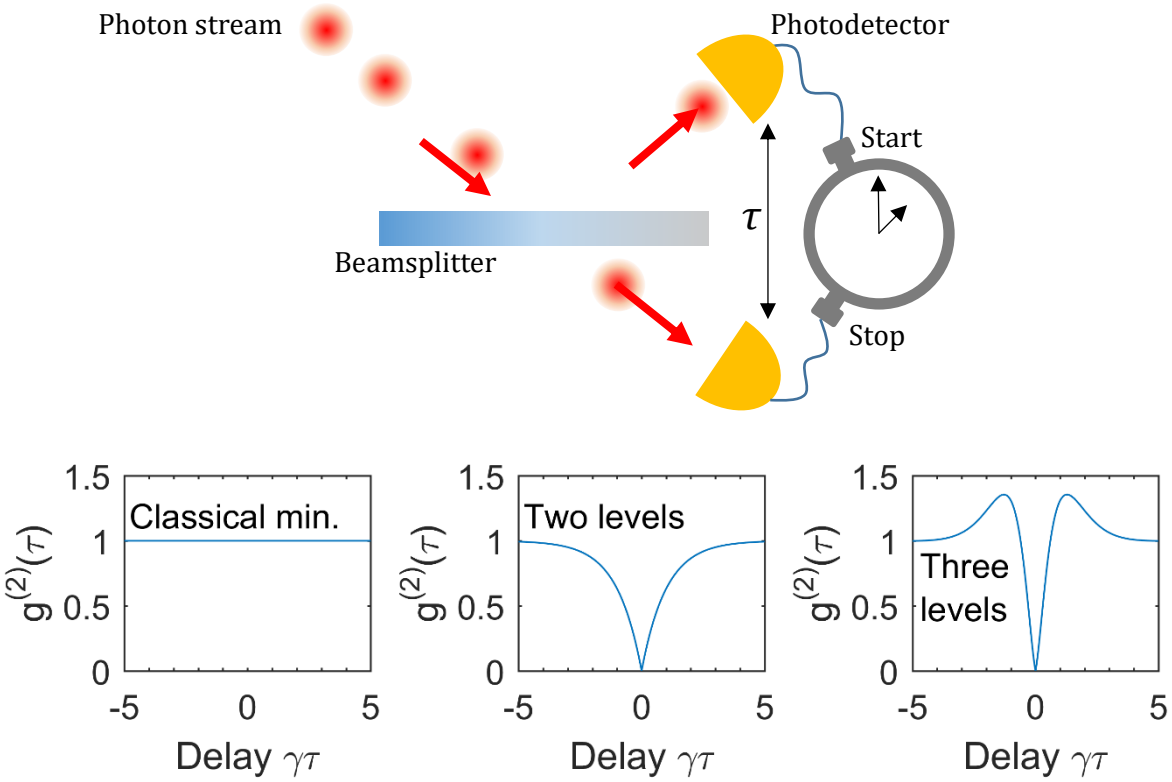

Figure 1.1: (Top) The Hanbury Brown and Twiss[34] configuration used to measure the second-order autocorrelation function ($g^{(2)}(\tau)$). (Bottom-left) The lower limit of $g^{(2)}(\tau)$ for a classical source, (bottom-centre) the $g^{(2)}(\tau)$ curve for a system of two energy levels, and (bottom-right) the $g^{(2)}(\tau)$ curve for a richer energy level structure.

Consider again the continuous wave source. $I(t)$ is constant, so $I(t) = I(t+\tau)$, and $g^{(2)}(\tau) = 1$. This can be shown to be the lowest that a classical CW source can go. In fact, $g^{(2)}(\tau) = 1$ only for a perfectly coherent source, while $g^{(2)}(\tau) > 1$ for any source with thermal or other effects coming into play.

In a quantum light source, however, the likelihood of emitting a photon is not independent of whether a photon has just been emitted, as a result of the Pauli's exclusion principle[35]. It is only possible to have a single radiative decay occur at any time in a non-degenerate system, and once a decay has happened, the source needs some finite time to be reexcited. Considering the quantum operators for the creation and destruction of photons, we come to the expression:

$$\begin{aligned} g^{(2)}(\tau) &= \frac{\langle I(t)I(t+\tau)\rangle}{\langle I(t)\rangle\langle I(t+\tau)\rangle} \\ &= \frac{\langle \hat{a}^\dagger(t)\hat{a}(t)\hat{a}^\dagger(t+\tau)\hat{a}(t+\tau)\rangle}{\langle \hat{a}^\dagger(t)\hat{a}(t)\rangle\langle \hat{a}^\dagger(t+\tau)\hat{a}(t+\tau)\rangle} \\ &= \frac{\langle \hat{n}(\tau)^2\rangle}{\langle \hat{n}(\tau)\rangle^2} \end{aligned} \tag{1.3}$$

where $\hat{a}^{\dagger}$ and $\hat{a}$ are the photon creation and annihilation operators, and $\hat{n}$ is the photon number operator. Suppose your photon is in a well-defined Fock state containing n photons, then at $\tau = 0$ the autocorrelation function will be

$$g^{(2)}(0) = \frac{n(n-1)}{n^2} \tag{1.4}$$

In the case of a simple two-level system, $g^{(2)}(\tau)$ can be expressed as

$$g^{(2)}(\tau) = 1 - \exp(-\gamma|\tau|) \tag{1.5}$$

where γ is related to the excitation rate and the radiative lifetime of the transition. Richer energy-level structures result in more complex $g^{(2)}(\tau)$ curves, as exemplified in Figure 1.1. Streams of photons where $g^{(2)}$ goes above 1 are said to be 'bunched', whereas streams with $g^{(2)} < 1$ are said to be 'antibunched'. Anti-bunching is a phenomenon exclusive to quantum light sources, and is important in guaranteeing the security and fidelity of many QKD and quantum computation schemes[6,7,33].

1.3 Semiconductor quantum dots

III-V semiconductor quantum dots (QDs)[36–40] have shown themselves to be good quantum light sources, demonstrating promise as sub-Poissonian sources of single photons and entangled photon pairs. Quantum dots are a family of three-dimensionally confined crystals of semiconductor, modifying the density of states such that only very specific phonon modes are accessible, rather than the near-continuum of a bulk semiconductor. Their dynamics of excitation and radiative decay are analogous to that of individual atoms, and as such are frequently referred to as "artificial atoms", with the added benefits that their emission properties can be tuned and they can be embedded in a solid-state substrate. QDs can be created in a variety of ways, such as nanocrystals suspended in liquid solutions[41,42], or by generating a localised electrostatic trapping potential[43]. The QDs investigated in this thesis were created by epitaxial growth of semiconductor material onto a semiconductor matrix[44].

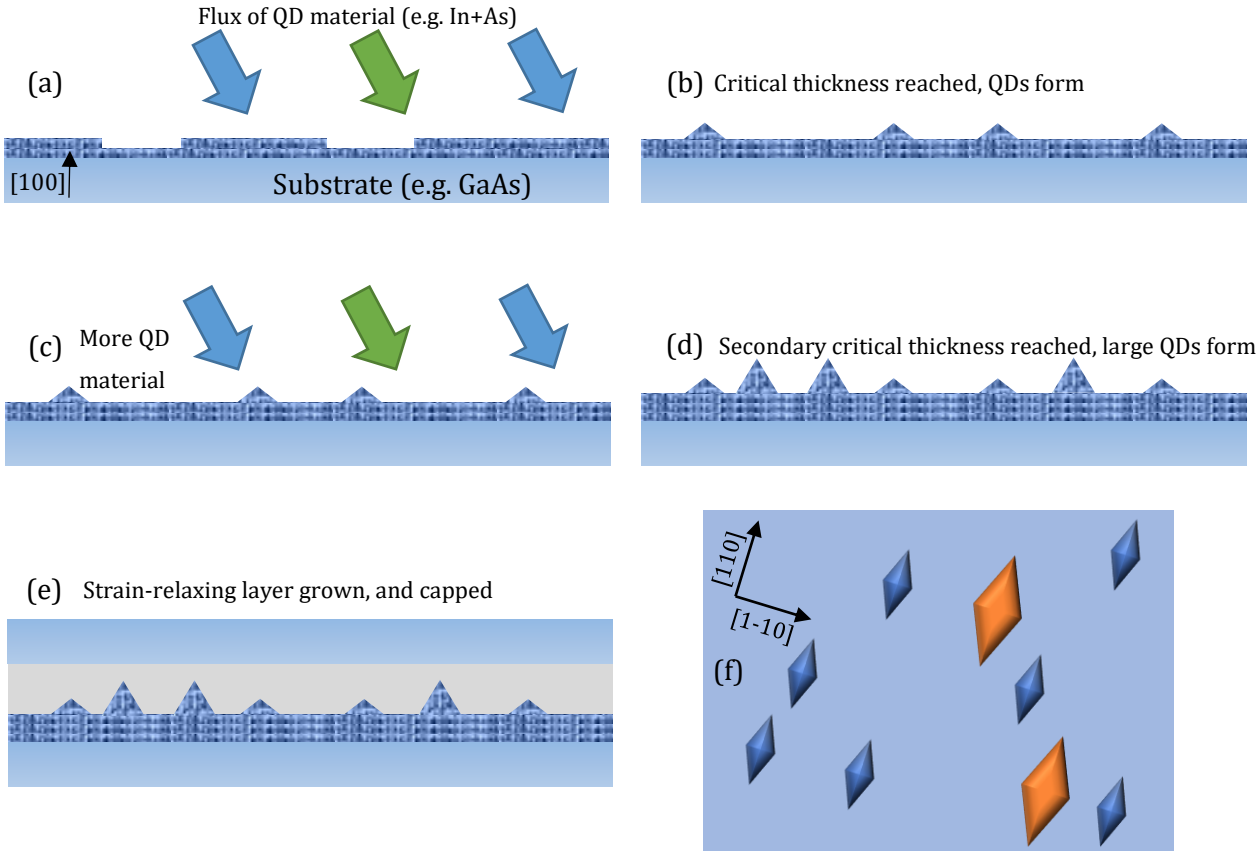

Figure 1.2: Illustration of the Stranski-Krastanow (S-K) growth mode [45] in forming a bi-modal distribution of quantum dots. The diagrams show (a) the deposition of QD material until a critical thickness is reached, (b) the formation of small QDs, (c) further deposition of QD material towards a second critical thickness, until (d) larger QDs have formed, which are then (e) covered with a strain-relaxing layer and capped with the substrate material. Shown in (f) is a representation of how our S-K QDs typically form, in a diamond shape typically elongating along the [110] axis of the crystal substrate.

Figure 1.2 illustrates the growth of III-V QDs in what is known as the Stranski-Krastanow growth mode[45]. The QD material, indium and arsenic in our case, is epitaxially grown onto a semiconductor substrate such as GaAs. Atomic terraces of InAs form, until a critical thickness is reached, upon which the strain that has been building up to the lattice mismatch between the QD material and the substrate causes small nanometre-scale islands to form. These are QDs that can be used in a variety of quantum optics experiments, typically at wavelengths below 1000 nm[29,39,46–49]. However, by continuing growth after this critical thickness is reached until a second critical thickness value is reached, larger QDs will form. Considering the quantum 'particle in a box' picture[50], it can be surmised that larger QDs will emit at longer wavelengths, hopefully into the optical fibre transmission windows (~1300 nm and ~1550 nm). To push the emission wavelength higher, a strain-relaxing layer is grown, and the QD layer is capped with the substrate material. Unfortunately, the strain which forms the dots will also cause them to preferentially elongate along the [110] crystal axis of the substrate, causing the degeneracy of important states to be lifted, as will be discussed in Chapter 3.

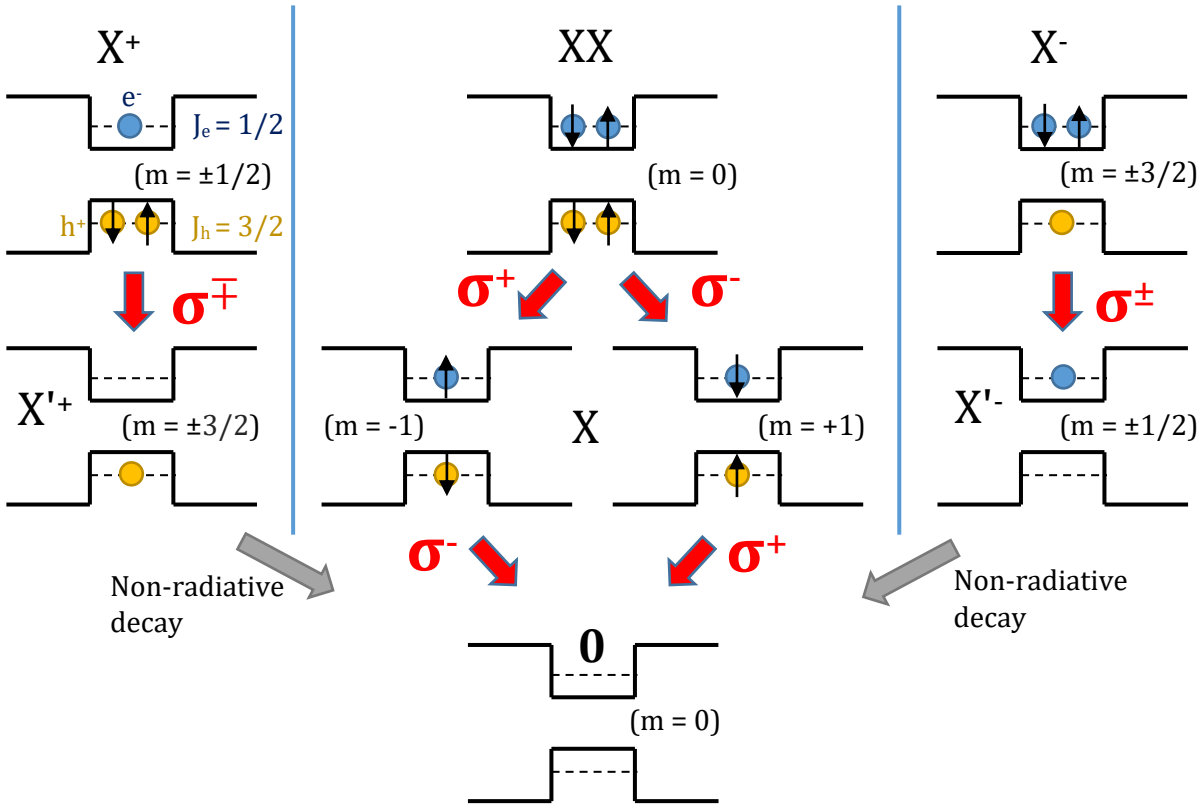

Figure 1.3: Configurations of electrons and holes in the lowest conduction and valence band of a III-V quantum dot, and the bright dipole transitions ($\Delta m = \pm 1$). Here we have electrons (blue circles) with angular momentum of $J_e = 1/2$, and heavy holes (orange circles) with angular momentum of $J_h = 3/2$. Our states of interest are the biexciton (XX) and the exciton (X), where the cascade from XX to the ground gives rise to a $(\sigma^{\pm}, \sigma^{\mp})$ pair of polarization-correlated photons.

The QDs studied in this thesis are indium arsenide (InAs) QDs grown on a gallium arsenide (GaAs) or indium phosphide (InP) substrate. InAs has a band gap energy of ~0.4 eV, GaAs has a band gap of ~1.5 eV, and InP has a band gap of ~1.4 eV between the bulk valence and conduction bands[51,52]. It was supposed that the smaller lattice mismatch between InAs and InP of 3 %, compared to the 7 % mismatch between the lattice constants of InAs and GaAs, would allow larger dots to form, causing the electronic states to be less strongly confined, resulting in emitted light red-shifted into the optical fibre telecom bands. Due to the small bandgap of InAs relative to GaAs or InP, and the strong spatial confinement of the InAs QDs, there are just a few discrete levels that electrons and holes can occupy in[53]. Additionally, due to the spin-orbit interaction in InAs QDs, light holes ($m = \pm 1/2$) are split off by several tens of meV, causing them to be poorly confined[54], so only heavy holes ($m = \pm 3/2$) need be considered. Pairs of electrons and heavy holes can be bound, and considered together as pseudoparticles called excitons. Shown in Figure 1.3 are some of the important excitonic configurations: the positively (X^+) and negatively (X^-) charged excitons, the neutral exciton (X), and the neutral biexciton (XX), and their associated bright transitions. The bright decay of a charge exciton leads to a single circularly-polarised photon being emitted, on average producing a beam of unpolarised photons. The decay of a neutral biexciton to the ground creates a pair of polarization-entangled photons. Typically, XX has a binding energy relative to the X state, such that the two photons emitted are spectrally resolvable. These are the photons that are going to make up the entanglement resource for our quantum relay.

1.4 Experimental techniques

1.4.1 Micro-luminescence

The core of the quantum dot experiments was the ability to collect micro-luminescence (μL). A microscope in a confocal configuration was constructed for this task, achieving spatial isolation of the light collection on the order of several square microns on the sample surface thanks to the strong mode selectivity of the standard single mode fibre being used. As such, with a sufficiently low density of QDs, on the order of 1 μm^{-2}, it would be possible to individually address single dots.

There are two broad schemes in which the excitonic levels can be excited. The first scheme, as utilised in Chapters 2, 3, and 4 of this thesis, is to optically excite electrons and holes within the QD or the surrounding semiconductor material, in a process known as photoluminescence (PL). The second, at the core of Chapter 5, involves electrically injecting the charge carriers to the semiconductor device, in a scheme known as electroluminescence (EL). The former benefits from not requiring any special doping or processing of the QD sample to achieve excitation, while the latter requires a higher level of engineering. However, the latter scheme is desirable in that more compact QD devices can be designed, which would be important for future commercialisation.

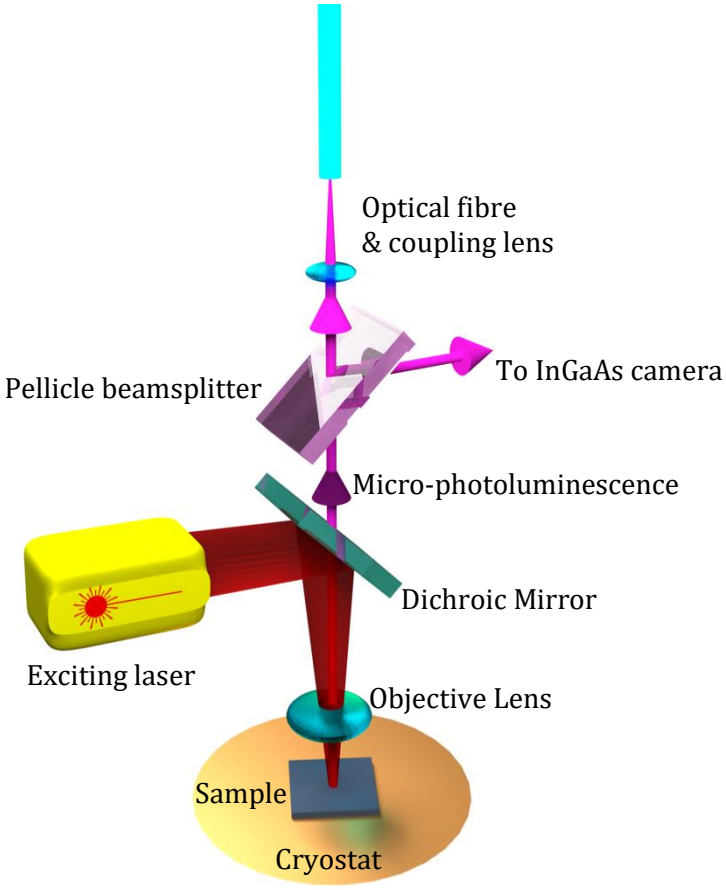

Figure 1.4: The confocal microscope used to achieve micro-photoluminescence from samples of quantum dots.

A representation of the confocal microscope setup used to achieve micro-photoluminescence (μPL) is demonstrated in Figure 1.4. A sample of QDs is held at cryogenic temperatures (4 to 20 K) in a liquid-helium-cooled cryostat. The exciting laser is injected into the collection path by way of a longpass dichroic mirror, and focused down to the surface of the semiconductor sample by an objective lens. The QDs' resulting μPL is then collimated by the same objective lens, transmitted through the dichroic mirror, and coupled into a standard optical fibre via a collimating lens. There is also a removable pellicle beam splitter, which diverts 45 % of the light to an InGaAs camera sensitive across the wavelengths of interest (~1 to 1.6 μm). The configuration for collecting micro-electroluminescence (μEL) differs only in that the laser and dichroic mirror are removed, and instead a voltage source is connected to a pair of electrical contacts attached to the cryogenically-cooled sample.

Resonance fluorescence, where the exciting laser is at the same wavelength as the QD emission of interest, is an effective method of excitation while retaining high coherence from the QD photons. Such a scheme was explored in[55] at ~1300 nm with a device nominally identical to that utilised in Chapter 2. The photons are close to being transform limited, which means that the photons will be indistinguishable from each other over longer timeframes than we would observe in more typical excitation schemes. However, there are practical problems in filtering the resonant laser light from the collected luminescence when considering an unpolarised beam, since spectral filtering becomes impossible, so it was decided not to pursue a resonant scheme for the telecom-wavelength quantum light sources described in this thesis.

Non-resonantly, there are two broad schemes of optical excitation. In above-band excitation, the exciting laser photons are at a higher energy than the bandgap of the surrounding semiconductor material. This excites electrons and holes in the surrounding matrix, which subsequently fall into the localised potential well of the QD. This kind of scheme is the simplest to implement, since the excitation laser beam does not need to be well-focused on the quantum dot. When exciting QDs above band, a 785 nm diode laser was used. Exciting between the above-band and resonant regimes, there is the below-band excitation scheme. Here, the exciting photons have energies below the bandgap of the surrounding matrix, but above the bandgap of the quantum dot. This excites electrons and holes within the QD itself, mitigating changes in the charge environment of the QD and potentially improving the coherence properties of the collected μPL.

1.4.2 Spectroscopy

Characterising the micro-luminescence collected from the QDs, it was necessary to perform spectrally-resolvable measurements. Through use of a spectrometer equipped with a liquid-nitrogen-cooled InGaAs sensor array, it was possible to measure spectra at wavelengths of 1 to 1.6 μm. Either the bare spectra from the collected QD μL was observed, giving an indication of the emission wavelengths and intensities, or intermediate optical components were introduced into the beam path, such as an interferometer (Section 2.3.3) or polarising optics (Section 3.3.1), to probe the coherence and excitonic properties of the QDs. Under reasonable excitation conditions, each QD tends to emit spectrally-distinct photons from the decay of at least four different transitions, and more if the QD is being excited strongly.

1.4.3 Time-correlated measurements

Time-resolved photon correlation measurements were performed by feeding measurement pulses from pairs of single-photon detectors to a system of time-correlating electronics. The detectors used were an array of four superconducting nanowire single-photon detectors (SNSPDs), chosen for their high efficiency and low timing jitter. The SNSPDs used in Chapter 2 had a timing jitter of 100 ps with 30 % efficiency, in Chapters 3 and 4 they had 70 ps of timing jitter with 60 % detection efficiency, and the system used in Chapter 5 had a detection efficiency of 45 % with a timing jitter of 65 ps. The time-correlating electronics recorded the arrival times of the photons with a precision of 1 ps. Thanks to the speed and efficiency of these detector setups, it was possible measure the temporal evolution of two- and three-photon correlations, such as the second-order autocorrelation function of Equation (1.2) as measured in the setup described in Figure 1.1. The central result of each experimental chapter in this thesis relied on this capability.

1.5 Thesis Outline

Chapters 2 to 4 of this thesis describe the work behind a fibre telecommunication O-band quantum relay, whereas the Chapter 5 describes the development of an electrical source of C-band telecom-wavelength entangled photon pairs.

In Chapter 2, measurement of two-photon interference is discussed. The result of this chapter involves photons from an InAs/GaAs telecom-wavelength sub-Poissonian QD light source being interfered with weak coherent photons from a laser, with observation of Hong-Ou-Mandel-type quantum interference[56]. The ability to produce high visibility two-photon interference between statistically dissimilar light sources is an important step in building a quantum relay.

Chapter 3 sees work on producing a source of quantum entangled photons at telecom wavelengths, based on a similar device to that discussed in Chapter 2 and nominally identical to the source in Ward *et al.*[27]. The chapter's main result is the generation of entangled photon-pairs in the telecom O-band ($\lambda \simeq 1300$ nm), with sufficient fidelity to operate a quantum relay. The chapter constitutes a thorough characterisation of the entanglement resource used later in Chapter 4.

In Chapter 4, the advances learnt from Chapters 2 and 3 are implemented in tandem as a quantum relay at telecom wavelengths. With an InAs/GaAs QD device emitting entangled photon-pairs in the O-band, the relay demonstrated sufficient performance to implement a quantum cryptographic channel, and the black box dynamics of the relay were fully characterised.

Alternate to the InAs/GaAs QDs of the previous chapters, Chapter 5 describes the development of an InAs/InP QD light source. By growing on an InP substrate instead of GaAs, it is found that QDs will emit natively in the optical fibre telecommunication C-band ($\lambda \simeq 1550$ nm). The end result of this chapter is the successful development of an entanglement-ready sub-Poissonian quantum light source emitting in the telecom C-band, which at the time of writing this thesis was developed by colleagues at the Toshiba Cambridge Research Labs into a C-band entangled-LED.

Two-Photon Interference 2

2.1 Introduction

At the centre of quantum mechanics lies the phenomenon of interference. Arising from the indistinguishability of quantum states, it leads to many effects which are of fundamental physical interest, as well as having application in a range of technologies. As an example, when two identical photons are impingent on separate input modes of a balanced beamsplitter, the two-photon interference will manifest as a bunching of the photons in the output modes, as first measured by Hong, Ou, and Mandel in 1987. That is, both photons will leave either by one port or the other. This effect is essential for linear-optics quantum computation implementations[33], and by performing a Bell-state measurement on these two photons, it is possible to herald the teleportation of quantum bits (qubits)[57]. The latter phenomenon would allow for the execution of a quantum relay[21], or even an all-photonic quantum repeater[58], both of which would be valuable resources in a large scale quantum network[4].

Also of interest is the ability to interfere photons with distinct statistics. That is to say, the spectral, spatial, and polarisation modes of these photons are kept as similar as possible, but the photons may come from different sources with dissimilar properties. For example, the difference between a quantum dot light source with its characteristically antibunched photons, and a laser with its Poissonian weak coherent states, as discussed in Section 1.2. There has been work looking both at two-photon interference between identical single-photon states[59–62], as well as interference between photons from dissimilar sources[36,63]. It has been shown that interference with dissimilar sources would allow measurement of both the spectral[30] and temporal[31] density matrices of otherwise unknown photonic states, as well as allowing the implementation of certain quantum amplifier schemes[64].

Today, the most mature technology based around photonic qubits is that of quantum key distribution (QKD)[65,66]. Of the numerous QKD schemes, the most widely applied make use of weak coherent laser pulses[67]. As it is not possible to enact a direct analogue of a signal amplifier in a quantum communication channel, due to the no-cloning theorem[15], the ability to realise a quantum relay, repeater, or amplifier scheme would be invaluable in reducing the effect of noise and increasing the range of a quantum channel. Considerable work has been carried out

investigating III-V semiconductor quantum dots (QDs) both as single-photon sources and sources of entangled photon pairs[37–40]. By interfering light from a QD with laser photons, such as carried out in Bennet et al.[63], it would be possible to teleport a laser-generated qubit. This was achieved by Stevenson et al.[29], later extended to a demonstration of a quantum relay over 1 km of optical fibre[46]. These three experiments, however, all operated at wavelengths below 1 μm, and as such would suffer from high photon losses over metropolitan distances. The experimental work in this chapter was performed in collaboration with Dr. Jan Huwer of TREL, and is summarised in Felle *et al.*[36], in which O-band (1260—1360 nm) telecom-wavelength photons from dissimilar sources (an InAs/GaAs QD and a laser) are interfered with high visibility. Together with the entanglement observed from a similar QD device emitting in the O-band[27], this successful two-photon interference result predicts the further success of a quantum relay implementation based around such a telecom-wavelength quantum dot source.

2.2 Modelling interference

2.2.1 Single-photon interference

To gain some insight into what is expected of this chapter's two-photon interference experiment, models for single and two-photon interference are explored, analysing quantum circuits corresponding to the paths of the photons in the spatio-temporal modefunction domain, as seen in Legero *et al.*[68]. Firstly, interference of single photons from a quantum dot is explored, revealing an important parameter for the later two-photon interference measurements, the single-photon coherence time. The QD single-photon source described in this chapter is influenced by its charge environment, affecting the coherence time of the emitted photons. Observing single-photon interference of QD emissions gives us a measure of the coherence time, where time-resolved fluorescence would be insufficient. The QD coherence time is a crucial parameter for two-photon interference and, as shown later in this thesis, quantum teleportation.

In this work, a Mach-Zehnder (MZ) interferometer was used to observe such single-photon interference. Figure 2.5 shows a circuit diagram of the interferometer, demonstrating the evolution of the incoming electric field operator E_1^+, representing the QD emission, through the interferometer, which has two $\cos^2\kappa_{a(b)} : \sin^2\kappa_{a(b)}$ non-polarising beam splitters. Assuming that the QD emission occupies a single spatial mode, such as by use of standard single-mode fibre, the interference can be treated in terms of normalised spatio-temporal mode functions[68] $\zeta(t)$. By introducing a delay $\Delta\tau$ in one arm of the interferometer, and where a_i is the photon annihilation operator, the field operators at each stage of the interferometer can be expressed as

$$\begin{aligned}
&\hat{E}_1^+(t) = \zeta_1(t)a_1, \qquad \hat{E}_2^+(t) = \cos\kappa_a\,\hat{E}_1^+(t), \qquad \hat{E}_3^+(t) = \sin\kappa_a\,\hat{E}_1^+(t)\\
&\hat{E}_4^+(t,\Delta\tau) = \cos\kappa_b\,\hat{E}_2^+(t) + \sin\kappa_b\,\hat{E}_3^+(t+\Delta\tau)\\
&\qquad = \cos\kappa_b\cos\kappa_a\,\hat{E}_1^+(t) + \sin\kappa_b\sin\kappa_a\,\hat{E}_1^+(t+\Delta\tau)\\
&\qquad = \left(\cos\kappa_b\cos\kappa_a\,\zeta_1(t) + \sin\kappa_b\sin\kappa_a\,\zeta_1(t+\Delta\tau)\right)a_1
\end{aligned} \tag{2.1}$$

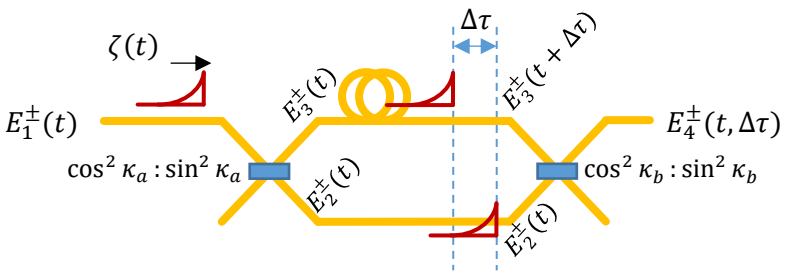

Figure 2.5: Circuit diagram of the Mach Zehnder interferometer. The beam splitters are nominally 50:50 to allow maximal interference contrast, but Equation (2.6) shows that imbalanced splitters can be tolerated.

The probability of a photon emerging from output 4 of the interferometer, at a time t after its creation, with a relative optical delay $\Delta\tau$ between the two arms, is given by

$$\begin{aligned} p(t,\Delta\tau) &= |\langle 1_1|\mathrm{E}_4^-(t,\Delta\tau)\mathrm{E}_4^+(t,\Delta\tau)|1_1\rangle|^2 \\ &= \cos^2\kappa_a\cos^2\kappa_b\,|\zeta_1(t)|^2 + \sin^2\kappa_a\sin^2\kappa_b\,|\zeta_1(t+\Delta\tau)|^2 \\ &\quad + \sin\kappa_b\sin\kappa_a\cos\kappa_b\cos\kappa_a\left(\zeta_1^*(t)\zeta_1(t+\Delta\tau) + \zeta_1^*(t+\Delta\tau)\zeta_1(t)\right) \end{aligned} \tag{2.2}$$

The QD photons can be considered as being created at time $t = 0$, exponentially decaying with a radiative lifetime τ_r, central frequency ω, and random phase fluctuations $\Phi(t)$. The temporal wavefunction $\zeta_1(t)$ of a QD photon can thus be expressed as

$$\zeta_1(t) = \frac{1}{\sqrt{\tau_r}}\exp\left(-\frac{t}{2\tau_r} - i\omega t - i\Phi(t)\right)\Theta(t) \tag{2.3}$$

where $\Theta(t)$ is the Heaviside step function. $\langle\exp(\mathrm{i}[\Phi(t) - \Phi(t+\Delta\tau)])\rangle = \exp(-|\Delta\tau|/T_2)$ describes the contribution to the coherence time of the QD from the pure dephasing time T_2. The coherence time τ_c is related to the radiative lifetime τ_r and pure dephasing time T_2 by

$$\frac{1}{\tau_c} = \frac{1}{2\tau_r} + \frac{1}{T_2} \tag{2.4}$$

Since the photons will be observed over a duration much longer than a single photon length, the expression for the observed probability is $p(t,\Delta\tau)$ integrated over t, giving

$$\begin{aligned} P(\Delta\tau) &= \int_{-\infty}^{\infty}\mathrm{d}t\; p(t,\Delta\tau) \\ &= \frac{1}{2}(1 + \cos 2\kappa_a\cos 2\kappa_b) + \frac{1}{2}\sin 2\kappa_b\sin 2\kappa_a\,\mathrm{e}^{-|\Delta\tau|/\tau_c}\cos(\omega\Delta\tau) \end{aligned} \tag{2.5}$$

Typically, $\cos(\omega\Delta\tau)$ evolves much faster than the exponential term (that is, $2\pi/\omega \ll \tau_c$). The interference visibility is therefore defined as

$$\begin{aligned} V(\Delta\tau) &= \frac{P_{max}(\Delta\tau) - P_{min}(\Delta\tau)}{P_{max}(\Delta\tau) + P_{min}(\Delta\tau)} \\ &= V_0\mathrm{e}^{-|\Delta\tau|/\tau_c} \end{aligned} \tag{2.6}$$

where $V_0 = \sin 2\kappa_b\sin 2\kappa_a/(1 + \cos 2\kappa_a\cos 2\kappa_b)$ is the visibility at $\Delta\tau = 0$. A value of τ_c can be extracted from measurements of $V(\Delta\tau)$ as long as $V_0 \neq 0$ (i.e. $\kappa_{a(b)} \neq n\pi/2\ \forall\, n \in \mathbb{Z}$). This relaxes the constraint of using precisely balanced 50:50 beamsplitters. We now have a practical means of characterising the coherence properties of quantum dot luminescence, which is crucial for the observation of two-photon interference.

2.2.2 Two-photon interference

Although the preceding single photon interference model was constructed using quantum operators, the same conclusions could have been reached using classical electrodynamics. The same is not true for two-photon interference (TPI), as demonstrated by Hong, Ou, and Mandel in 1987[56], where indistinguishable photons incident on separate inputs of a beamsplitter will leave bunched; this is an exclusively quantum phenomenon.

To introduce the mechanics of two-photon interference, consider a simple idealised case: two otherwise identical photons arriving simultaneously at separate input ports (labelled 1 and 2) of a 50:50 non-polarising beam splitter, as shown in Figure 2.6 (a). Because of the way the amplitudes of the reflections and transmissions add up, the resulting output is a bunched entangled state—a two-photon NOON-state[69]—which becomes evident if we expand the two-photon state in terms of the input and output modes:

$$|\Psi\rangle = |1_1 1_2\rangle = a_1^\dagger a_2^\dagger |0\rangle = \frac{1}{2}\left(a_3^\dagger - a_4^\dagger\right)\left(a_3^\dagger + a_4^\dagger\right)|0\rangle = \frac{1}{\sqrt{2}}\left(|2_3 0_4\rangle - |0_3 2_4\rangle\right) \tag{2.7}$$

That is, an input state of one photon in each of the input modes leads to a coherent superposition of bunched outputs, a pure entangled state. This state is similar to a classical mixed state of pairs of photons leaving the beam splitter from the same port, with 50 % probability, with the crucial exception that there is a well-defined phase between the two amplitudes.

Similarly, if there is an arbitrary $\cos^2\kappa : \sin^2\kappa$ beam splitter, we will end up with the state

$$|\Psi\rangle = \frac{1}{\sqrt{2}}\sin 2\kappa\,\left(|2_3 0_4\rangle - |0_3 2_4\rangle\right) + \cos 2\kappa\,|1_3 1_4\rangle \tag{2.8}$$

Evaluating the fidelity of the state in Equation (2.8) to that in Equation (2.7), the latter of which has the form of the Φ^- Bell state, results in $|\langle\Phi^-|\Psi\rangle|^2 = \sin^2 2\kappa$. That is, the state is maximally entangled when there is a 50:50 beam splitter, and is completely unentangled when $\kappa = 0$ (100% transmission) or $\pi/2$ (100% reflection).

However, a realistic description of the interference would consider its temporal extent. From prior work[29,63], it is understood that the arriving single photons can be considered as wavepackets in the space-time domain[68]. The input modes $a_1^\dagger$ and $a_2^\dagger$ are not restricted to any spatio-temporal mode, so the modefunctions and field operators are taken as:

$$\zeta(t) = \varepsilon(t)\exp\left(-\mathrm{i}\phi(t)\right)$$
$$\hat{E}^+(t) = \sum_k \zeta_k(t)\,a_k\,, \text{and}\;\; \hat{E}^-(t) = \sum_k \zeta_k^*(t)\,a_k^\dagger \tag{2.9}$$

where $\varepsilon(t)$ and $\phi(t)$ can be taken as the real valued electric field amplitude and phase, without loss of generality, and $\varepsilon(t)$ is normalised such that $\int_{-\infty}^{\infty} \mathrm{d}t\;\varepsilon(t)^2 = 1$. If there is a photon in mode i, there is a probability of it being present at time t given by $P_i(t) = \langle 1_i|\hat{E}^-(t)\hat{E}^+(t)|1_i\rangle = \zeta_i^*(t)\zeta_i(t) = \varepsilon_i(t)^2$. If the Hilbert space of the input modes is limited to single modes, the field

operators at input modes 1 and 2 can be written as $\hat{E}^+_{1,2}(t) = \zeta_{1,2}(t)a_{1,2}$. The $\cos^2\kappa : \sin^2\kappa$ beam splitter transforms the input modes to the output by

$$\begin{pmatrix} \hat{E}^+_1(t) \\ \hat{E}^+_2(t) \end{pmatrix} = \begin{pmatrix} \cos\kappa & -\sin\kappa \\ \sin\kappa & \cos\kappa \end{pmatrix} \begin{pmatrix} \hat{E}^+_3(t) \\ \hat{E}^+_4(t) \end{pmatrix} \tag{2.10}$$

The bunching from port 3 is measured with a Hanbury Brown and Twiss (HBT) setup[34], with detectors at outputs 5 and 6 ($\hat{E}^+_5(t) = \hat{E}^+_6(t) = \hat{E}^+_3(t)/\sqrt{2}$). Now, the joint probability of measuring one of the photons at detector 5 at time t and another at detector 6 at time $t+\tau$ is:

$$\begin{aligned} p(t,\tau) &= \langle \Psi | \hat{E}^-_5(t)\hat{E}^-_6(t+\tau)\hat{E}^+_6(t+\tau)\hat{E}^+_5(t) | \Psi \rangle \\ &= \frac{1}{4}\langle 0 | a_1 a_2 \left(\cos\kappa\, \hat{E}^-_1(t) + \sin\kappa\, \hat{E}^-_2(t)\right)\left(\cos\kappa\, \hat{E}^-_1(t+\tau) + \sin\kappa\, \hat{E}^-_2(t+\tau)\right) \\ &\qquad \left(\cos\kappa\, \hat{E}^+_1(t+\tau) + \sin\kappa\, \hat{E}^+_2(t+\tau)\right)\left(\cos\kappa\, \hat{E}^+_1(t) + \sin\kappa\, \hat{E}^+_2(t)\right) a^\dagger_2 a^\dagger_1 | 0 \rangle \\ &= \frac{\sin^2 2\kappa}{16} |\zeta_1(t)\zeta_2(t+\tau) + \zeta_1(t+\tau)\zeta_2(t)|^2 \end{aligned} \tag{2.11}$$

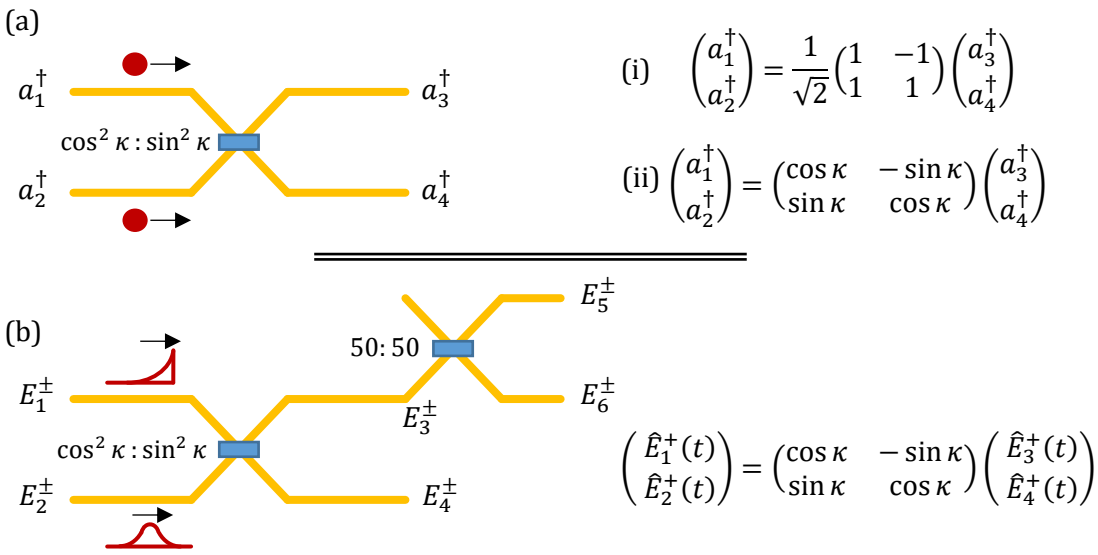

Figure 2.6: Diagrams demonstrating the phenomenon of Hong Ou Mandel two-photon interference[56], for pairs of photons impingent on a $\cos^2\kappa : \sin^2\kappa$ non-polarising beam splitter. Diagram (a) shows a simplistic view of the interference; two ideal Fock states in distinct input ports of a beam splitter arriving at the same moment in time. The outgoing state is in general entangled across the two output ports, with fidelity $\sin^2\kappa$, maximal for a 50:50 splitter, minimal for a fully reflecting or transmitting splitter. In the 50:50 case, the transmitted light is completely bunched: measurement of a photon in one of the output ports guarantees there is another photon present in this arm. Diagram (b) shows a more advanced model, considering the spatio-temporal extent of the incoming light, but still assumes we have exactly one photon in each input port. This second circuit closely resembles the actual experimental setup.

A similar expression for $p(t,\tau)$ where the two input modes are completely distinguishable, perhaps with orthogonal polarisations, is $p_{dist}(t,\tau) = \frac{\sin^2 2\kappa}{16}(|\zeta_1(t)\zeta_2(t+\tau)|^2 + |\zeta_1(t+\tau)\zeta_2(t)|^2)$. To find the expected probability of measuring coincident counts in modes 5 and 6 as a function of the time τ between detection events, given that the interference will be observed over timescales much longer than the length of the photon wavepackets, Equation (2.11) is integrated over all *t*, to arrive at the expression $P_{56}(\tau) = \int_{-\infty}^{\infty} \mathrm{d}t\, p(t,\tau)$.

To bring these dynamics in line with the QD and laser light sources, a pair of spatio-temporal modefunctions are defined. ζ_1 describes the QD emission mode (as in Equation (2.3)), and ζ_2 describes Gaussian laser wavepackets of temporal width σ.

$$\zeta_1(t) = \frac{1}{\sqrt{\tau_r}} \exp\left(-\frac{t}{2\tau_r} - i\omega_1 t - i\Phi(t)\right)\Theta(t)$$
$$\zeta_2(t) = \frac{1}{\sqrt{\sigma\sqrt{\pi}}} \exp\left(-\frac{(t-t_0)^2}{2\sigma^2} - i\omega_2 t\right) \tag{2.12}$$

As such, the probability of observing coincident counts in modes 5 and 6, as a function of relative delay τ, in the limit of continuous wave laser operation ($\sigma \to \infty$), can be expressed as

$$P(\tau) = \lim_{\sigma\to\infty} P_{56}(\tau) = \frac{\sin^2 2\kappa}{8}\left(1 + \mathrm{e}^{-\frac{|\tau|}{\tau_c}} \cos(\tau\Delta\omega)\right) \tag{2.13}$$

where $\tau_c = [1/2\tau_r + 1/T_2]^{-1}$ is the coherence time of the QD light, as in Equation (2.4), and $\Delta\omega = \omega_1 - \omega_2$ is the detuning between the QD photons and the laser light. Similarly, the probability of observing coincident counts for distinguishable input photons is evaluated as $P_{dist}(\tau) = \lim_{\sigma\to\infty} \int_{-\infty}^{\infty} \mathrm{d}t\, p_{dist}(t,\tau) = \sin^2(2\kappa)/8$. The TPI visibility at delay τ is expressed as

$$V_{TPI}(\tau) = \frac{P(\tau) - P_{dist}(\tau)}{P_{dist}(\tau)} = \mathrm{e}^{-\frac{|\tau|}{\tau_c}} \cos(\tau\Delta\omega) \tag{2.14}$$

In this more complete but still simplified model, it is clear that the TPI visibility depends crucially on the coherence time τ_c of the quantum dot emission, and the detuning $\Delta\omega$ between the laser and quantum dot light. Note, however, that the expression for $V_{TPI}(\tau)$ is independent of κ, as long as $\kappa \neq n\pi/2 \;\forall\, n \in \mathbb{Z}$. Practically, this allows the beamsplitter ratio to be chosen such that higher quality statistics will be collected faster. Typically, the intensity of the QD emission is a limiting factor, since the laser can be arbitrarily bright or dim in comparison with little difficulty. Choosing a beamsplitter weighted such that most of the QD photons got to the HBT setup will allow the experiment to be performed more quickly.

This example predicts 100 % visibility at $\tau = 0$, independent of the detuning and coherence properties. This is akin to observing the interference in an arbitrarily small time interval, where the uncertainty in the photons' energies will tend to infinity. This will not remain

the case, there are several experimental limitations in achieving 100 % visibility, as we will find out.

So far it has been assumed that the photons have statistics of ideal Fock states, whereas in fact the laser is a coherent state of the form $|\alpha\rangle = \exp(-|\alpha|^2/2)\sum_{n=0}^{\infty}\left(\alpha a^{\dagger}\right)^n/\sqrt{n!}\,|0\rangle$, and the QD state has the statistics $\left|\langle 0|\psi_{QD}\rangle\right|^2 = 1-\eta$ and $\left|\langle 1|\psi_{QD}\rangle\right|^2 = \eta$. The fluxes of photons from the QD and laser are proportional to η and $|\alpha|^2$ respectively. The statistics of the sources are suitably characterised by their second-order autocorrelation functions $g_L^{(2)}(\tau) = 1$ and $g_{QD}^{(2)}(\tau)$. The contribution of background light and dark counts can also be considered as a signal of intensity proportional to β with a $g^{(2)}$ of 1. Additionally, the relative polarisation angle χ between the laser and QD light is taken into account, as is the response function $R_f(\tau)$ of the detectors. Taking all of these factors into consideration, the second order cross-correlation functions that will be measured, and the corresponding TPI visibility, are of the form

$$g_{TPI}^{(2)}(\tau,\Delta\omega,\chi) = R_f(\tau)\otimes\left(1+\frac{\eta^2\left(g_{QD}^{(2)}(\tau)-1\right)+2\eta|\alpha|^2\mathrm{e}^{-\frac{|\tau|}{\tau_c}}\cos(\tau\Delta\omega)\cos^2\chi}{(\eta+|\alpha|^2+\beta)^2}\right)$$

$$V_{TPI}(\tau) = \frac{g_{\parallel}^{(2)}-g_{\perp}^{(2)}}{g_{\perp}^{(2)}} = \frac{2\eta|\alpha|^2\,R_f(\tau)\otimes\left(\mathrm{e}^{-\frac{|\tau|}{\tau_c}}\cos(\tau\Delta\omega)\right)}{(\eta+|\alpha|^2+\beta)^2-\eta^2+\eta^2\,R_f(\tau)\otimes g_{QD}^{(2)}(\tau)} \qquad (2.15)$$

where the beamsplitter ratios and detector efficiencies have been absorbed into the η, $|\alpha|^2$, and β intensity parameters. With no background ($\beta = 0$), ideal detectors ($R_f(\tau) = \delta(\tau)$), and a single photon source ($g_{QD}^{(2)}(0) = 0$), we see that the interference visibility can only asymptotically approach 100 %, as the ratio of QD to laser intensity increases. Later in the experimental preparation, the detector timing jitter was measured as 100 ps, and the background was estimated to be about 10 % of the QD intensity, so the peak interference visibility actually occurs at a QD/laser intensity ratio of approximately 2.

Figure 2.7 shows the expected peak TPI visibility as a function of coherence time and the relative dot/laser intensity, according to Equation (2.15). It is assumed that the bare QD $g_{QD}^{(2)}(\tau)$ is of the form $1-\exp(-\gamma|\tau|)$, where γ is the excitation rate of the QD, here taken as 1 GHz, which is a sensible estimate. The detector response function $R_f(\tau)$ is a Gaussian with full-width-half-maximum timing jitter $\Delta\tau_J$ of 100 ps in the left-hand plot, typical of a superconducting nanowire single photon detector (SNSPD) pair, and 300 ps for the right hand plot, typical for an avalanche photodiode (APD) pair. The background and detuning are here taken to be zero, but introducing a background decreases the peak TPI visibility, and shifts the peak interference towards a lower intensity ratio. The initial estimate of the conditions for the experiment is given by the red dot,

where τ_c = 150 ps and $\eta/|\alpha|^2 \simeq 2$, corresponding to a TPI visibility of roughly 60-65%. In the case of the APD pair, it would be difficult to observe interference visibility above the classical limit of 50 %. Considering that η is fixed by experimental conditions, a lower intensity ratio means a greater absolute number of photons, increasing the speed with which beneficial statistics are achieved.

To summarise, through the use of commercially available detectors and telecom wavelength laser light sources, and with a quantum dot emitting in the telecom O-band (~1300 nm[27,28]) exhibiting coherence times on the order of 150 ps, it is predicted to be possible to observe two-photon interference with visibilities as high as 65 %.

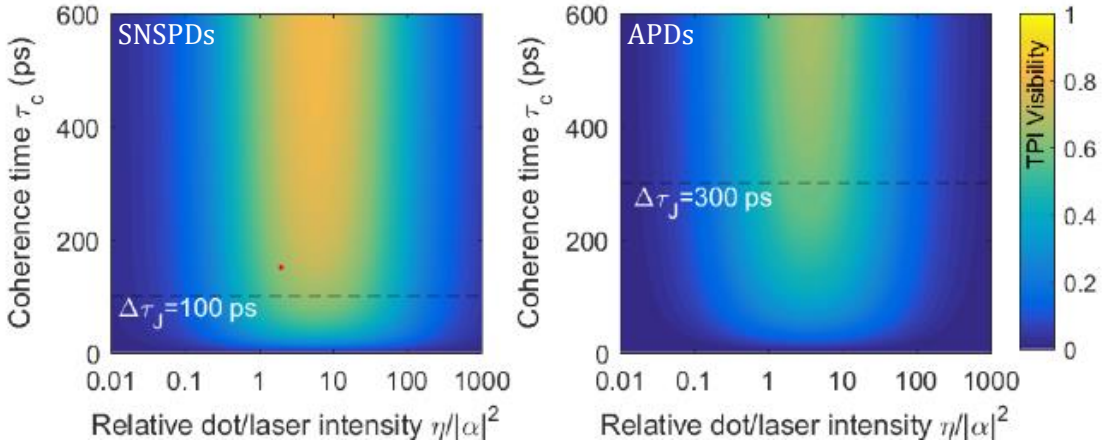

Figure 2.7: Simulated maximum two-photon interference visibility as a function of the dot/laser intensity ratio $\eta/|\alpha|^2$ and the QD coherence time, from Equation (2.15), for SNSPD ($\Delta\tau_J$ = 100 ps) and APD ($\Delta\tau_J$ = 300 ps) detector pairs. The red dot in the left-hand plot shows the region of operation for the TPI experiment later in this chapter.

2.3 Experimental preparation

The theoretical models developed in Section 2.2 describe two-photon interference between quantum dot single-photons and weak coherent states from a laser, predicting how such interference will manifest in a realistic laboratory environment. In this section, the experimental means and results of single-photon interference are discussed, as well as a description of the QD light source used in the TPI experiment, paying special attention to control over the coherence time of the QD emissions. The circuit described in Figure 2.6 (b) is subsequently realised, ready for observation of two-photon interference.

2.3.1 Quantum dot single photon source

The dot studied in this chapter is an InAs/GaAs self-assembled QD at the centre of the intrinsic region of a *p-i-n* diode, surrounded by a planar distributed Bragg reflector cavity made of AlGaAs/GaAs stacks, grown in the Stranski-Krastanov growth mode on a GaAs substrate. The DBR cavity of the wafer consists of 17 repeats of AlGaAs/GaAs underneath the QD layer, and one layer of the same material-pair above the dots. The result is a weak optical cavity that directs the QD emission around 1300 nm normal to the top surface of the chip. The device containing the QD operated at a temperature of 10 K, and was optically excited by continuous wave 785 nm laser light. The device has electrical contacts to apply a field to counteract the charge environment of the QD, and unless otherwise stated the device was operating at a bias voltage of +1 V. The design of the device can be seen in Figure 2.8. An aspheric lens (NA = 0.55) was used to collect the photoluminescence from the QD, coupled to a single mode fibre, which acted as a spatial filter isolating QD emission on the micron length scale. Preliminary measurements of the dot were performed with a grating spectrometer equipped with an InGaAs detector array.

By way of the quantum confined Stark effect[70,71], the wavelengths of the emissions from the QD are dependent on the applied electric field. As an applied field becomes stronger, the electron energy levels decrease, while the heavy hole energies increase, leading to longer wavelength photons being emitted. Figure 2.12 demonstrates how the wavelengths of the X and XX photons are tuned with applied bias voltage. The intensity of the fluorescence decreases with increasingly negative voltage, both because the emission is being tuned away from the optical cavity resonance of the device, and because the electron and hole wavefunctions become less overlapped in space, decreasing the probability of excitonic radiative recombination.

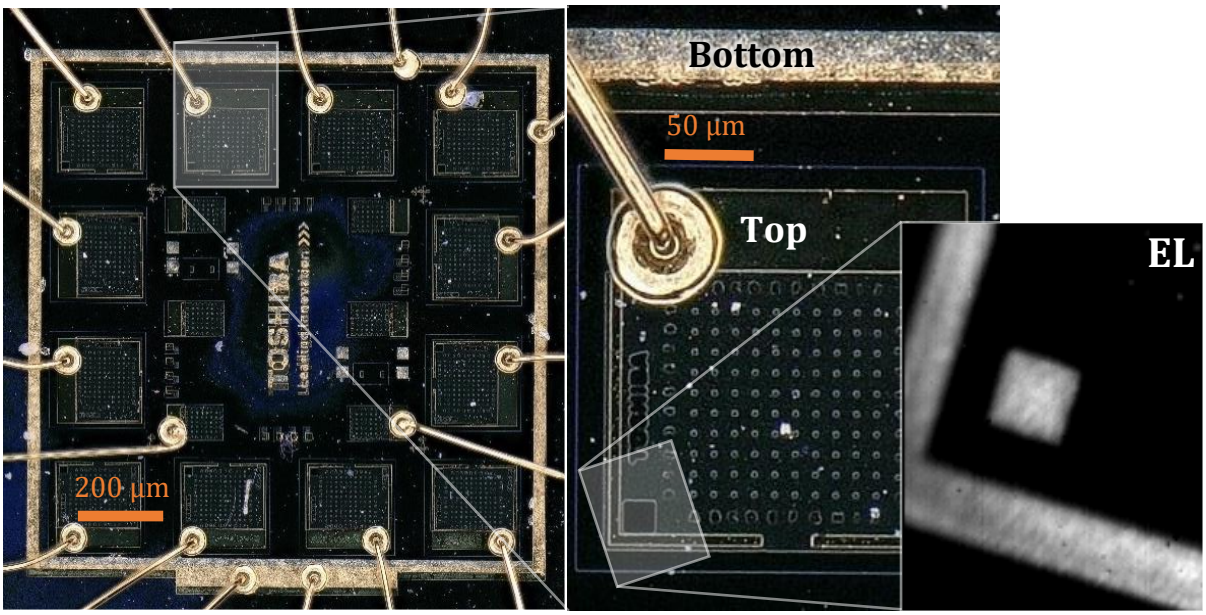

Figure 2.8: A dark field microscope image of devices on the chip, identical in design to those used in this chapter's experiments. The devices consist of top (smooth gold) and bottom (rough gold) electrical contacts, and a top layer of 3 µm-diameter aluminium apertures as an aid for position mapping. The inset black and white image is a telecom-wavelength photo of the actual experimental device under electrical excitation, where the white haze is emission from ~1300 nm QDs on what is a relatively high density portion of the wafer (around 10 dots μm^{-2}).

2.3.2 The Mach-Zehnder interferometer

An interferometer is a crucial piece of equipment in any quantum optics laboratory. A Mach-Zehnder interferometer, with the configuration discussed in Section 2.2.1, allowed for the en-masse characterisation of potential quantum dots for the two-photon interference experiment. Taking advantage of the ease of spatial-mode overlap found in standard single-mode optical fibres, as much of the interferometer was kept in-fibre as was practical.

The interferometer was constructed from single-mode polarisation-maintaining optical fibres, 50:50 non-polarising beamsplitters, a motorized freespace optical delay, and a piezo fibre-stretcher. As shown in Figure 2.9, both arms of the interferometer have the ability of introducing a phase delay. The freespace variable delay stage, consisting of two collimating lenses on a motorized stage, was used to introduce a large coarse delay $\Delta\tau_{coarse}$, in steps of several tens of picoseconds, where the minimum step size was ~2.5 fs, and the stage had a total travel range of 300 ps. The piezo-actuated fibre-stretcher introduced smaller delays to the optical path, in step sizes considerably smaller than $2\pi/\omega$.

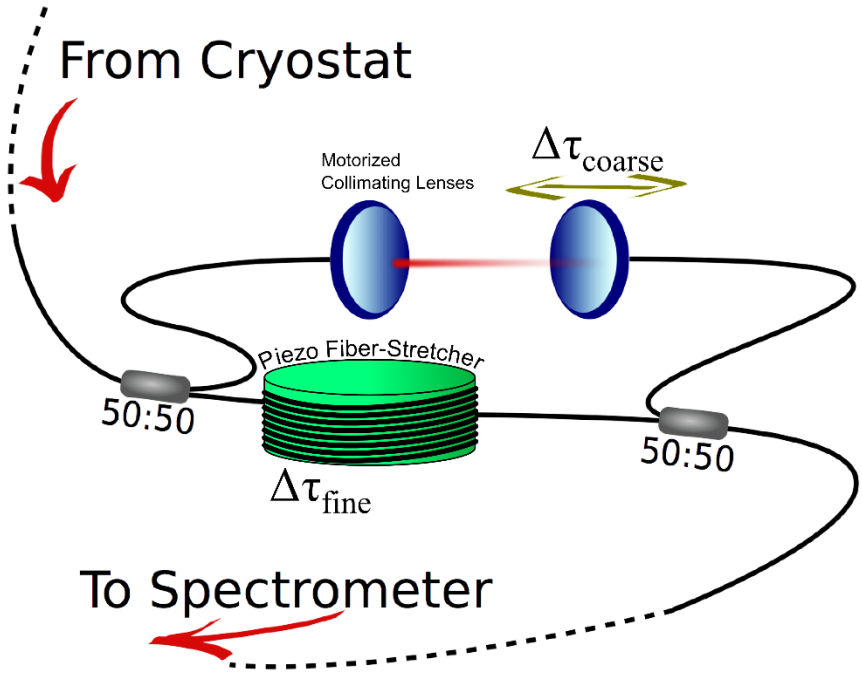

Figure 2.9: A representation of the Mach-Zehnder interferometer used to characterise the quantum dots. In one arm, a pair of collimating lenses mounted on a motorized stage make up a coarse variable delay, with a range of 300 ps, while in the other arm, a piezo fibre-stretcher is used to probe the interference fringes over much shorter time delays. All the fibre here is polarisation-maintaining, to the facilitate overlap of the polarisation modes, and before arriving at the spectrometer the resulting lights is filtered with a linear polariser, such that only light corresponding to one optical axis of the polarisation-maintaining fibre is measured.

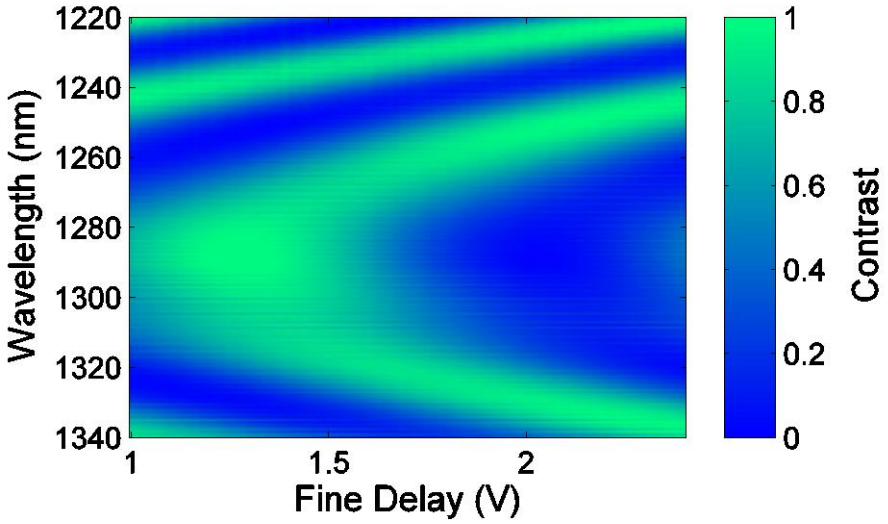

Figure 2.10: A plot showing an interference visibility contrast measurement of an LED light source at the 215.5 ps coarse delay position, which was taken to be the zero delay, for fine steps of 0.01 V in the piezo fibre stretcher.

Typically, the steps $\delta\tau_{fine}$ in the fine delay are much smaller than the steps of the coarse delay, such that $\Delta\tau_{coarse}$ corresponds to the variable $\Delta\tau$ in Equation (2.6). For a given wavelength and coarse delay, the visibility information $V(\Delta\tau)$ was extracted by fitting a sinusoidal curve of the form $V(\Delta\tau_{coarse}) \times \cos^2\left(\left[\omega\Delta\tau_{fine} + \phi(\Delta\tau_{coarse})\right]/2\right)$ to the experimental interference contrast $I\left(\Delta\tau_{coarse}, \Delta\tau_{fine}\right)/2\langle I\rangle_{\Delta\tau_{coarse}}$, where $I(\Delta\tau_{coarse}, \Delta\tau_{fine})$ is the intensity measured at the detector and $\langle I\rangle_{\Delta\tau_{coarse}}$ is the mean intensity at coarse delay $\Delta\tau_{coarse}$, which is nominally independent of the coarse delay positions. Later, Figure 2.13 (a) and (b) demonstrate this with an example data set from the experiment QD.

The output of the interferometer was sent to a spectrometer equipped with a liquid nitrogen-cooled InGaAs sensor array, sensitive across the fibre telecom bands (1000 to 1600 nm). By using the spectrometer, it was possible to probe the coherence of several emission lines from a QD simultaneously. Figure 2.10 shows a broadband interference measurement at a fixed coarse delay, with the piezo fibre stretcher modulated from 1 V to 2.4 V, in steps of 0.01 V, which was still much higher than the resolution limit of the voltage source. The end result was a piece of equipment that could measure single-photon interference for spectra in the telecom O-band across a range of 300 ps, providing visibility data that would allow the extraction of the coherence times for the various QD emission lines.

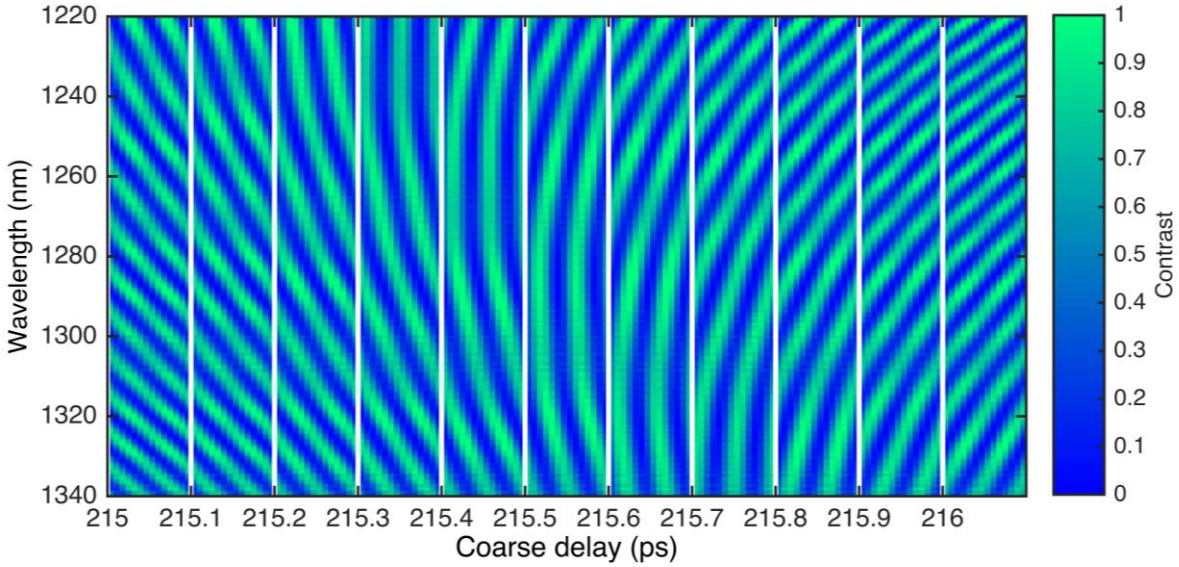

Figure 2.11: Interference contrast measurements of a 1300 nm broadband LED source, close to the zero delay of the interferometer. In total, 12 coarse delays are shown here, with the fine delay varied from +1 V to +2.4 V in steps of 0.1 V. The fine delays here are exaggerated for clarity; while it appears that one period of the interference fringe is about 50 fs, the actual period is roughly 4 fs.

The MZ interferometer was initially characterised with a broadband 1300 nm LED light source. This allowed the determination of the zero coarse delay of the configuration, corresponding to the lens position of maximal interference visibility, as well as correctly aligning the polarisation filtering, by finding the polarisation angle such that the interference visibility was independent of wavelength. Figure 2.11 shows how the interference fringes vary close to the zero delay of the interferometer; the fringes have almost identical amplitude, but they are the most symmetric at the 215.5 ps coarse delay, so this is taken as the zero value. The zero delay has a slight wavelength dependence, as can be seen by the variation of the interference fringe inflection point (where $\partial I/\partial\lambda = 0$) with $\Delta\tau_{coarse}$. However, this variation of roughly 4 fs nm^{-1} in the zero delay is tolerable, typically negligible in comparison to the fitting uncertainty, so for practical purposes can be ignored.

2.3.3 Single photon interferometry

A number of dots were investigated as candidates for the telecom wavelength two-photon interference experiment. As discussed in Section 2.2.1, the limiting factor to the interference visibility is often the coherence time of the QD emission. With the MZ interferometer discussed in Section 2.3.2, the coherence times of several dozen QDs were characterised. The spectral resolvability of the interferometer proved useful, since there are typically three or more spectral emission lines present, and they vary in wavelength with a dependence on the applied electric field, as exemplified in Figure 2.12.

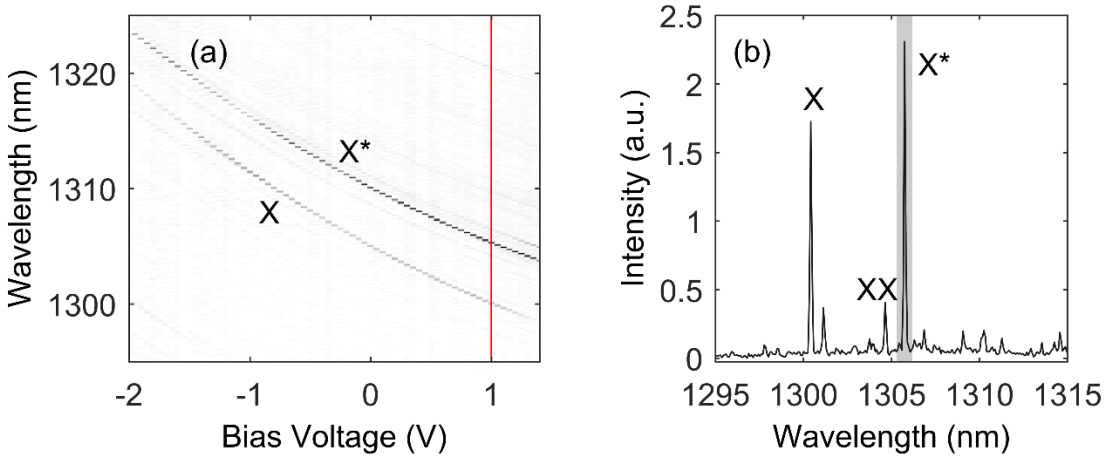

Figure 2.12: (a) µPL spectra of the experiment QD, under a varying vertically applied electric field, cooled to 10 K, under 785 nm CW laser excitation. The most prominent line is a charged exciton (X*) transition, which was used for the two-photon interference experiment, and the other prominent line is the neutral exciton (X). In (b), as plotted in Felle *et al.*[36], the µPL spectrum of the QD is shown under a bias voltage of +1 V, the same as the interference experiment conditions. The unpolarised charged exciton (X*) making up the single photon source is shaded for clarity.

Figure 2.13 demonstrates how the data for the Mach Zehnder interference measurements of the QDs is interpreted. The piezo fibre-stretcher adjusts the relative time delay in the two arms in fine steps, such that the steps $\delta\tau_{fine}$ are less than $2\pi/\omega$, while the freespace delay stage move in larger steps, such that $2\pi/\omega \ll \delta\tau_{coarse} < \tau_c$, and the total delay between is $\Delta\tau = \Delta\tau_{coarse} + \Delta\tau_{fine}$. Plot (a) in Figure 2.13 shows fine delay scans for two coarse delays. There is a distinctly sinusoidal change in the measured intensity at a single pixel of the array, and a sine curve is fitted to each coarse delay to find the corresponding visibility value. Plot (b) shows the change in visibility as a function of the coarse delay. As predicted, the visibility curve is close to exponential.

While the two-photon interference visibility in idealised conditions will always reach unity, with a temporal width determined by the coherence time, in reality the peak visibility will be lowered by uncorrelated coincidences, detector dark counts, and timing jitter. As such, the coherence time of the QD light in question must be at least as large as the detector timing resolution, which in this case is 101.9 ± 0.4 ps. Figure 2.13 (c) shows that the coherence time of the QD emission increases with bias voltage, for both the neutral biexciton (XX) state, and the charged exciton (X*) line of interest. The characterisations yielded a dot with a coherence time of 150 ± 9 ps, shown in Figure 2.13 (b). This was the dot used for the TPI experiment.

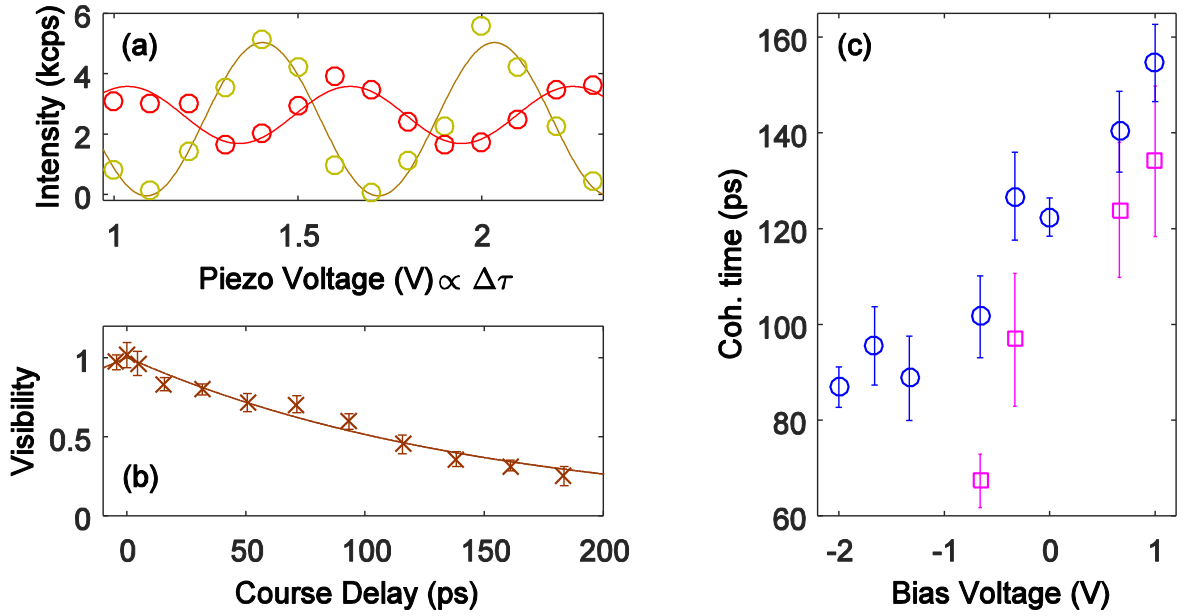

Figure 2.13: Single photon interference measurements. Plot (a) shows how the intensity of the QD light varies sinusoidally with the voltage on the piezo fibre stretcher in the MZ interferometer, for coarse delays of 0 (V = 101.7 ± 8.0 %) and 138.3 ps (V = 35.9 ± 4.7 %). (b) shows how the interference visibility decays with coarse delay, with an exponential fit giving us a lower limit on the coherence time of the light. Plot (c) reveals that the coherence time varies strongly on the applied bias voltage to the QD device, here showing X* (blue circle) and XX (pink square) measurements. The data from (b) and (c) is also shown in Felle *et al.*[36].

2.3.4 Two-photon interference circuit

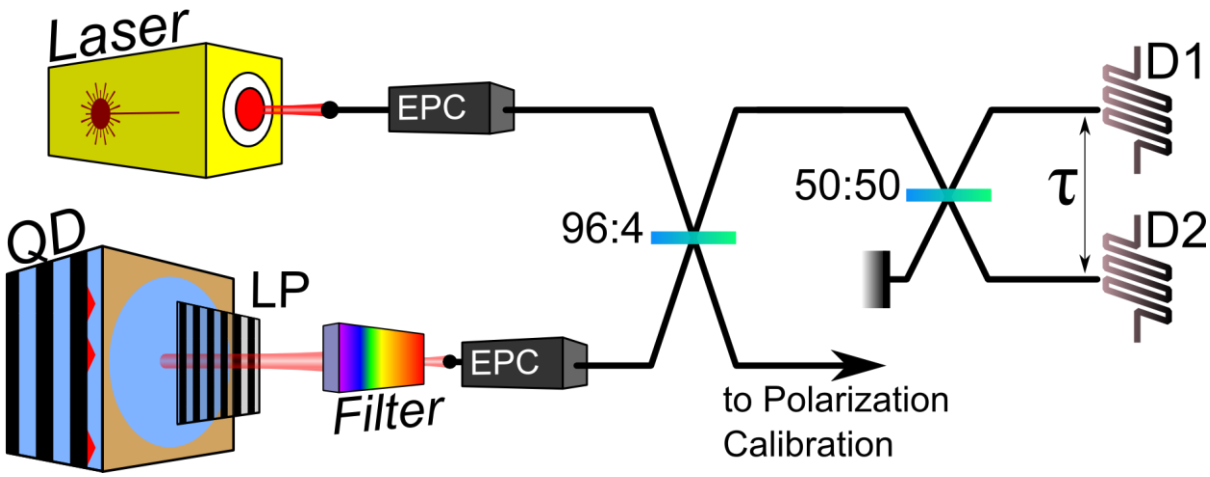

Figure 2.14: The experimental layout of the two-photon interference experiment, taken from Felle *et al.*[36]. The quantum dot device was excited with a 785 nm CW laser, suspended at a temperature of 10 K. Light from the QD was filtered through a linear polariser, and the charged exciton emission spectrally filtered through an O-band transmission diffraction grating, before being coupled into a single-mode fibre. A pair of electronic polarisation controllers (EPCs) were used to control the QD and laser polarisations such that the two beams were either cross- or co-polarised at the 96:4 beam splitter.

The experimental interference circuit consisted of the quantum dot single photon source, as described in Section 2.3.1, operating under the conditions described in Section 2.3.3, with the charged exciton (X*) line filtered to be spectrally isolated and linearly polarised. A commercial O-band CW diode laser was used to generate weak coherent states, with a specified spectral width of 2 neV, and with which it was possible to spectrally overlap with the QD X* line. The spectral overlap was achieved by first fitting a Gaussian curve to the lone QD X* spectrum and finding the central energy to within ±2 μeV, considerably more precise than the spectrometer resolution of 60 μeV. The QD light was then blocked, the laser turned on, and similar Gaussian fittings were performed while tuning the laser wavelength, until the centre of the laser spectrum was overlapped to within ±0.5 μeV of the QD value. With this method, the expected uncertainty in the laser/charged exciton detuning is 2 μeV, which is tolerable.

The two-photon interference circuit configuration used is shown Figure 2.14. The QD and laser photons were incident on separate inputs of a 96:4 beam splitter, which is where the two-photon interference can be said to have occurred. Correlations in one arm of the beam splitter, corresponding to 96 % transmission of the QD photons, were then measured with an HBT setup. The two detectors are a pair of SingleQuantum superconducting nanowire single photon detectors (SNSPDs), with timing jitter of 101.9 ± 4.0 ps. Events from the two detectors were sent

to time-correlating electronics, recording histograms of start-stop times between D1 and D2, equivalent to second order two-photon correlation function measurements ($g^{(2)}$) within a normalising factor. The raw data was recorded in bins of 1 ps size. The function $g^{(2)}(\tau)$ was measured for both co-polarised and cross-polarised QD/laser beams, from which the two-photon interference visibility can be extracted, per Equation (2.15).

During the experiment, the polarisation of the laser through the circuit was kept fixed, while the QD light was switched between being co- and cross-polarised relative to the laser, via electronic polarisation controllers (EPCs). Not shown in Figure 2.14 is the polarisation calibration apparatus, which consists of a PBS and two more detectors measuring the output intensities. The EPCs are not deterministic polarising elements, so a gradient-seeking search algorithm was implemented to find the settings that minimize the light sent to one of the detectors. The laser signal and the QD light signal were alternately minimised to the same detector to find the co-polarised settings, and then minimised to different detectors to find the cross-polarised settings. After this polarisation calibration, it was possible to run the two-photon interference experiment, where the interference was hoped to manifest as bunching of QD/laser photons in the co-polarised correlations, at time delays within the coherence time of the charged exciton.

2.4 Results

The two-photon interference experiment was carried out as described in Section 2.3.4. The ratio of the quantum dot ($\propto \eta$) to laser ($\propto |\alpha|^2$) intensity was set to 1.59 ± 0.10, where the quantum dot detected photon rate was 40 kHz. The measured second-order correlation functions are shown below in Figure 2.15, with the non-interfering cross-polarised (blue) and the interfering co-polarised (red) beams displayed together. Both correlations show an antibunching dip as they approach $\tau = 0$, characteristic of the sub-Poissonian nature of the quantum dot source. However, in the co-polarised case, we can see a bunching peak, due to the bosonic nature of the interfering particles. The data are plotted with model curves from Equations (2.15), with independently measured parameters: $g_{QD}^{(2)}(0)$ = 0.21 ± 0.04, $\Delta\tau_{jitter}$ = 101.9 ± 0.4 ps, and τ_c = 150 ± 9 ps. The deviations of the model curves near the zero delays can be explained by slight deviations in the alignment of the polarisation of the two beams relative to each other, and a possible small detuning between the QD and laser light on the order of 1 μeV.

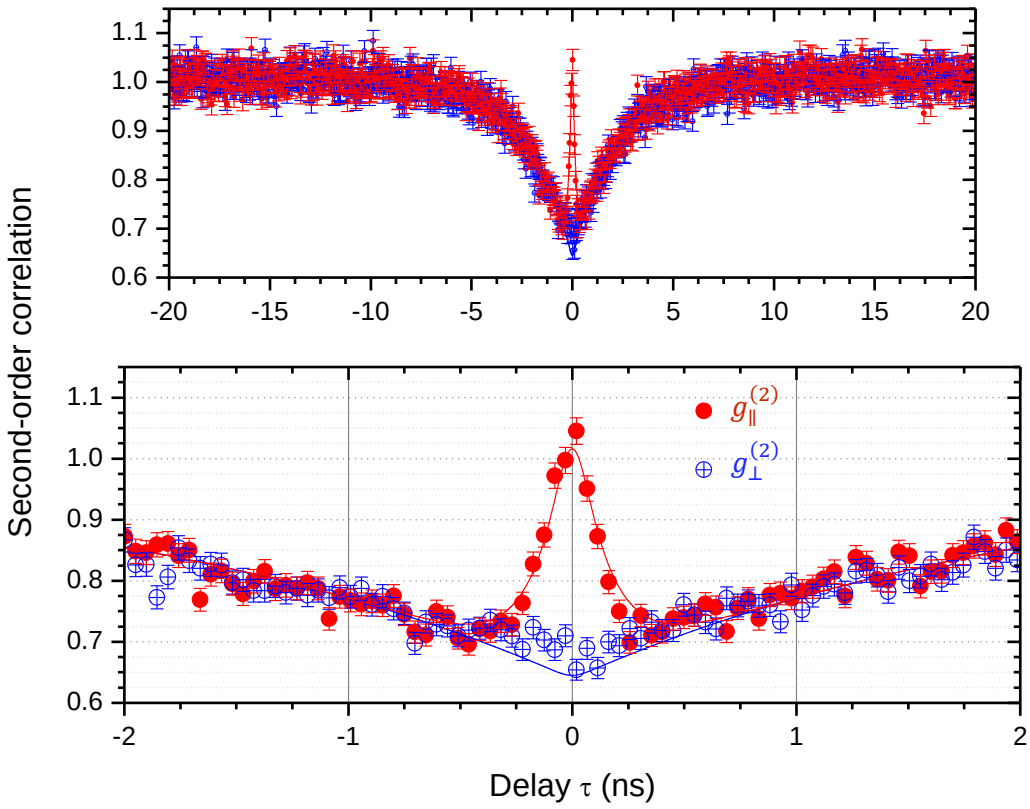

Figure 2.15: (Data plotted in Felle *et al.*[36]) The second order correlation functions ($g^{(2)}$) measured in the two-photon interference experiment, with 48 ps time bins. The non-interfering cross-polarised measurement (⊥, blue crossed circles) shows the antibunching dip characteristic of a QD light source, with a Poissonian contribution from the laser. The co-polarised beams (∥, red filled circles), however, exhibit an additional bunching peak close to a zero delay.

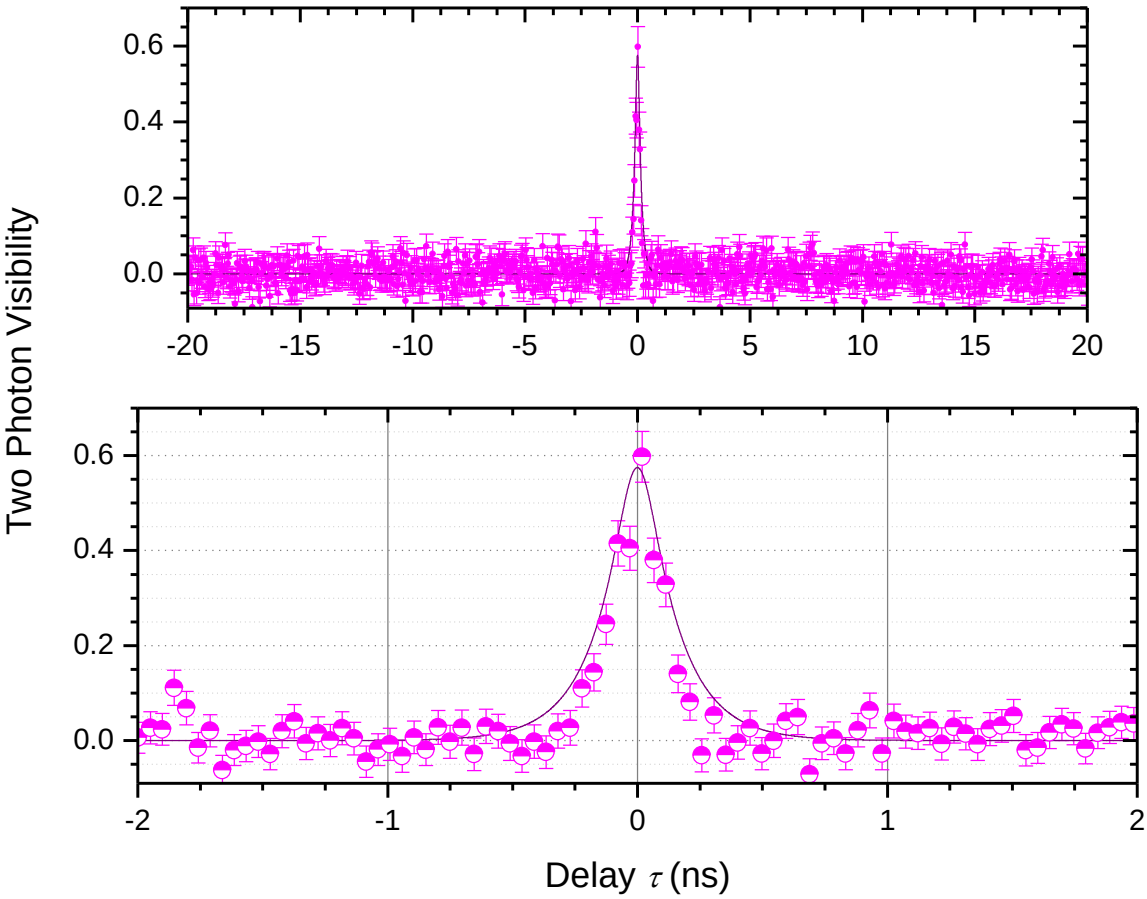

Figure 2.16: (Data plotted in Felle *et al.*[36]) The two-photon interference visibility of the QD and laser photons, extracted from the data in Figure 2.15 according to Equations (2.15), again with 48 ps time bins, as well as the corresponding model curve using independently measured parameters. The width of the interference peak is characterised by the coherence time of the QD light. The maximum visibility is limited by the detector timing jitter and the Poissonian laser and dark count contributions. The close adherence of the model to the experimental data suggests nearly perfect indistinguishability of the two distinct interfering modes. The peak visibility measured is 60 ± 6 %.

The two-photon interference visibility is shown in Figure 2.16, evaluated per Equation (2.15). As predicted, the visibility is high within the coherence time of the QD emission, while dropping to zero at time delays far away. The peak visibility is 60 ± 6 %, which corresponds to a value of 76.2 % if the effects of the background counts and detector timing jitter are removed. This means that an interference visibility corresponding to 79 ± 8 % of what was observable under ideal conditions has been measured, for the given QD/laser intensity ratio.

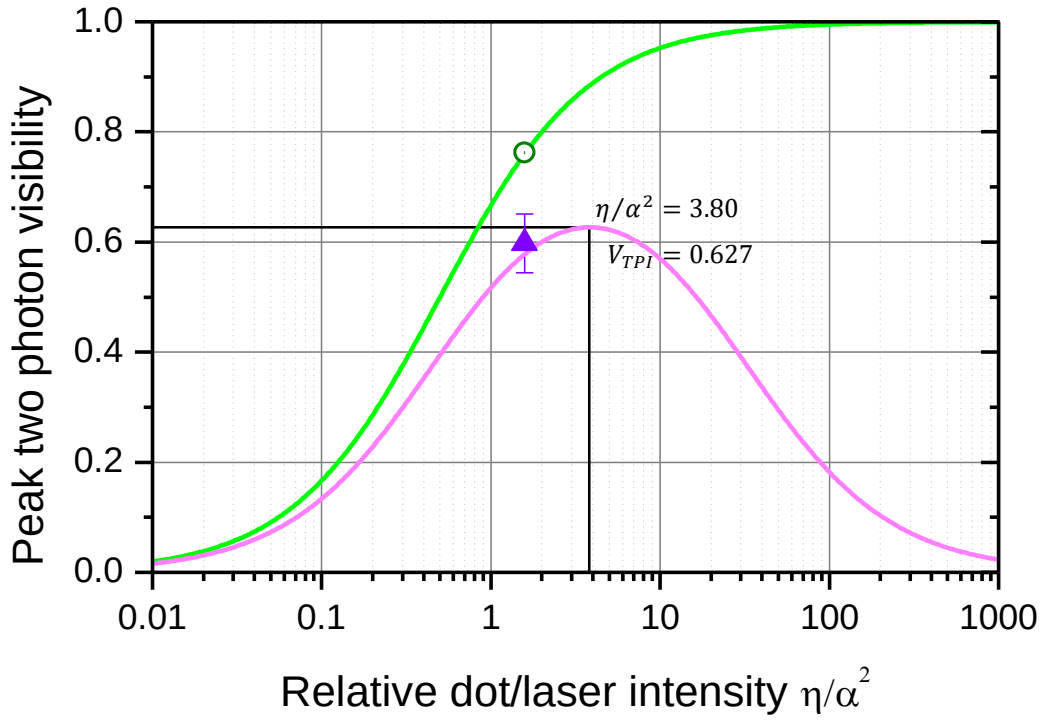

Figure 2.17: The predicted variation of the two-photon interference visibility with the dot/laser intensity ratio, from independently measured parameters.

The variations of the expected experimental and ideal interference visibilities are shown in Figure 2.17. In the limit of high laser power (low η/α^2), the measured correlations will be dominated by the laser's Poissonian contribution, and there will be zero interference visibility. However, for an arbitrarily low laser power (large η/α^2), the sub-Poissonian contribution of the QD will dominate, with the visibility asymptotically approaching 1. However, in reality, the finite timing jitter of the detectors and non-zero background counts will lead to a finite $g_{\perp}^{(2)}(0)$ for any intensity ratio, such that the visibility will again drop to zero. The TPI experiment operated at $\eta/\alpha^2 = 1.59 \pm 0.10$, which was about half of the optimal value of 3.8. However, there was a benefit of a roughly doubled rate of two-photon coincidences as a result, improving the statistics by a factor of $\sim\sqrt{2}$, without suffering greatly in reduced visibility.

This result represents the first measurement of two-photon interference between light from a quantum dot and a dissimilar source at fibre-telecom wavelengths.

2.5 Conclusions

The work in this chapter represents the first demonstration of quantum interference between light from a semiconductor quantum dot and weak coherent photons from a laser at telecom wavelengths. The raw data interference visibility of 60 % compares well with other raw visibilities achieved in other works, between identical single photon sources operating at lower wavelengths[36,40,63,68].

The results agree closely with the theoretical model explored in Section 2.2, strongly indicating that there is a high degree of indistinguishability between the independent light sources. Assuming an entanglement fidelity of 85 %, as has been observed at telecom wavelengths by M. B. Ward *et al.* in 2014[27], then the interference visibility would be sufficiently high to see quantum teleportation with fidelities in excess of 80 %, which is the threshold required for guaranteeing security in certain quantum key distribution applications[17].

Future work will entail exploring the two-photon interference of neutral biexciton photons, extending the coherence time as much as possible. A desired implementation would be through resonant excitation of the biexciton state. This would involve either resonant injection of electrons and holes into the QD, through an entangled-LED design[47], or through two-photon excitation. In the latter case, filtering of the exciting beam would become problematic, especially as an unpolarised biexciton beam would be required for a quantum relay, but the coherence time can be expected to increase by an order of magnitude in optimal conditions[55,72,73]. In the former case, such an ELED design is not compatible with the QDs described in this chapter, which already require an electrical field to be applied to control the QD charge environment.

Entanglement at Telecom Wavelengths 3

3.1 Introduction

Quantum entanglement is a central example of the differences between quantum mechanics and classical physics. Commonly known as the 'spooky action at a distance', where measurement of one part of an entangled ensemble will affect the others instantaneously, no matter how large a separation in space, entanglement finds use in a range of quantum technologies, as well as being of considerable interest in fundamental physics.

A more formal definition is that a multipartite state Ψ is said to be entangled if it cannot be expressed as a product of its individual constituent states ψ_i, i.e. $\Psi \neq \prod_i \psi_i$. Einstein, Podolsky, and Rosen[74] were troubled by this issue in quantum mechanics, believing that it must be possible to measure an element of nature without disturbing anything else. Bell[75] went on to consider and formalise this problem, recognising that sets of correlations could be measured to determine if nature can be completely described by locally real (including local hidden-variable) theories. One form of the Bell test which is frequently measured is the Clauser-Horne-Shimony-Holt (CHSH) inequality[76]. Sources of entanglement are crucial to testing Bell's theorem, in order to demonstrate the non-classical correlations required. Often, Bell tests require a certain number of assumptions before they can be said to be in violation of any possible local theory[77]. The detection loophole, where signal loss or detector inefficiencies can lead to unconvincing Bell inequality violation, has been addressed by Christensen *et al.*[78] and Giustina *et al.*[79]. The locality loophole has been investigated in experiments such as Weihs *et al.* [80] and Scheidl *et al.*[81]. Excitingly, there have been recent experiments simultaneously closing all of the main Bell test loopholes[82–84].

Aside from fundamental physics, entanglement is of considerable use in the field of quantum information[85], such as quantum key distribution[65,66,86], and implementations of linear optics quantum computing[33]. Sources of entanglement are also a crucial component of a quantum relay[21,87,88], as will be explored in Chapter 4. These quantum information technologies generally require high-fidelity sources. Typically in modern quantum technologies, entangled photon pairs are generated from spontaneous parametric down conversion sources[88–95]. However, the Poissonian statistics of such sources leads to unwanted multi-photon emission, degrading their quality as a source of entanglement.

Semiconductor quantum dots (QDs) have been proposed as sources of pairs of entangled photons through the radiative decay of the biexciton state[37]. They have been shown to have the statistics of single-photon emitters below 1 μm[38,48] and at telecommunication wavelengths[96–98]. The 3D spatial confinement in such a QD leads to distinct quantised energy levels that become saturated with pairs of excited electrons and holes due to the Pauli exclusion principle[99]. An excited state of two holes is known as a biexciton, and has two equally-probable radiative polarisation-correlated decay paths to the ground state of the QD, as displayed in Figure 3.1. Critically, the two decay paths have a well-defined relative phase, leading to the pair of emitted photons being entangled in polarisation. Early work investigating such an entanglement source was hampered by an energy splitting in the intermediate exciton state[100–102] arising from anisotropy in the shape of the QDs, known as the fine structure splitting (FSS). However, with the advent of higher bandwidth detectors and development of QDs with smaller FSS, it has been possible to observe entanglement first at wavelengths below 900 nm[39,47], and later in the fibre telecommunication O-band (~1300 nm[27]).

The experimental work in this chapter was performed in collaboration with Dr. Jan Huwer of TREL, using a QD device processed by Dr. Joanna Skiba-Szymanska, also of TREL.

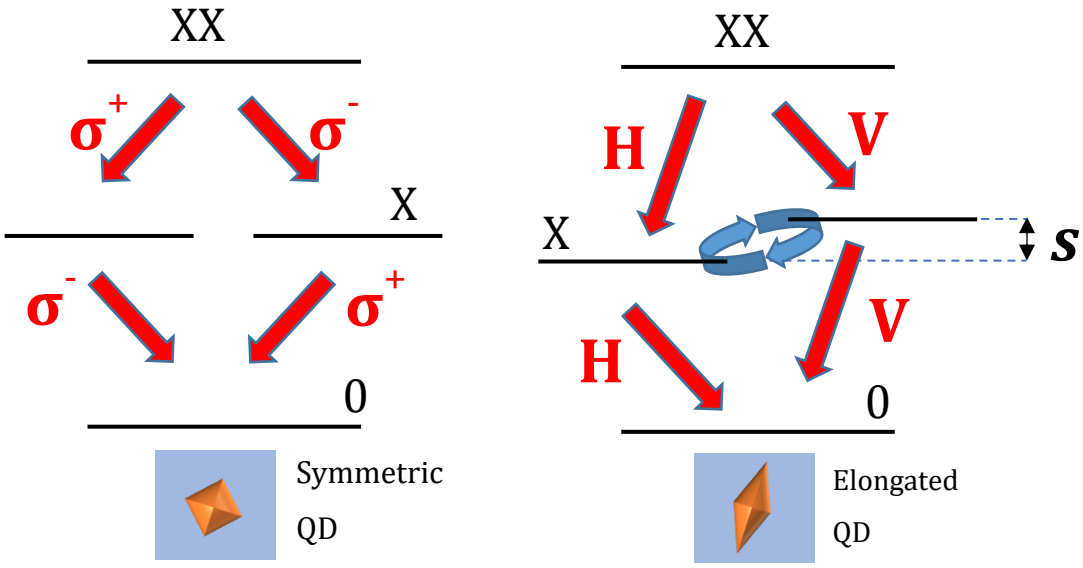

Figure 3.1: The quantum dot dynamics through which entanglement arises. In decaying from the doubly-excited neutral biexciton (XX) state, an emitted unpolarised photon leads to an intermediate superposition state for the neutral exciton (X), which then decays to the QD ground state with another unpolarised photon emitted. In a symmetric dot, the two X levels are degenerate. In an elongated dot, which is frequently the case, the degeneracy of the X levels is lifted for emitted polarisations corresponding to the crystal axes of the QD. The so-called fine structure splitting *s* leads the state to precess, accruing a phase in the resulting two-photon state, degrading the quality of the entanglement.

3.2 Background

3.2.1 Modelling Entanglement

As in the treatment at the start of Chapter 2, let us return to the spatio-temporal field operator regime of quantum optics, this time to predict how entanglement from the biexciton cascade of a quantum dot will manifest. Measurements of polarisation entanglement from the such a cascade have been performed routinely in Toshiba's Cambridge Research Lab, with examples in Salter *et al.*[47], Nilsson *et al.*[49], and at telecom wavelengths in Ward *et al.*[27] and the thesis of Matthew Dean[28].

Measuring polarisation entanglement entails performing polarisation correlation measurements. In our case, these measurements are performed as time-resolved coincidences between photons in the biexciton (XX) mode with polarisation $|A\rangle = \cos\alpha\,|H\rangle + \exp(\mathrm{i}\beta)\sin\alpha\,|V\rangle$ and photons in the exciton mode (X) with polarisation $|B\rangle = \cos x\,|H\rangle + \exp(\mathrm{i}y)\sin x\,|V\rangle$, as in Figure 3.2, where H and V are the eigenmodes of the emitted QD photons. By carefully choosing A and B, as will be described later in Section 3.2.3, parameters describing the quality of the entanglement can be extracted.

Consider a somewhat idealised model of the entanglement, where the input modes are assumed to consist of Fock states. There is some probability $p_{A,B}(t,\tau)$ of finding a photon in mode (X, B) at time $t+\tau$, and another photon in mode (XX, A) at time t. The electric field operators $\hat{E}^{+}_{iQ}$ (a single-mode contribution is assumed) for input mode i (XX or X) with polarisation Q are expressed in terms of their temporal modefunctions $\zeta_i(t)$ and annihilation operator a_{iQ} as

$$\hat{E}^{+}_{iQ}(t) = \zeta_{iQ}(t)\,a_{iQ} \tag{3.1}$$

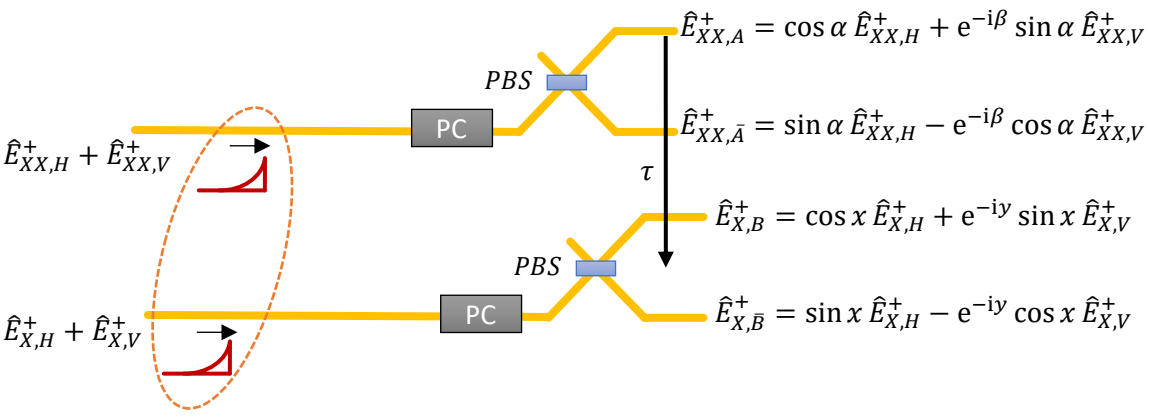

Figure 3.2: A circuit diagram displaying how entanglement from a dot is observed. Polarisation correlations are measured between biexciton photons with polarisation A against exciton photons with polarisation B. Typically, $A = B$.

It is now that the fine structure splitting (FSS) between the exciton eigenstates plays an important part. The biexciton state decays to the exciton level, upon which the energy difference in the exciton eigenstates causes the intermediate state to precess, accruing a phase relative to the biexciton level, until the exciton radiatively decays, with the phase difference preserved in the emitted photon. This phase difference is taken into account as an $s\tau/\hbar$ phase term in the two-photon state, where τ is the difference in time between the biexciton radiative decay and the exciton radiative decay. As such, the two input photons are taken to be in the entangled state

$$|\Psi_{in}\rangle = \frac{1}{\sqrt{2}}\left(|H_{XX}H_X\rangle + \mathrm{e}^{\mathrm{i}s\tau/\hbar}|V_{XX}V_X\rangle\right) = \frac{1}{\sqrt{2}}\left(a^{\dagger}_{XX,H}a^{\dagger}_{X,H} + \mathrm{e}^{\mathrm{i}s\tau/\hbar}a^{\dagger}_{XX,V}a^{\dagger}_{X,V}\right)|0\rangle \tag{3.2}$$

The probability $p_{A,B}(t,\tau)$ of measuring an *XX* photon at time t with polarisation *A* and an *X* photon at time $t+\tau$ with polarisation *B* is thus:

$$\begin{aligned} p_{A,B}(t,\tau) &= \langle\Psi_{in}|\hat{E}^{-}_{XX,A}(t)\hat{E}^{-}_{X,B}(t+\tau)\hat{E}^{+}_{X,B}(t+\tau)\hat{E}^{+}_{XX,A}(t)|\Psi_{in}\rangle \\ &= \frac{1}{2}|\zeta_X(t+\tau)|^2|\zeta_{XX}(t)|^2\left(\cos^2 x\cos^2\alpha + \sin^2 x\sin^2\alpha \right. \\ &\qquad \left. + \frac{1}{2}\sin 2x\sin 2\alpha\cos\left(\frac{s\tau}{\hbar} - \beta - y\right)\right) \end{aligned} \tag{3.3}$$

To simulate the dynamics of the entangled photons from a QD, we now incorporate the QD modefunctions, with the same form as the QD modefunction in Equation (2.3) from Section 2.2.1. For completeness, the random phase contributions $\Phi_i(t)$ are included, but these correspond to a global phase which cannot be observed, as evidenced by the modulus-square dependence of the modefunctions in the expression for $p_{A,B}$. That is to say, the entanglement does not depend on the pure dephasing (characterised by T_2 as in Equation (2.4)) of the quantum dot. The two modefunctions are

$$\begin{aligned} \zeta_{XX}(t) &= N_{XX}\exp\left(-\frac{\Gamma_{XX}t}{2}\right)\mathrm{e}^{-\mathrm{i}(\omega_{XX}t+\Phi_{XX}(t))}\,\Theta(t) \\ \zeta_X(t) &= N_X\exp\left(-\frac{\Gamma_X t}{2}\right)\mathrm{e}^{-\mathrm{i}(\omega_X t+\Phi_X(t))}\,\Theta(t) \end{aligned} \tag{3.4}$$

where ω_i and Γ_i are the central frequency and effective decay rate of mode i, respectively. $\Theta(t)$ is the Heaviside step function, and N_i is a normalising factor such that $\int_{-\infty}^{\infty}\mathrm{d}t\,|\zeta_i(t)|^2 = 1$.

The quantity of interest is the conditioned probability $P_{A,B}(\tau)$ of detecting a photon in mode (*X*, *B)*, given the detection of a photon in mode (*XX*, *A*), after a time delay τ. The individual probability $\int_{-\infty}^{\infty}\mathrm{d}t\,p_A(t)$ of observing the biexciton photon in mode (*XX*, *A*) at some point in time is $1/2$, as the stream of photons is unpolarised. So, by integrating Equation (3.3) over all time t, and dividing by this factor of $1/2$, we arrive at an expression for $P_{A,B}(\tau)$:

$$P_{A,B}(\tau) = \frac{\int_{-\infty}^{\infty} \mathrm{d}t\, p_{A,B}(t,\tau)}{\int_{-\infty}^{\infty} \mathrm{d}t\, p_A(t)}$$
$$= \frac{1}{2}\left(\Theta(\tau)\mathrm{e}^{-\Gamma_X \tau} + \Theta(-\tau)\mathrm{e}^{\Gamma_{XX}\tau}\right)$$
$$\times \left(1 + \cos 2x \cos 2\alpha + \sin 2x \sin 2\alpha \cos\left(\frac{s\tau}{\hbar} - \beta - y\right)\right) \quad (3.5)$$

However, the decay rate Γ_{XX} is typically much higher than Γ_X, suggesting that the decay from the biexciton level to the exciton level is much faster than the decay of the exciton state to the ground state, as one may expect. As such, we will approximate Equation (3.5) as

$$P_{A,B}(\tau) = \frac{1}{2}\Theta(\tau)\mathrm{e}^{-\Gamma_X \tau}\left(1 + \cos 2x \cos 2\alpha + \sin 2x \sin 2\alpha \cos\left(\frac{s\tau}{\hbar} - \beta - y\right)\right) \quad (3.6)$$

3.2.2 Measuring Entanglement

Experimentally, second-order correlations ($g^{(2)}$) of the exciton-biexciton polarisation entanglement will be measured. There is a chance that the exciton state will be reexcited to the biexciton level before having time to radiatively decay, contributing to an uncorrelated background. As a result, the polarisation cross-correlations will have the form

$$g^{(2)}_{A,B}(\tau) = g^{(2)}_{UC}(\tau) + \eta P_{A,B}(\tau) \quad (3.7)$$

where $g^{(2)}_{UC}$ is the uncorrelated contribution to $g^{(2)}_{A,B}$, and η is a parameter characterising how strongly the correlations occur relative to this background. The weaker the QD is being excited, the larger η will be. Usually in such a QD, $g^{(2)}_{UC}$ has a form close to $g^{(2)}_{UC}(\tau) = 1 - \exp(-\gamma|\tau|)$, where γ is an excitation rate dependant on how strongly the dot is being excited and the transition's radiative lifetime.

The polarisations of interest are typically those belonging to points on the poles (H and V) or the equator (superposition states) of the Poincaré sphere. For the HV correlations ($\alpha, x = 0$ or $\pi/2$), Equation (3.7) tells us that correlations will exhibit a smooth exponential decay after $\tau = 0$. For superposition states ($\alpha, x = \pi/4$), however, the correlations will be a decaying oscillation within the envelope of the HV correlations, with a period of h/s. Figure 3.3 displays the predicted cross-correlations between the QD eigenstates H and V, and two orthogonal superposition states ($D = (H + V)/\sqrt{2}$ and $A = (H - V)/\sqrt{2}$), as well as their corresponding correlation coefficients given by

$$C_{A,B}(\tau) = \frac{g^{(2)}_{A,B}(\tau) - g^{(2)}_{A,\bar{B}}(\tau)}{g^{(2)}_{A,B}(\tau) + g^{(2)}_{A,\bar{B}}(\tau)} \quad (3.8)$$

To make the theoretical prediction closer to what will be measured, the cross-correlations are also convoluted with the expected response of the detectors, which is taken to be Gaussian with timing jitter of 70 ps (an improvement on Chapter 2 thanks to the use of electrical bandpass

filters). This has the effect of reducing the superposition correlations below the envelope of the *HV* correlations.

In the case of measuring cross-correlations between rectilinear and superposition states, there is an equal chance of being in either state of the exciton measurement basis. This leads to identical $g^{(2)}$ curves, and correlation coefficients of zero. Were the fine structure splitting zero, this would be true for any pair of complementary bases (bases where $|\langle A|B\rangle|^2 = 1/2$). Instead, unless one of the bases is the rectilinear basis, there will always be oscillations, which are maximal in amplitude when looking at bases on the equator of the Poincaré sphere.

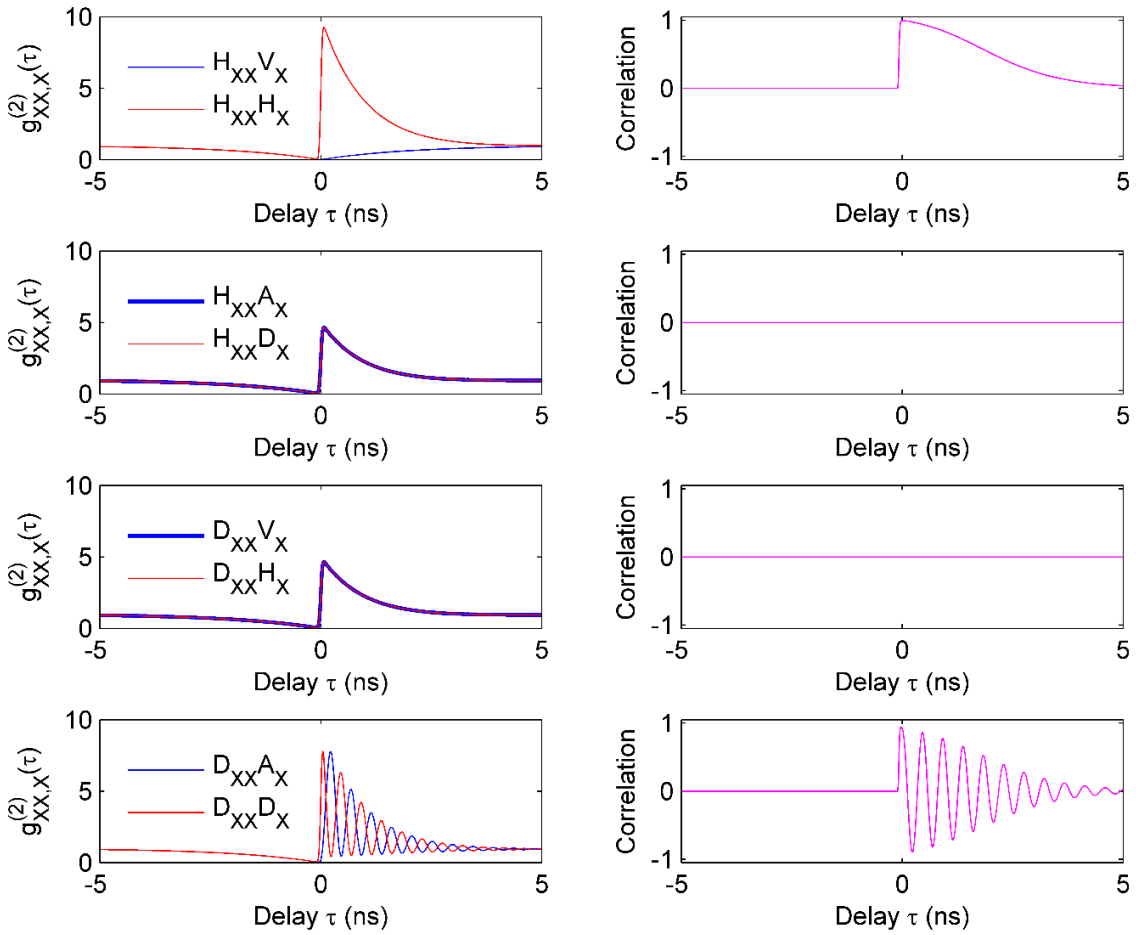

Figure 3.3: Cross-correlations and their respective correlation coefficients between the H, V, D, and A states. The uncorrelated contribution ($g^{(2)}_{HV}(\tau) = 1 - \exp(-\gamma|\tau|)$), here with γ = 0.5 GHz, and the lifetime of the exciton photon, here τ_X = 1 ns, causes the amplitude of the correlation coefficient to decay with time. The fine structure splitting, here s = 10 μeV, causes the correlations of superposition states to oscillate in time.

3.2.3 Quantifying entanglement

We will consider two quantities of interest in characterising the quality of our entanglement. First, is the fidelity to a maximally entangled state, such as one of the four Bell states[75]. For us, the $\Phi^{\pm}$ Bell states are particularly informative, since the QD two-photon emission is in the Φ^{+} state, under ideal circumstances. These two states have the form

$$\left|\Phi^{\pm}\right\rangle = \frac{1}{\sqrt{2}}(|HH\rangle \pm |VV\rangle) \tag{3.9}$$

A similar maximally entangled state with a phase term can be defined:

$$|\Phi(\phi)\rangle = \frac{1}{\sqrt{2}}(|HH\rangle + \exp(\mathrm{i}\phi)\,|VV\rangle) \tag{3.10}$$

The fidelity to such a state, as derived in Ward *et al.*[27], is

$$F(\phi) = \frac{1}{4}\left(1 + C_{HV} + (C_{DA} - C_{LR})\cos\phi + \left(C_{E_{LD}E_{RA}} - C_{E_{LA}E_{RD}}\right)\sin\phi\right) \tag{3.11}$$

where the C_{AB} are the same correlation coefficients from Equation (3.8). Setting ϕ to 0 or π is equivalent to measuring the fidelity of the two-photon QD emission to the Φ^{+} or Φ^{-} Bell state. Alternatively, $\phi = s\tau/\hbar$ describes a time-evolving maximally entangled state, where the accrued phase from the FSS is considered. By searching for a dot with as low fine structure splitting as possible, the entanglement fidelity will oscillate more slowly in time, which is desirable.

The second important quantity is the Bell parameter. This can be expressed with the form[27]

$$S_B(t) = \frac{1}{\sqrt{2}}\left[\left(C_{E_{LD}E_{RA}} - C_{E_{LA}E_{RD}}\right)\sin\left(\frac{s\tau}{\hbar}\right) + (C_{DA} - C_{LR})\cos\left(\frac{s\tau}{\hbar}\right) + 2C_{HV} + C_{DA} + C_{LR}\right] \tag{3.12}$$

Bell's theorem[75] governs differences between the predictions of classical systems and quantum mechanics, postulating that no local hidden variables theory can exist. According to the Clauser-Horne-Shimony-Holt (CHSH) inequality[76], under conditions of classical correlation the magnitude of the Bell parameter cannot exceed two:

$$|S_B| \leq 2 \tag{3.13}$$

Violation of the CHSH inequality is considered a proof of Bell's theorem. Quantum mechanics predicts a maximum possible value of $2\sqrt{2}$ for the Bell parameter S_B [103].

To summarise, we have explored a model describing the polarisation entanglement of photons arising from the cascade of a neutral biexciton to the ground state in a quantum dot, as would be measured in a laboratory. The crucial quantity in determining the quality of the entanglement is the magnitude of the correlation coefficient for complementary sets of measurement bases, which can be used to evaluate both the fidelity to a maximally entangled two-photon state and a time-evolving Bell parameter. The limiting factor in the strength of the correlations is expected to be the fine structure splitting of the exciton energy levels. In the next section, methods of ascertaining the FSS of a QD are discussed, and measures that can be taken to reduce the FSS in a particular dot are investigated.

3.3 Entanglement source

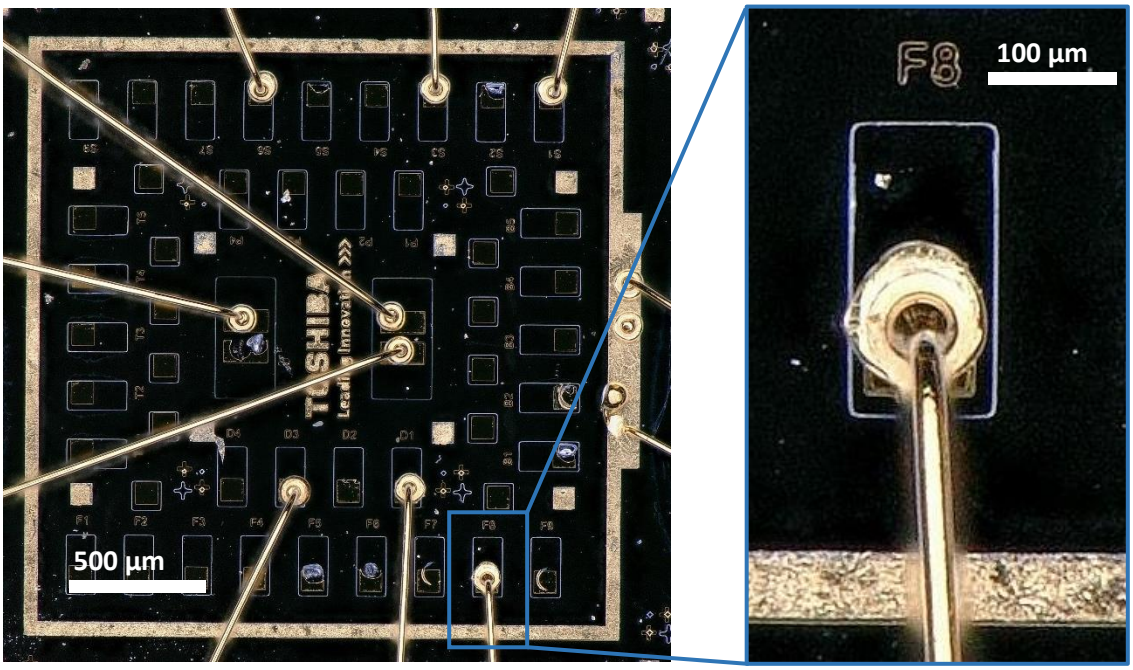

Figure 3.4: A microscope image of a device with an identical design to that used in Chapters 3 and 4, processed by Dr. Joanna Skiba-Szymanska. On this portion of the wafer, there is a dot density of approximately 0.02 QD µm^{-2}.

III-V Quantum dots have been demonstrated to emit pairs of natively telecom-wavelength entangled photons with nearly Fock state statistics[27,28]. The device here employs self-assembled InAs/GaAs quantum dots embedded in the intrinsic region of a *p-i-n* doped DBR cavity centred around 1300 nm, and is nominally identical to the devices used in Ward *et al.*[27] and Felle *et al.*[36], as well as the device used in Chapters 2 and 4. The dots emit in the telecom O-band thanks to a bimodal growth method that allows larger dots to form, as well as a 5 nm InGaAs strain relaxing layer on top of the dots. It was possible to explore a region of the wafer with an ultra-low QD density, thanks to the use of an InGaAs camera sensitive to telecom wavelengths (900-1600 nm), which was not the case for the work in Ward *et al.*[27] and earlier.

The following description of the source is true for the experimental work in both this chapter and Chapter 4, which relates to a single quantum dot. The QD was suspended in a helium flow cryostat at a temperature of approximately 10 K, with the exact temperature depending on environmental conditions, but stabilised to within ±50 mK. A top-down view of the device design is shown in Figure 3.4, where the QDs have been etched away from everywhere but on the 210 µm × 110 µm rectangular mesas, and metal contacts allow an electric field to be applied vertically across a mesa. Unless stated otherwise, a 0 V bias was applied across the device, and the sample was optically excited quasi-resonantly with a continuous-wave 1064 nm laser.

Photoluminescence was collected with a confocal microscope configuration, with an NA = 0.68 objective lens, and coupled into a single-mode fibre using an achromatic reflective coupler. Spectral isolation of the exciton and biexciton photons was achieved using a transmission diffraction grating.

By varying the voltage across the device, it is possible to tune the charge environment of the dot, altering the emission wavelength, coherence properties, the external charge tunnelling probability (leading to a change in the exciton and biexciton lifetimes), and the fine structure splitting. After successful observation of telecom-wavelength entanglement, it is hoped to implement a quantum relay with the same QD. As such, while a small FSS is the critical quantity in observing entanglement, it would also be desirable to extend the coherence time as much as possible so that two-photon interference could be observed. Unfortunately, the coherence and FSS tune in opposite directions to each other with the applied field (higher bias leading to longer coherence time but larger FSS), so it was necessary to find a point of compromise between a good coherence time, good fine structure splitting, and good flux of photons. Such a point occurred in the vicinity of a 0 V applied bias.

3.3.1 Measuring fine structure splitting

The jitter of the detectors, $\Delta\tau_J$, in this and the next chapter's work is 70 ps. To observe entanglement, suppose it is possible to resolve the oscillations in the correlations when the jitter corresponds to smaller than a $\pi/2$ change in the phase. This imposes the criterion that $s < h/4\Delta\tau_J \simeq 15$ μeV. So, a dot with $s < 15$ μeV is required.

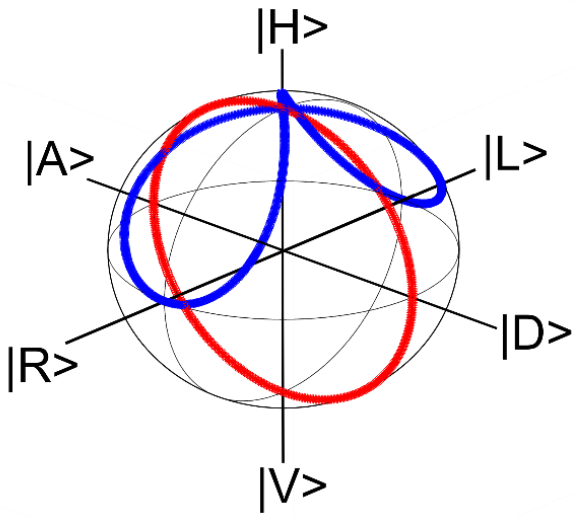

Figure 3.5: The one-qubit Poincaré sphere with traces of the measurement basis with changing waveplate angle, when making fine-structure splitting measurements. The red path shows the frequently used half-waveplate method, while the blue is our quarter-waveplate method. The first method is not robust against the introduction of birefringence to the beam.

Usefully, the FSS is a quantity that that can be measured spectrally, without directly observing exciton-biexciton polarisation correlations. The following treatment, developed by the author and detailed in the appendix of Skiba-Szymanska *et al.*[104], allows the measurement of the FSS of a quantum dot, after it has accrued an arbitrary but fixed birefringence, such as can occur from semi-polarising optics or transmission through a length of optical fibre. Firstly, suppose the quantum dot emits exciton or biexciton photons in the state ρ_1, where the H and V polarised photons, eigenstates of the Hamiltonian $\hat{H}$, have energies E_H and E_V.

$$\rho_1 = |H\rangle\langle H| + |V\rangle\langle V|$$
$$\hat{H}\rho_1 = E_H|H\rangle\langle H| + E_V|V\rangle\langle V| \tag{3.14}$$

For a QD that is symmetric along the [110] and [101] crystal axes, the two energies will be degenerate. This is not true in general, however. Elongation of the QD (grown on the [100] plane) in one of these directions occurs almost always for dots of this type, due to the growth techniques used to push the emission wavelength from ~850 nm towards ~1300 nm. This asymmetry causes the degeneracy of the eigenstates to be lifted, and they will exhibit a fine structure splitting $s = E_H - E_V$, with a mean energy $\varepsilon = (E_H + E_V)/2$.

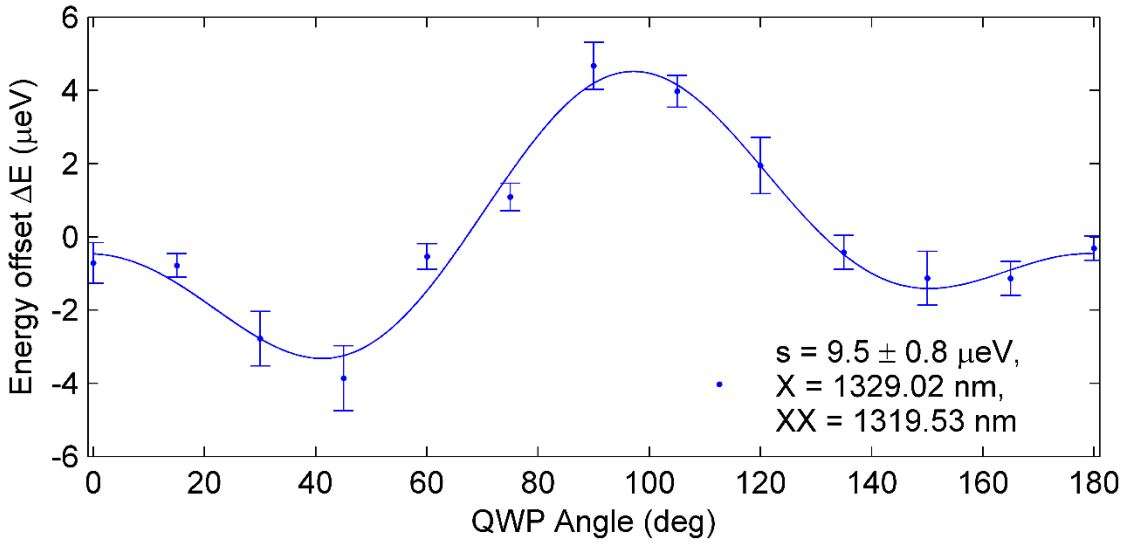

Figure 3.6: A fine structure splitting measurement of the QD that was eventually chosen as the entanglement source for our quantum relay. μPL spectra were measured for a number of quarter waveplate angles, and the central energies were found for the transition of interest via Gaussian fits to each line. The resulting shifts in energy with angle were then fit to the function given in Equation (3.18). In this case, the FSS was extracted as 9.5 ± 0.8 μeV, with exciton and biexciton wavelengths of 1329.02 nm and 1319.53 nm respectively.

After travelling through a sequence of generally polarising and birefringent optical components and fibres, the state will have accrued a degree of polarisation p, and undergone a rotation θ and phase shift ϕ in its polarisation. Assuming the effect is linear, the H and V eigenstates have been transformed to the bases B_1 and B_2, and the state ρ_1 is transformed to ρ_2, by

$$\begin{aligned}
|H\rangle \rightarrow |B_1\rangle &= \cos\frac{\theta}{2}|H\rangle + \sin\frac{\theta}{2}\mathrm{e}^{\mathrm{i}\phi}\,|V\rangle \\
|V\rangle \rightarrow |B_2\rangle &= \sin\frac{\theta}{2}|H\rangle - \cos\frac{\theta}{2}\mathrm{e}^{\mathrm{i}\phi}\,|V\rangle \\
\rho_1 \rightarrow \rho_2 &= \left(\frac{1+p}{2}\right)|B_1\rangle\langle B_1| + \left(\frac{1-p}{2}\right)|B_2\rangle\langle B_2|
\end{aligned} \tag{3.15}$$

The light is then passed through a quarter-wave plate (QWP) at angle χ relative to the laboratory polarisation axis, defined by the orientation of a subsequent linear polariser. The light is then sent through freespace to a spectrometer, and spectra are recorded as a function of the QWP angle χ. This is equivalent to measuring the state against the measurement basis $|M\rangle$, given by:

$$|M(\chi)\rangle = \mathrm{QWP}(\chi)|H\rangle = \frac{1}{\sqrt{2}}(\mathrm{i} + \cos 2\chi)|H\rangle + \frac{1}{\sqrt{2}}\sin 2\chi\,|V\rangle \tag{3.16}$$

As such, the energy observed at the spectrometer will be

$$E(\chi) = \frac{\langle M|\hat{H}\rho_2|M\rangle}{\langle M|\rho_2|M\rangle} = \varepsilon + \frac{s}{2}\left(\frac{\big(\alpha_1(\chi) - \alpha_2(\chi)\big) + p}{1 + p\big(\alpha_1(\chi) - \alpha_2(\chi)\big)}\right) \tag{3.17}$$

where $\alpha_j(\chi) = \left|\langle M(\chi)|B_j\rangle\right|^2$. An expression for the deviation ΔE from the mean energy ε as a function of χ is thereby attained. For the QWP configuration, this gives:

$$\begin{aligned}
\alpha_1 - \alpha_2 &= \frac{1}{2}(\cos\theta\,(1 + \cos 4\chi) + \sin\theta\sin 4\chi\cos\phi - 2\sin\theta\sin 2\chi\sin\phi) \\
\Delta E(\chi) &= E(\chi) - \varepsilon \\
&= -\frac{s}{2}\left(\frac{2p + \cos\theta\,(1 + \cos 4\chi) + \sin\theta\sin 4\chi\cos\phi - 2\sin\theta\sin 2\chi\sin\phi}{2 + p\cos\theta\,(1 + \cos 4\chi) + p\sin\theta\sin 4\chi\cos\phi - 2p\sin\theta\sin 2\chi\sin\phi}\right)
\end{aligned} \tag{3.18}$$

By measuring the deviation in the exciton/biexciton energy for a number of values of χ, and performing a fit to Equation (3.18), it is thereby possible to extract values for the FSS, degree of polarisation, and the polarisation angle and phase. The resolution of the spectrometer is 60 μeV, so in order to resolve shifts in the FSS on the order of 1 μeV, Gaussian fits to the measured spectra are performed. In the experiments detailed in this thesis, measures were taken to make the polarisation introduced into the beam path to be as small as possible, and p can be taken to be negligibly small. This improves the fitting equation, removing singularities for certain values of θ and ϕ and thus increasing the reliability of the fitting algorithms, to give:

$$\Delta E(\chi) = \frac{s}{4}(\cos\theta\,(1 + \cos 4\chi) + \sin\theta\sin 4\chi\cos\phi - 2\sin\theta\sin 2\chi\sin\phi\,) \tag{3.19}$$

One such measurement of the FSS, corresponding to the central experimental QD of this and the next chapter, is plotted in Figure 3.6. It should be noted that the energy shifts for exciton photons are anticorrelated to the shifts of the biexciton photons, i.e. $\Delta E_{XX}(\chi) = -\Delta E_X(\chi)$. Therefore, to provide stronger statistics in the fitting to the theoretical curve, the fitting can be applied to the experimental data $\Delta E(\chi) = \big(\Delta E_{XX}(\chi) - \Delta E_X(\chi)\big)/2$, a technique that was utilised in Figure 3.6. The method described here enables timely characterisation of the FSS of a QD, providing an indication of whether or not the QD will be a suitable entanglement source.

3.3.2 Quantum dot selection

With the Mach Zehnder interferometer used in Section 2.3.3, and the setup for measuring the fine structure splitting described in Section 3.3.1, we had the tools to mass-characterise quantum dots suitable for teleportation. After surveying several hundred dots across six devices on the same chip, such a QD was found, with splittings between 7 and 12 μeV, and biexciton coherence times around 100 ps, depending on the applied bias voltage. This would be sufficient to temporally resolve both entanglement and two photon interference with the SNSPD detectors, and therefore be a viable entanglement source for a quantum relay.

The μPL spectrum of the QD, under the conditions used in the operation of the quantum relay and entanglement experiments, is shown in Figure 3.7. As explained in Section 2.3.1 of Chapter 2, the wavelength and intensity of the QD emission can be controlled through the quantum confined Stark effect[70,71], and this effect is demonstrated in Figure 3.8. The undesired background—the small peaks close to the XX line—arise due to relatively poor confinement of the hole wavefunction within the quantum dot, distancing the state from the idealised 'particle in a box' conditions.

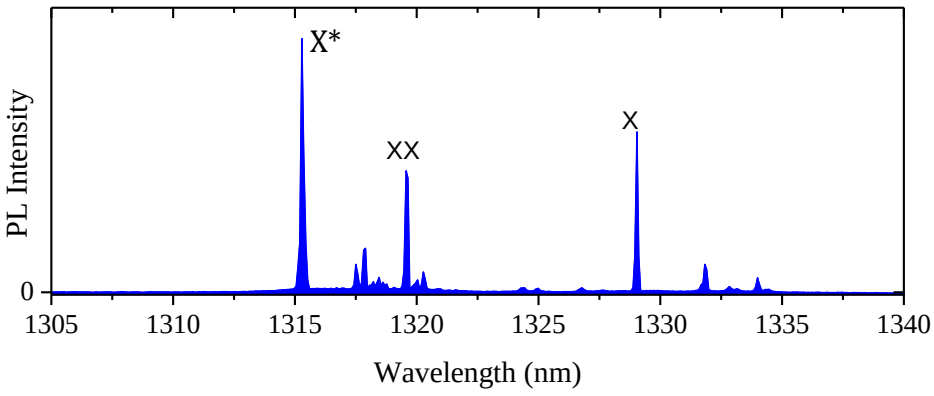

Figure 3.7: The μPL spectrum of the QD under the chosen experimental conditions, prior to being spectrally filtered. The QD is held under a bias of 0 V, and the excitation power is controlled such that, after the spectral filtering, the X and XX emissions have equal intensities at the SNSPDs. This spectrum is also shown in Huwer *et al.*[105].

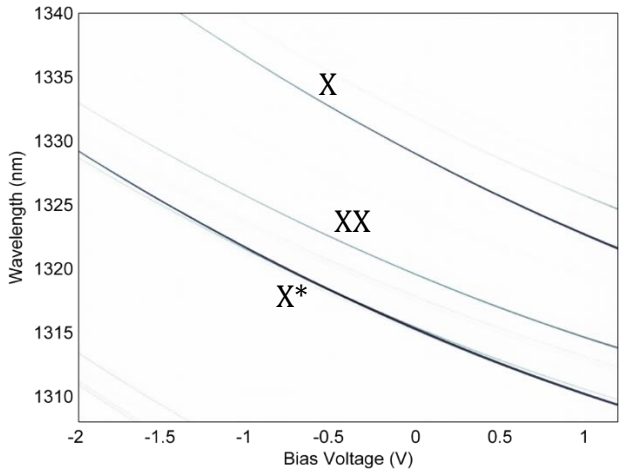

Figure 3.8: The μPL spectra under varying applied bias voltage, for the QD used in our quantum relay. Each excitonic transition varies by over nearly 20 nm in the displayed voltage range.

It is postulated that the coherence time increases with bias voltage due to a higher macroscopic field more successfully masking the local charge fluctuations that contribute to decoherence. In Figure 3.9 (b) it can be seen that the coherence time exhibits this behaviour, albeit less strongly and more erratically than similar measurements seen in Figure 2.13. This may be a result of the change from above band (~780 nm) excitation in Chapter 2 to below band (~1064 nm) excitation here, causing charge fluctuations to be more localised to the vicinity of the QD. The coherence time is also dependent on the excitation power, also shown in Figure 3.9, since more charges close to the dot are excited at higher powers, giving rise to a richer charge environment more prone to decohering the QD excitonic states.

The FSS depends on the macroscopic field applied, with the dependence shown in Figure 3.9 (a), and seems to be largely insensitive to local charge fluctuations, shown later in Figure 3.13. Unfortunately, desirably low FSS and high coherence time tune with the bias voltage in opposite directions. Ultimately, the experiment was operated at a bias of 0 V, in a compromise between reducing the FSS and increasing the coherence time.

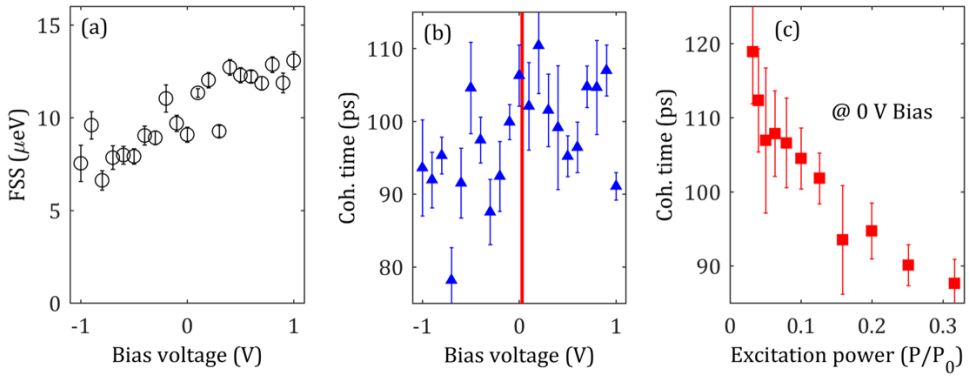

Figure 3.9: The dependence of the FSS and coherence time with the applied bias voltage, and coherence time with excitation power at a fixed voltage.

3.4 Observing Entanglement

3.4.1 Experimental setup

After finding a viable telecom-wavelength quantum dot, the next step towards measuring entanglement was to build and implement an experimental setup capable of filtering the desired modes, coupled into a set of time-resolving detectors with time-correlating electronics. This required spectral filtering, to spatially separate the exciton (X) and biexciton (XX) photons, and polarisation filtering, to observe correlations in the desired X and XX basis. Figure 3.10 is a representation of the setup used to measure entanglement between the X and XX photons, with as much of the apparatus kept in-fibre as practical.

In the experiment, a 1064 nm CW laser excites the QD source, with a constant bias voltage applied to the QD. A longpass dichroic mirror (DM) is used to inject the exciting laser photons, while a second DM is placed at 90° to the beam path to compensate for the birefringence on the collected photons introduced by the first DM. The X and XX lines are spectrally filtered at a transmission diffraction grating (TDG), sending the two modes into separate fibre arms, with an efficiency of 60 %. A pair of electronic polarisation controller (EPC) and polarising beam splitter (PBS) combinations are used to switch between the polarisation measurement bases. For calibration of the two EPCs, a movable mirror (MM) allows injection of a reference beam with a well-defined polarisation into the collection path of the experiment, achieved with spectrally broad O-band LED light, transmitted through a linear polariser (LP), half-wave plate (HWP), and quarter-wave plate (QWP) combination, to deterministically generate arbitrary polarisations.

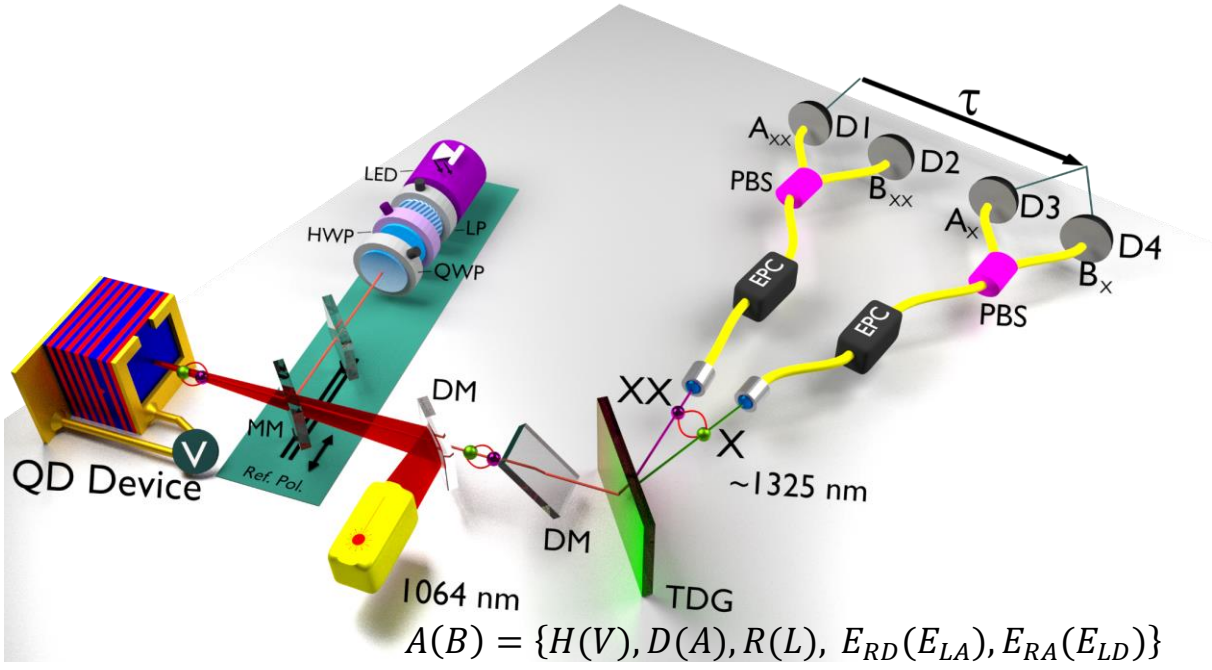

Figure 3.10: The experimental setup used to measure entangled photon pairs from our quantum dots.

Not shown in Figure 3.10, the collected QD photons can be sent either to the TDG, or to an InGaAs spectrometer. By feeding the QD light through an LP immediately after the compensating DM, and adjusting the LP angle such that the X or XX line was shifted to one of the expected extremes ($\Delta E = \pm s/2$), the spectrometer was only measuring light from one of the H or V eigenstates of the QD emission. Then, switching back to the SNSPDs with the LP still in place, injecting the LED reference polarisation into the beam path, and searching for the reference polarisation setting corresponding to a minimized signal at all four SNSPDs (but in practice, minimizing to one each of D1/D2, and D3/D4), the LED light is now aligned to the eigenbases of the X and XX emissions. The LED reference light can now be deterministically set to H, V, D, A, R, L, or any combination thereof. Finding the X and XX EPC settings that maximize or minimize the signal for to one each of D1 or D2, and D3 or D4, for a given reference polarisation (this time without the inserted LP), means that the SNSPD/EPC/PBS combinations have been calibrated to that polarisation measurement basis. This calibration step was found to be necessary, as the EPCs are not deterministically polarising elements.

With the EPCs calibrated and the MM removed from the beam path, a histogram of start-stop times between detecting an A_{XX} photon and an A_X(B_X) photon is recorded, providing us with the second-order cross-correlation functions with which to ascertain the entanglement fidelity. When measuring entanglement, the bases for the X and XX photons observed are always collinear. In total, five polarisation bases are alternately observed: the rectilinear (HV), diagonal (DA), and circular (LR) bases, and two elliptical bases, $E_{RD}E_{LA}$ and $E_{RA}E_{LD}$, in order to give information on the fidelity of the time-evolving entanglement of the emission, per Equation (3.11).

3.4.2 Entanglement excitation conditions

It is of interest to optimise the excitation conditions such that the entanglement correlations are as long lived and with as high amplitude as possible, while still performing the experiment in a practical timeframe. From the FSS values measured in Figure 3.9, it is judged that operating under a bias of 0 V is an adequate compromise between high intensity (roughly 100 kcps at each detector), low FSS (9.5 ± 0.8 μeV), and high coherence time (about 100 ps).

The variation of entanglement quality with excitation power was also investigated. Figure 3.11 shows polarisation correlation measurements under extremes of tolerable excitation power: not so low that impractical timeframes are required to perform the measurements, but not so high that the emission becomes saturated and a strong uncorrelated background arises. The characteristic oscillations are present in the superposition bases, as expected in the model from Section 3.2.1. There are also some weak oscillations in the nominally rectilinear correlations. Comparing to the model, this could be explained by the LED calibration beam deviating from the polarisation eigenstates of the QD by about $\pi/20$.

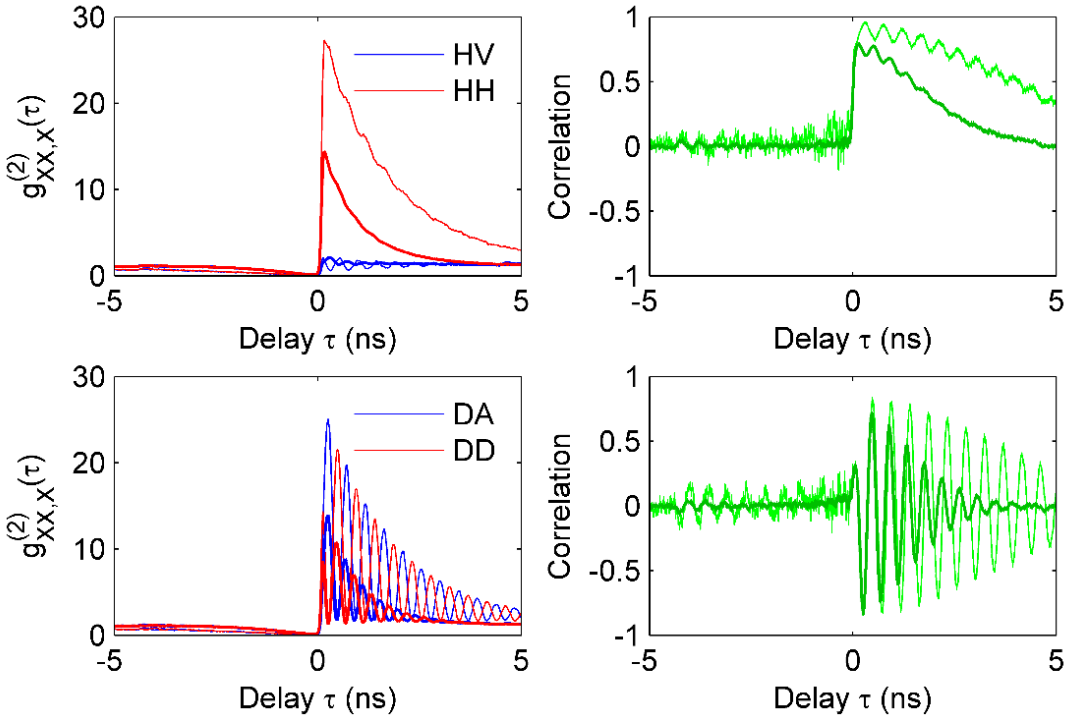

Figure 3.11: Cross-correlations and their correlation coefficients measured from the setup in Figure 3.10, for low power excitation (thinner lines) and high-power excitation (thicker lines). Co-polarised (red) and cross-polarised (blue) measurements were taken in the rectilinear and diagonal bases, showing the behaviour expected from Equations (3.6) and (3.7), as plotted earlier in Figure 3.3.

Several properties of the power dependence are noted, as plotted in Figure 3.13. Firstly, the correlation coefficient dies off more quickly for the higher power. This is due to the relative increase of the contribution of the uncorrelated background, as the exciton state gets reexcited more readily before decaying. For the same reason, the cross-correlation peak around zero increases for lower laser power, meaning that a higher proportion of the biexciton photons are being emitted as part of a coherent two-photon cascade. Lastly, the FSS increases slightly with increasing excitation power, but is always inside the initial estimate obtained from the quarter-wave plate polarimeter described in Section 3.3.1. It can be postulated that this is due to more charge carriers being excited in the vicinity of the QD, producing an average electric field opposite in direction to the applied field. This means that, when performing runs of the entanglement experiment and the quantum relay, the excitation conditions must be as similar as possible, to make the results directly comparable. The solution to this problem was to adjust the excitation such that the X and XX beams were equal to a chosen ratio of their respective saturation intensities at the spectrometer. This allows for any difference in the efficiency in the collection optics, which was liable to change due to removal and replacement of the cryostat in between experimental runs, leading to the QD being observed at slightly differing angles.

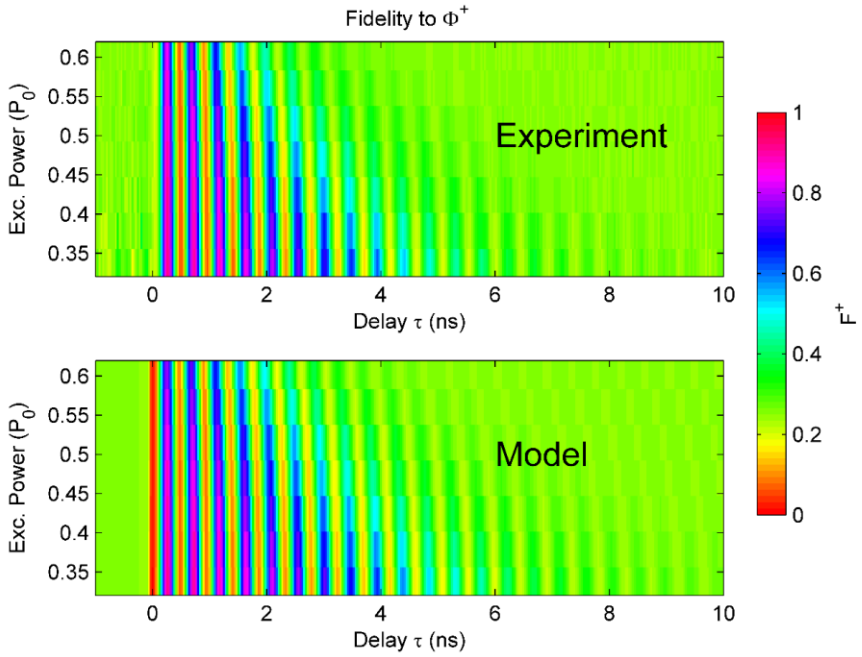

Figure 3.12: Plots of entanglement fidelity to the Φ^+ Bell state, as measured in the setup Figure 3.10, for a range of excitation powers. The data in Figure 3.11 corresponds to the two extremes of excitation power here. The model fits were extracted by fitting Equations (3.6), (3.7), and (3.8) to the measured correlations for each excitation power. The model fits show good qualitative agreement with the experimental fidelities, save for immediately at the zero-delay due to a finite relaxation time between the XX and X levels.

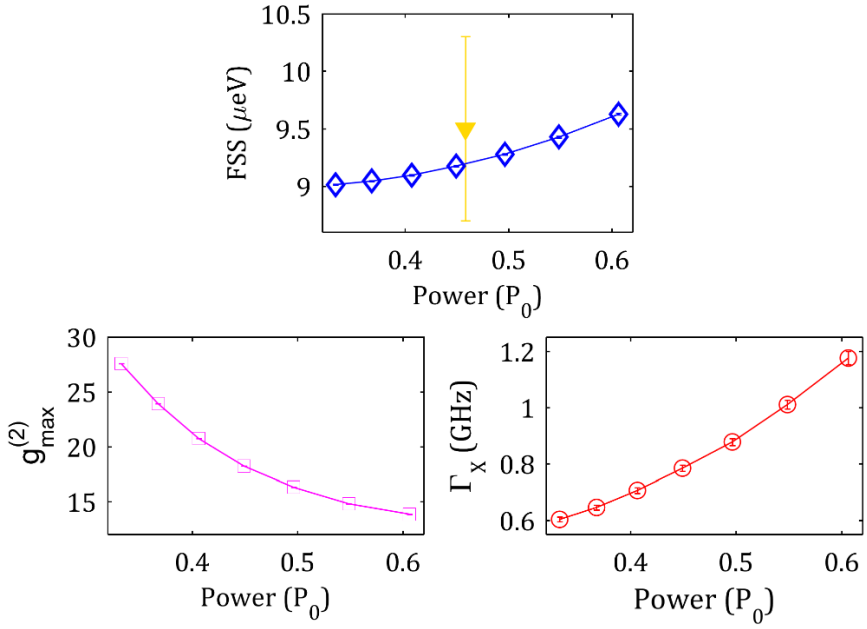

Figure 3.13: Parameters extracted from the model fits to the experimental data in Figure 3.12. Interestingly, the FSS varies slightly with excitation power, but still within the margin of uncertainty of the initial spectrometer FSS measurement (yellow triangle). The bunching efficiency $g^{(2)}_{max}$ and the exciton decay rate Γ_X also improve with lower excitation power.

3.5 Time-evolving entanglement

3.5.1 Second-order polarisation cross-correlations

Having chosen the experimental conditions for the entanglement measurements, namely the applied bias voltage and excitation power, it was possible to fully probe the time-evolving two-photon entangled state being emitted from the quantum dot. From Figure 3.11 it is already clear that the polarisation correlations evolve closely as predicted by the model in Section 3.2.1, with an exponential decay arising from the extent of the photon wavepackets, and oscillations arising from the fine structure splitting.

Equations (3.11) and (3.12) give expressions for the entanglement fidelity and Bell parameter for a state of the form $|\Phi(\phi)\rangle = (|HH\rangle + \exp(i\phi)\,|VV\rangle)/\sqrt{2}$. Choosing $\phi = 0$ or π is equivalent to the Φ^+ and Φ^- Bell states, respectively. Choosing $\phi = s\tau/\hbar$, however, corresponds

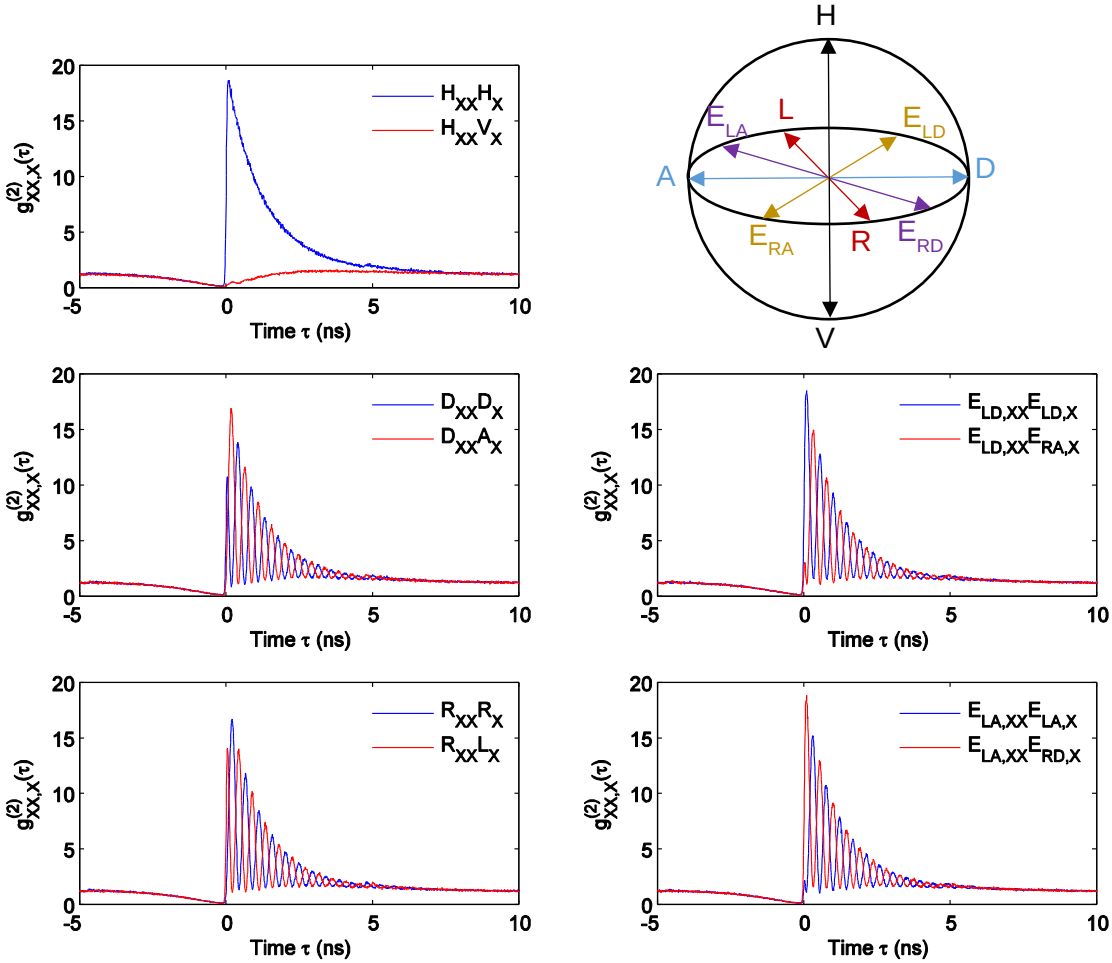

Figure 3.14: The second order correlation functions measured in the experimental setup described in Figure 3.10. The five polarisation bases are illustrated in the Poincaré sphere at the top right of this figure. Co-polarised correlations are plotted in blue, and cross-polarised correlations in red.

to a time-evolving maximally entangled state, which we expect our QD two-photon state to be close to. Equations (3.11) and (3.12) in general require five sets of correlations: measurements in the rectilinear, diagonal, circular, and two complementary elliptical bases. Figure 3.14 shows these five pairs of cross-correlation measurements. The rectilinear correlations are considerably smoother than in Figure 3.11, and any uncorrelated oscillatory contributions now have a small amplitude, close to the idealised case demonstrated in Figure 3.3, indicating a better degree of calibration. This was thanks to lessons learned in calibration of the polarisation reference beam, which also meant that better calibration of the EPCs for the superposition bases relative to Section 3.4.2 could be achieved.

The rectilinear measurements demonstrate the strongest correlations, since they are not affected by the precession of the entangled state. The other four plots in Figure 3.14, however, all show measurements for superposition states, and as such exhibit oscillations from the accrued phase, proportional to the product of the FSS s and the time delay τ. The image in the top right of the figure illustrates where the measured polarisations come from on the single-qubit Poincaré sphere, for the five basis pairs. From these measurements, it is possible to extract the fidelity of the two-photon state to a maximally entangled $\Phi(\phi)$ state, and to evaluate the Bell parameter $S_B(\phi)$.

3.5.2 Entanglement fidelity

The correlation coefficients are extracted from the normalised data in Figure 3.14 per Equation (3.8), as shown in Figure 3.15 (a), demonstrating the same oscillatory behaviour of the superposition states, and the enveloping decaying behaviour of the rectilinear states, as has been observed in Section 3.4. The rectilinear correlation coefficient reaches a peak of 97.5 ± 0.3 %, demonstrating the highly polarisation-correlated nature of the emitted photon pairs. The four superposition bases all oscillate within the envelope of the rectilinear correlation coefficient, with successive shifts of π/4 between the diagonal, LD-RA elliptical, circular, and LA-RD elliptical bases, in that order. In fact, this data represents an overcomplete set of measurements to probe the entanglement fidelity of the two-photon state, only one of the elliptical bases is required, as discussed in the supplementary information of Ward *et al.*[27]. However, due to the symmetry of using these five sets of data in reducing the propagation of any undesired correlated background, it is preferred to employ all five bases.

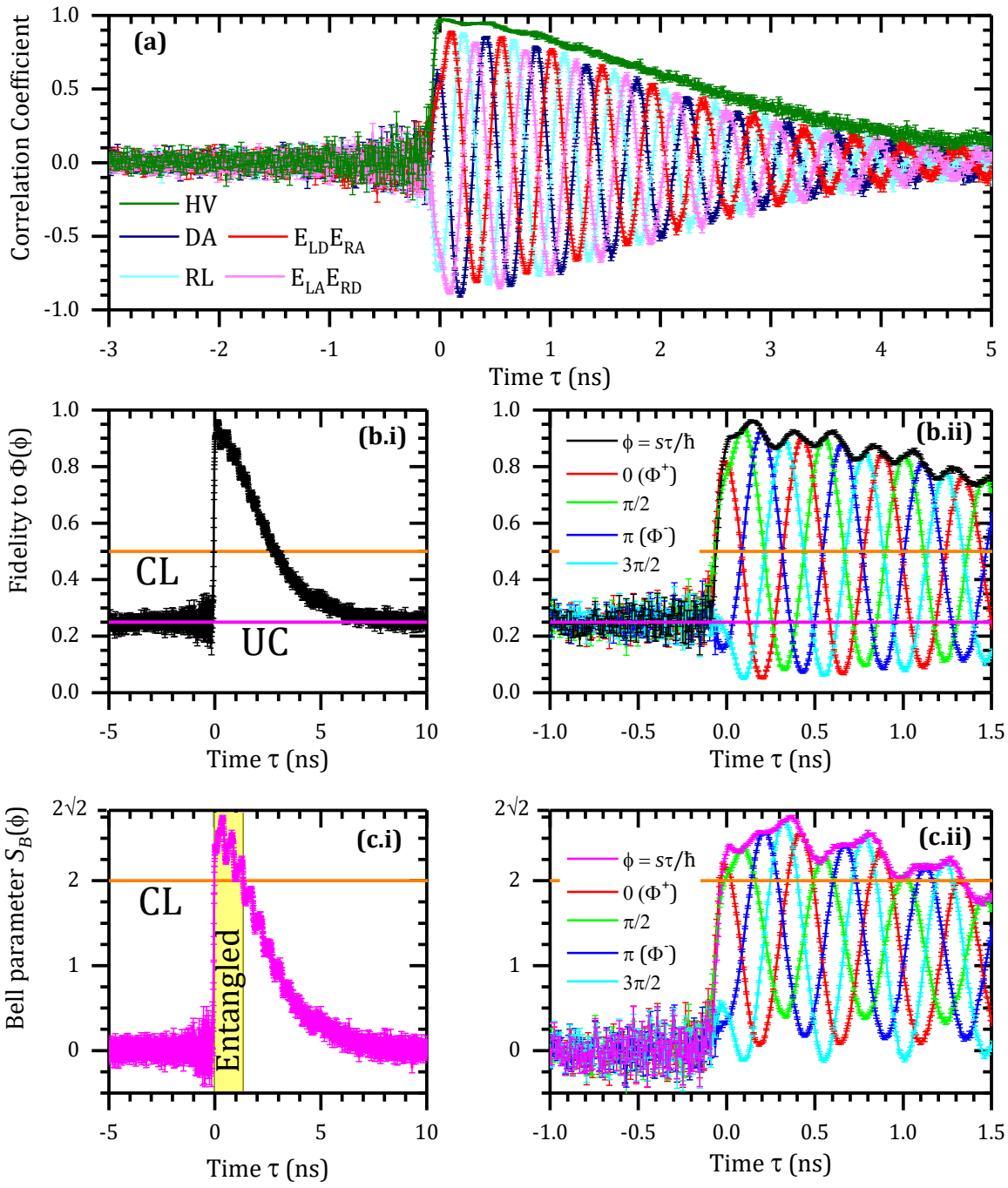

Figure 3.15: Important quantities extracted from the $g^{(2)}$ data in Figure 3.14. The correlations coefficients are shown in plot (a). The entanglement fidelity for the two $\Phi^{\pm}$ Bell states, plus two related entangled states, and a time-evolving maximally entangled state are shown in plots (b). The bottom two plots show the Bell parameter for four fixed phases and one time evolving phase. The data from (b) is also plotted in Huwer *et al.*[105].

From fits to these correlation coefficients, a more precise value of 9.05 ± 0.01 μeV for the fine structure splitting was measured. This value corresponds to observing the entanglement correlations oscillating with a period of 457 ± 0.5 ps. The entanglement fidelities, extracted from the correlation coefficients per Equation (3.11), to states of the form in Equation (3.10), are shown in Figure 3.15 (b). Five different values of ϕ are plotted. $\phi = 0$ and π correspond to the Φ^+ and Φ^- states, respectively, and only require measurements of the *HV, DA*, and *RL* bases. $\phi = \pi/2$ and $3\pi/2$, which are two alternative maximally entangled states, require measurements of the *HV*, $E_{LA}E_{RD}$, and $E_{LD}E_{RA}$ bases. In an idealised case of zero FSS and instantly fast detectors, we would see fidelities $F(\phi = 0) = 1$, $F(\phi = \pi) = 0$, and $F(\phi = \pi/2) = F(\phi = 3\pi/2) = 0.5$. As it is, all four states oscillate in time, alternately approaching unity and zero within phase shifts of $\pi/4$. The peak entanglement fidelities to these four static states are 90.1 ± 0.2 %, 93.4 ± 0.2 %, 92.0 ± 0.2 %, and 89.1 ± 0.2 %, for $\phi = 0, \pi/2, \pi$, and $3\pi/2$, respectively.

A non-oscillatory fidelity is achieved when $\phi = s\tau/\hbar$, where the probing of the entanglement is matched to the precession of the exciton state about the equator the Poincaré sphere. The fidelity of the two-photon state to this time-evolving entangled state peaks at 96.3 ± 0.3 %, and stays above the upper limit of 0.5 imposed by classical correlations for 2.74 ns, before descending into the uncorrelated regime at time delays away from zero. To our best knowledge, this constitutes a record-high entanglement fidelity for photon pairs from a quantum dot.

3.5.3 Violating Bell's theorem

The correlation coefficients also allow the evaluation of the Bell parameter, per Equation (1.2.11) as derived in Ward *et al.*[27]. The same five phases are considered, $\phi = 0, \pi/2, \pi$, and $3\pi/2$, as well as the time-evolving phase $\phi = s\tau/\hbar$, although they have a different significance in this context. As discussed in Section 3.2.3, Bell's theorem[75] governs differences between the predictions of classical systems and quantum mechanics, and violation of the relayed CHSH inequality[76], $|S_B| \leq 2$, can be considered a proof of Bell's theorem. The five different Bell parameters are plotted in Figure 3.15 (c), reaching peak values of 2.548 ± 0.011, 2.389 ± 0.012, 2.570 ± 0.009, and 2.704 ± 0.014 for the four static phases in ascending order, all individually violating the CHSH inequality at different times.

For the time-evolving state ($\phi = s\tau/\hbar$), the Bell parameter reaches a peak of 2.753 ± 0.013, violating the CHSH inequality by nearly 58 standard deviations. The Bell parameter of the time-evolving state stays above 2 for a total of 1.4 ns, comparable to the fluorescence lifetimes of the emitted photons, demonstrating the long-lived nature of the entanglement.

3.6 Conclusions

A model has been developed that qualitatively predicts the time evolution of the entangled emission from biexciton cascade of a quantum dot. This can be used to anticipate and characterise any imperfections in the polarisation calibration of a quantum relay.

Entanglement fidelities of 90.1 ± 0.2 % and 92.0 ± 0.2 % to the Φ^+ and Φ^- Bell states, respectively, were measured, more than sufficient to operate a quantum relay. Moreover, to a time-evolving entangled state, a peak fidelity of 96.3 ± 0.3 % was achieved, representing a record entanglement fidelity in photon pairs from a quantum dot light source. This time-evolving state exhibited correlations violating standard classical mechanics for a duration of 2.74 ns, and violated the CHSH inequality, a firm proof of quantum entanglement, for 1.4 ns.

From the results of Chapters 2 and 3, it has been shown that semiconductor QDs can emit pairs of highly entangled photons, and single photons that can be interfered with a dissimilar light source with high visibility, albeit in separate circumstances. The next step is to combine these two results and implement a quantum relay, which requires two-photon interference to perform a Bell state measurement, which heralds the teleportation of a qubit onto a photon entangled with one of the Bell state measurement inputs. This will be explored in the next Chapter.

Telecom-Wavelength Quantum Relay 4

4.1 Introduction

The means by which quantum key distribution (QKD) is made secure—the inability to observe a quantum state without disturbing it—is a double-edged sword. The no-cloning theorem states that it is impossible to make a copy of an arbitrary unknown quantum, precluding the analogue of a classical signal amplifier in a quantum channel (QC), limiting the distance that such a channel can span. Unamplified, there have been implementations of QCs as long as 260 km[20], but for practical key rates, QCs are limited to metropolitan distances of tens of kilometres[106].

A solution to this problem may lie in quantum teleportation, proposed by Bennet *et al.* in 1993[57]. Simply put, teleportation is a mechanism by which it is possible to copy an arbitrary quantum state from one quantum bit (qubit) to another, with the caveat that the information in the original qubit is automatically destroyed. In the first experimental realization of teleportation by Bouwmeester *et al.* in 1997[59], a spontaneous parametric down conversion (SPDC) source generates two pairs of entangled photons from the transmission and retroreflection of an ultraviolet pulse. The retroreflected photon-pair was used as a heralded single-photon source and filtered in polarisation, upon which a Ψ^- Bell state measurement (BSM) was performed between the polarised individual photon and one half of the other entangled photon-pair, such that the polarisation qubit became encoded on the other unmeasured entangled photon. Requirements for teleportation are a high level of indistinguishability between the photons in the two-photon measurement, and a high-fidelity entanglement resource. While this still won't allow a traditional amplifier to be implemented, the transmission distance of a quantum channel will potentially be increased because the noise is suppressed.

An implementation of this description is known as a quantum relay[21]. These have been demonstrated with quantum channels operating over both optical fibre[88,89,107–109] and free-space[110–112]. Spontaneous parametric down conversion sources[110,112] are typically used in teleportation experiments, but they propagate the statistics of the original source of photons, pulses from a laser. This leads to the increase of the error rate in a QC, due to unwanted multi-photon emission[113], compared to a single photon-pair emitter. To reduce the error rate in a quantum relay, either a source with sub-Poissonian statistics or single photon-pair heralding

techniques must be used. The latter possibility greatly reduces the efficiency of a quantum relay. More recently, implementations utilising decoy states[108] have also been performed as a means to mitigate the increased error introduced by multi-photon emissions.

Semiconductor quantum dots have been demonstrated to be excellent sources of single photons and singe entangled pairs[37–39], with the benefit of being electrically excitable[47] and embedded in a solid-state architecture. A quantum relay with such a device was recently demonstrated over 1 km of fibre, albeit operating at 886 nm[46], with high teleportation fidelities well above the lower limit required for strong error correction algorithms[17,114]. Considerable advances have been made in extending the emission wavelength of the QDs towards the low-absorption windows in optical fibre, the O-band (1260—1360 nm, ~0.3 dB/km) and the C-band (1530—1565 nm, ~0.2 dB/km)[96,98,115]. The results of Chapters 2 and 3, though pertaining to two different QDs, demonstrate the main technical requirements to implement a QD-based O-band quantum relay. The experimental work in this chapter was performed in collaboration with Dr. Jan Huwer of TREL, using a QD device processed by Dr. Joanna Skiba-Szymanska, also of TREL. At the time of writing this thesis, a paper summarising the results of this chapter is under review for publication[105].

4.2 Background

4.2.1 Quantum teleportation

Bennet *et al.*[57], who first presented the idea of quantum teleportation, provide a treatment of how an unknown quantum state can be sent between two remote nodes of a quantum network, where the qubits in transit are in no way encoded. In line with the conventions of quantum information, the qubit is sent by a source named Alice to a recipient named Bob. Alice and Bob have arranged to have possession of a shared EPR[74] pair. Alice has an additional principally unknown qubit, expressed in terms of the computational basis with a general form of

$$|\psi\rangle = \cos\alpha|0\rangle + e^{i\beta}\sin\alpha\,|1\rangle \tag{4.1}$$

Here, 0 and 1 can be any pair of orthogonal states. The shared EPR pair can be any pair of entangled quantum states, but it is useful to consider the Bell states[75], which make up a complete basis of orthonormal and maximally entangled two-qubit states. The four Bell states are:

$$\begin{aligned}|\Phi^{\pm}\rangle &= \frac{1}{\sqrt{2}}(|00\rangle \pm |11\rangle)\\ |\Psi^{\pm}\rangle &= \frac{1}{\sqrt{2}}(|01\rangle \pm |10\rangle)\end{aligned} \tag{4.2}$$

In this treatment, we take the EPR pair to be in the symmetric Bell state $|\Phi^{+}_{AB}\rangle = (|0_A 0_B\rangle + |1_A 1_B\rangle)/\sqrt{2}$, which corresponds to the emission that will be seen from a quantum dot in the rectilinear polarisation basis, where the subscripts A and B refer to the quantum possessed by Alice and Bob, respectively. If the unknown qubit (with subscript U) is indistinguishable to Alice's half of Φ^{+} state, the combined three-photon state can then be expressed as $|T_{UAB}\rangle = |\psi_U\rangle\otimes|\Phi^{+}_{AB}\rangle$, or

$$|T_{UAB}\rangle = \frac{1}{2}\{|\Phi^{+}_{UA}\rangle\otimes|\psi_B\rangle + |\Phi^{-}_{UA}\rangle\otimes\sigma_z|\psi_B\rangle + |\Psi^{+}_{UA}\rangle\otimes\sigma_x|\psi_B\rangle - i|\Psi^{-}_{UA}\rangle\otimes\sigma_y|\psi_B\rangle\} \tag{4.3}$$

where σ_i are the Pauli matrices

$$\sigma_x = \begin{pmatrix}0 & 1\\ 1 & 0\end{pmatrix}, \qquad \sigma_y = \begin{pmatrix}0 & -i\\ i & 0\end{pmatrix}, \qquad \sigma_z = \begin{pmatrix}1 & 0\\ 0 & -1\end{pmatrix} \tag{4.4}$$

As such, if Alice performs a Bell state measurement (BSM), Bob will now have an exact copy of the unknown qubit, within a unitary transformation, whereas both of quanta involved in the BSM will have been consumed. Figure 4.1 outlines this process. Alice's measurement constitutes a quantum non-demolition (QND) measurement, since no information of the state $|\psi\rangle$ is gained, but the successful teleportation is heralded and communicated to Bob over a classical channel.

Practically, it is not possible to perform a complete Bell state measurement with linear optics, only Ψ^{+} and Ψ^{-} can be ascertained unambiguously, limiting the efficiency of quantum teleportation here to 1/2. With non-linear optics, it is possible to perform a full Bell state

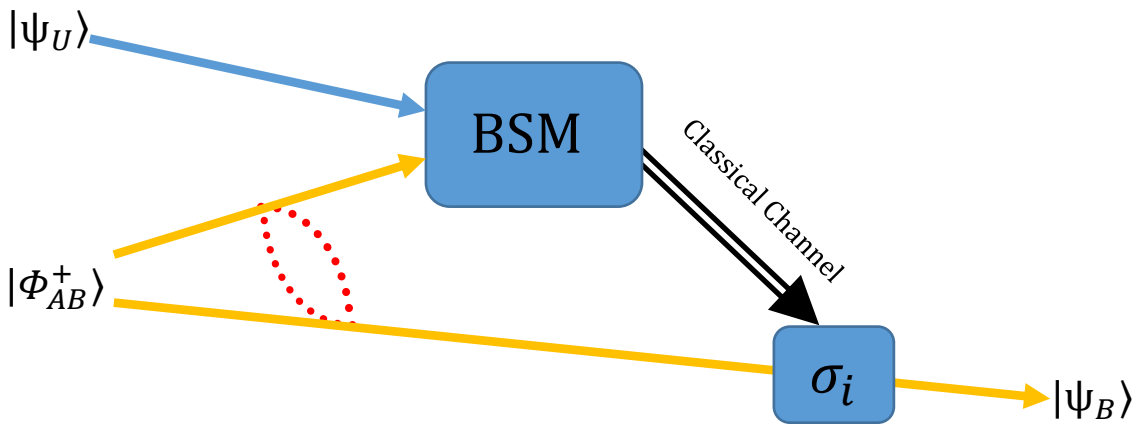

Figure 4.1: Teleportation for a Φ^+ Bell state entanglement resource. By performing a Bell state measurement (BSM), Alice knows which unitary correction Bob must make to his qubit such that he has an exact replica of the unknown input state $|\psi\rangle$, which she communicates to him over a classical channel.

measurement, but the non-linear effects cause the measurement to be even more inefficient. Figure 4.2 demonstrates a setup capable of teleporting a quantum state encoded as a photonic polarisation qubit. This setup performs a Ψ^+ measurement, successfully heralding teleportation in one quarter of cases.

Thus we have outlined a general picture of how a qubit is teleported from Alice to Bob. However, in order to discover the limits of such teleportation, it is important to consider the dynamics of real-world quantum sources. While having multitudinous causes, the deficiencies in a teleportation implementation all arise due to a level of distinguishability between the quanta, non-optimal fidelity of the entangled state, and deviation from the ideal Fock state regime.

4.2.2 Realistic teleportation

The above treatment makes exclusive use of pure, maximally entangled, and indistinguishable quantum states (although in general only the two particles taking part in the Bell state measurement need be indistinguishable). From this point on we will consider photonic qubits, as these are the best examples of flying qubits in a quantum network, thanks to the guiding effect in silica fibres and very low absorption at certain wavelengths (0.3 dB/km in the O-band, 1260-1360 nm[24], and 0.2 dB/km in the C-band, 1530-1565 nm[23]). In this context, the level of indistinguishability refers to the similarity of the spectral, spatial, temporal and polarisation modes, except for the mode in which the qubits are encoded. Here, the qubits will be encoded in the polarisations of the photons, so this is left freely varying. Spatial indistinguishability is achieved by use of single-mode optical fibre, and spectral indistinguishability is achieved by

tuning the wavelength of the light sources until they are spectrally overlapped. It is therefore useful to consider the photons in the spatio-temporal domain, as explored in Legero *et al.*[68].

The teleportation circuit as used in this chapter's work is displayed in Figure 4.2. Under ideal circumstances, the entanglement resource used to mediate the teleportation will be two photons in the Φ^+ Bell state. However, due to the fine structure splitting (FSS) in the excitonic level of a quantum dot (QD) as discussed in Chapter 3, the biexciton-exciton photon pairs have a time-evolving, but still maximally entangled, state of the form

$$|\Phi(\tau_1,\tau_2)\rangle = \frac{1}{\sqrt{2}}\left(|H_2H_3\rangle + \exp\left(\frac{is(2\tau_2-\tau_1)}{2\hbar}\right)|V_2V_3\rangle\right) \tag{4.5}$$

where s is the FSS and $(2\tau_2-\tau_1)/2$ is the time between detection of a biexciton (XX) photon and an exciton (X) photon in the teleportation circuit of Figure 4.2, taken as an average due to the indistinguishability of biexciton and laser photons. Again considering an unknown input state of $|\psi\rangle = \cos\alpha\,|H\rangle + e^{i\beta}\sin\alpha\,|V\rangle$ (where 0→H and 1→V from Equation (4.1)), the three-photon input state into the teleportation circuit is

$$\begin{aligned}|\Psi_{in}\rangle &= \frac{1}{\sqrt{2}}\left(\cos\alpha\,|H_1\rangle + e^{i\beta}\sin\alpha\,|V_1\rangle\right)\left(|H_2H_3\rangle + e^{is(2\tau_2-\tau_1)/2\hbar}|V_2V_3\rangle\right)\\ &= \frac{1}{\sqrt{2}}\left(\cos\alpha\,a_{1H}^\dagger + e^{i\beta}\sin\alpha\,a_{1V}^\dagger\right)\left(a_{2H}^\dagger a_{3H}^\dagger + e^{is(2\tau_2-\tau_1)/2\hbar}a_{2V}^\dagger a_{3V}^\dagger\right)|0\rangle\end{aligned} \tag{4.6}$$

A photon in spatial mode i with polarisation B has the field operator $\hat{E}_{iB}^+$, given in terms of the temporal modefunctions $\zeta_{iB}(t)$ and annihilation operator a_{iB} by:

$$\hat{E}_{iB}^+(t) = \zeta_i(t)a_{iB} \tag{4.7}$$

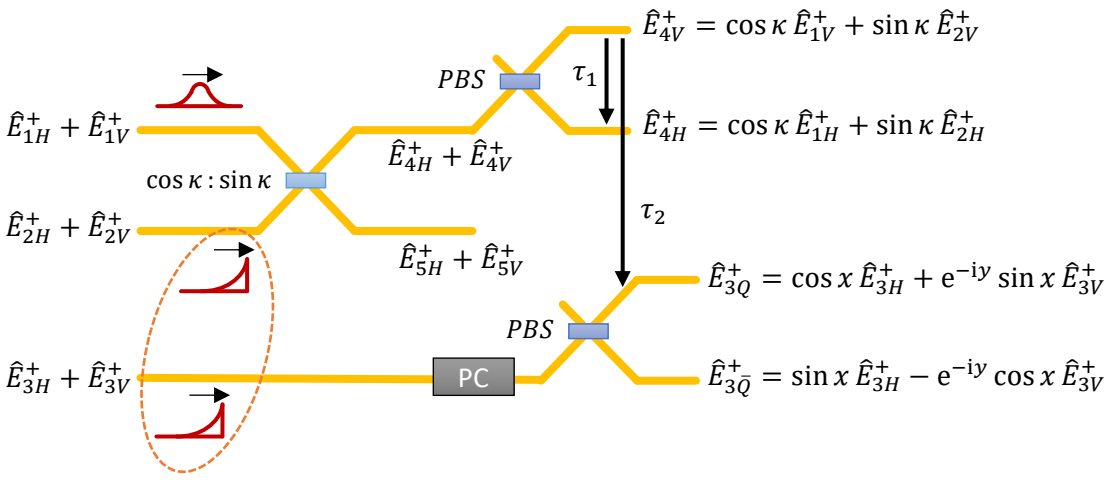

Figure 4.2: The teleportation circuit, in which an encoded laser photon in mode 1 is interfered with the biexciton photon (mode 2) of an entangled pair, such that the qubit is recovered in the exciton photon (mode 3), aside from a unitary transformation.

Following the evolution of the field operators through the configuration of beam splitters and polarising beam splitters in the teleportation circuit, the probability of detecting photons in mode $4V$ at time t, mode $4H$ at time $t+\tau_1$, and mode $3Q$ at time $t+\tau_2$ is given by:

$$\begin{aligned} p_Q(t,\tau_1,\tau_2) &= \langle\Psi_{in}|\hat{E}^-_{4V}(t)\hat{E}^-_{4H}(t+\tau_1)\hat{E}^-_{3Q}(t+\tau_2)\hat{E}^+_{3Q}(t+\tau_2)\hat{E}^+_{4H}(t+\tau_1)\hat{E}^+_{4V}(t)|\Psi_{in}\rangle \\ &= \left|\langle 0|\hat{E}^+_{3Q}(t+\tau_2)\hat{E}^+_{4H}(t+\tau_1)\hat{E}^+_{4V}(t)|\Psi_{in}\rangle\right|^2 \\ &= \frac{\sin^2 2\kappa}{8}|\zeta_3(t+\tau_2)|^2 \Big|\cos\alpha \sin x\, \zeta_2(t)\zeta_1(t+\tau_1) \\ &\quad + \sin\alpha\cos x\, \mathrm{e}^{\mathrm{i}\left(\beta+y-\frac{s(2\tau_2-\tau_1)}{2\hbar}\right)}\zeta_2(t+\tau_1)\zeta_1(t)\Big|^2 \end{aligned} \tag{4.8}$$

Practically, the input photon and one of the EPR pair photons are interfered, at a $\cos^2\kappa:\sin^2\kappa$ beam splitter, and a Ψ^+ Bell state measurement is performed. The remaining target photon is measured, after projecting it into the polarisation state $|Q\rangle = \cos x\,|H\rangle + \mathrm{e}^{\mathrm{i}y}\sin x\,|V\rangle$, as shown in the teleportation circuit. Nominally, the input state will have been mapped onto the target photon as $\sigma_x|\psi\rangle$, but in reality, there will only be some relative delays τ_1 and τ_2 where this holds true, mostly limited by the temporal distinguishability of the two BSM photons, and the FSS of the entanglement resource. However, it is possible to predict how the size of this time window will vary with these effects.

4.2.3 Teleportation with a QD entanglement source

We take the following three modefunctions for our three photons, corresponding to laser (L) photons in mode 1, biexciton (XX) photons in mode 2, and exciton (X) photons in mode 3, respectively:

$$\begin{aligned} \zeta_1(t) &= A_1 \exp\left(-\frac{(t-t_0)^2}{2\sigma^2} - i\omega_L t\right) \\ \zeta_2(t) &= A_2 \exp\left(-\frac{\Gamma_{XX}t}{2} - \mathrm{i}\left(\omega_{XX}t + \Phi_{XX}(t)\right)\right)\Theta(t) \\ \zeta_3(t) &= A_3 \exp\left(-\frac{\Gamma_X t}{2} - \mathrm{i}\left(\omega_X t + \Phi_X(t)\right)\right)\Theta(t) \end{aligned} \tag{4.9}$$

where ω_i is the central frequency of the photon, Γ_i is the decay rate of the X or XX level, and $\Theta(t)$ is the Heaviside step function. The functions $\Phi_i(t)$ is a random phase term contributing $\langle\exp(\mathrm{i}[\Phi_i(t)-\Phi_i(t+\tau)])\rangle = \exp\left(-|\tau|/T_{2,i}\right)$, for a pure dephasing time $T_{2,i}$. For the moment, the laser photons are treated as weak pulses, but this will be extended into the continuous-wave (CW) regime by working in the limit of $\sigma\to\infty$.

There is a $\sin^2(2\kappa)/8$ chance of having one photon in each of modes $4V$ and $4H$, so to find the conditioned probability $P_Q(\tau_1,\tau_2)$ of finding a photon in mode $3Q$ at delay τ_2, given the detection of a photon in mode $4V$ at delay zero and another in mode $4H$ at delay τ_1. Integrating

$p_Q(t,\tau_1,\tau_2)/(\sin^2(2\kappa)/8)$ over all time t, in the limit of $\sigma \to \infty$, and again taking $\Gamma_{XX} \gg \Gamma_X$ as in Section 3.2.1, we arrive at an expression for this conditioned probability:

$$\begin{aligned} P_Q(\tau_1,\tau_2) &= \lim_{\sigma\to\infty} \int_{-\infty}^{\infty} \mathrm{d}t\, p_Q(t,\tau_1,\tau_2) \Big/ \left(\frac{\sin^2 2\kappa}{8}\right) \\ &= \sin^2 x \cos^2 \alpha \exp(-\Gamma_X \tau_2)\, \Theta(\tau_2) \\ &\quad + \cos^2 x \sin^2 \alpha \exp\big(-\Gamma_X(\tau_2-\tau_1)\big)\, \Theta(\tau_2-\tau_1) \\ &\quad + \frac{1}{2} \mathrm{e}^{-\frac{|\tau_1|}{\tau_c}} \sin 2x \sin 2\alpha \cos\left(\beta + y + \Delta\omega\tau_1 - \frac{s(2\tau_2-\tau_1)}{2\hbar}\right) \\ &\qquad \times \left(\mathrm{e}^{-\Gamma_X|\tau_2-\tau_1|}\Theta(\tau_2-\tau_1,-\tau_1) + \mathrm{e}^{-\Gamma_X|\tau_2|}\Theta(\tau_1,\tau_2)\right) \end{aligned} \tag{4.10}$$

From these expressions, several things are evident. Linearly polarised control states, *H* and *V*, corresponding to $\alpha = 0$ or $\pi/2$, will be teleported independent of the fine structure splitting and coherence time. This occurs because the BSM has been chosen to overlap with the eigenbasis of the QD emission, and the precession induced by the FSS manifests as a global phase. Away from these poles, however, and the teleportation probability will oscillate in time. Correlations between control states on the equator of the Bloch sphere ($\alpha = \pi/4$) observed in some equatorial basis ($x = \pi/4$), will oscillate with maximal amplitude. We can anticipate that τ_c will be a limiting factor in the extent of teleportation of superposition states for τ_1 delays ($1/\Gamma_X$ is typically much larger than τ_c), and that the limiting factor in τ_2 delays will be the FSS, with oscillations of period h/s.

Aside from the polarisation angles, there are three parameters in Equation (4.10) for which there is a degree of control under experimental conditions. The fine structure splitting and coherence time can both be varied by application of an electric field normal to the QD growth surface, as discussed in Chapter 3, Section 3.3.2, although unfortunately they each improve with opposite tuning of the field. The spectral detuning between the biexciton and laser photons is another controllable parameter, either with the biexciton wavelength varied via the quantum confined Stark effect[70,71], (shown in Chapter 3, Section 3.3.2), or by fine-tuning the length of the laser's optical cavity, a capability common in commercial diode lasers. Since an electric field was already being utilised to optimize the FSS and coherence time, it was elected to utilise the wavelength tuning ability of an O-band tunable diode laser. Figure 4.3 demonstrates how the conditioned probability P_Q depends on the FSS and the polarisation measurement basis.

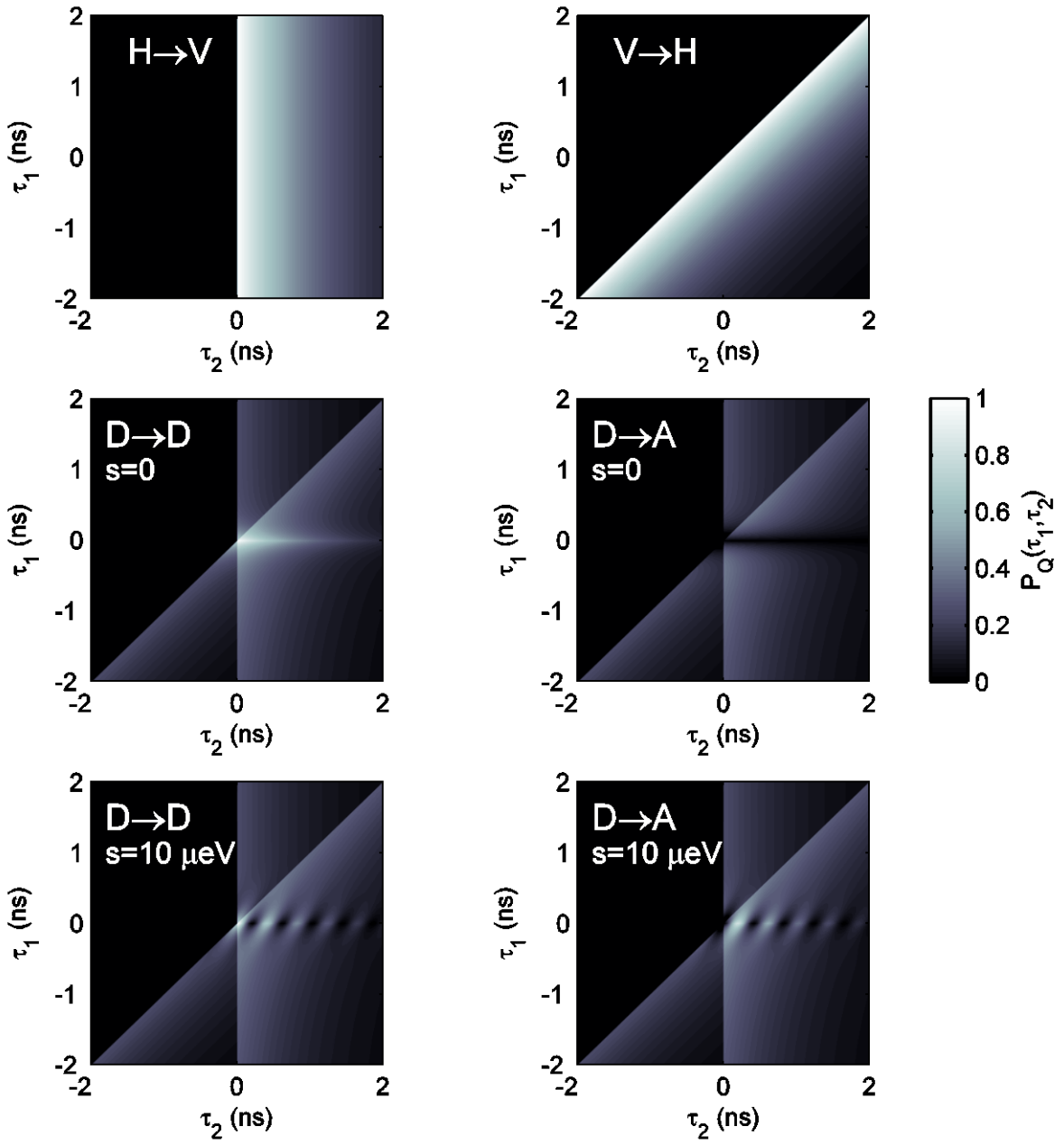

Figure 4.3: The conditioned probability of finding a photon in mode $3Q$ of for a given input polarisation in mode 1, as a function of Bell state measurement delay time τ_1 and exciton delay time τ_2, per Equation (4.10). The top two plot show 'trivial' teleportation of the two rectilinear polarisations, explicable through classical optics. The central two plots show the enhanced $(D \to D)$ and diminished $(D \to A)$ probability of observing a superposition state $(D = (H + V)/\sqrt{2})$ according to the measurement basis, near $|\tau_1| \lesssim \tau_c$ for zero FSS. The bottom two plots again show a superposition input state D, but now with a finite FSS, giving rise to anticorrelated oscillations in the D and A measurement bases.

Up to now, it has been assumed that the photons all obey single-photon statistics. However, the laser photons have Poissonian statistics, with possible multi-photon emissions, and the quantum dot light may not be an ideal single-photon source. Due to the excitonic states in the quantum dot not being a truly isolated system, there exists some coupling with their external environment, such that their statistics will deviate from the ideal Fock state picture at delay times away from zero. Including contributions due to uncorrelated exciton-biexciton-laser coincidences, accidental exciton-laser-laser coincidences, and accidental exciton-biexciton-biexciton coincidences, we arrive at an expression for the third-order correlation function that we will measure:

$$g^{(3)}_{HVQ}(\tau_1,\tau_2) \propto \eta_L\eta_X\eta_{XX}\left(g^{(2)}_C(0)P_Q(\tau_1,\tau_2)+\frac{1}{2}\cos^2\alpha\, g^{(2)}_{UC}(\tau_2) + \frac{1}{2}\sin^2\alpha\, g^{(2)}_{UC}(\tau_2-\tau_1)\right)+\frac{1}{2}\eta_L^2\eta_X+2\eta_{XX}^2\eta_X g^{(3)}_{2XX,X}(\tau_1,\tau_2) \tag{4.11}$$

where the η_i terms refer to the time-averaged intensity of each beam. The $g^{(2)}_{UC}(\tau)$ uncorrelated cross-correlations are precisely the same function as discussed in the Section 3.2.2 (Equation (3.7)), related to the probability of observing the 'wrong' polarisation in the entangled pair. The $g^{(3)}_{2XX,X}$ term takes into account triple-coincidences involving pairs of correlated X and XX photons and an additional uncorrelated XX photon, arising due to reexcitation of the QD to the biexciton level. This expression takes into account the Poissonian statistics of the laser photons, reexcitation of the QD, and the adiabatic dephasing of the QD photons. These non-ideal contributions were taken from Varnava *et al.*[46], which provides a more general treatment for teleportation with pulsed light sources.

4.3 The Quantum Relay

From what has been learned from the work of Chapters 2 and 3 in high-visibility two-photon interference and high-fidelity quantum entanglement between pairs of photons, both at telecom wavelengths, it should now be practically possible to implement a telecom-wavelength quantum relay. According to the theoretical treatment in Section 4.2.3, the limiting factors will be the exciton (X) fine structure splitting and the coherence time of the biexciton (XX) photons. Additionally, in order to build up sufficient statistics in a sensible time frame, light sources with intensities above a certain threshold are needed. As an initial estimate, to observe one triple coincidence per hour in a square time bin of $\Delta\tau_1 \times \Delta\tau_2 = \tau_c \times (h/4s)$, where the splitting s is 9.05 μeV and the coherence time τ_c is 95 ps, would require detected photon rates of at least 140 kHz for each of the exciton, biexciton, and laser emissions.

Fortunately, we have such a source, in the form of the same InAs/GaAs quantum dot used to observe quantum entanglement in the telecom O-band in Chapter 3. This QD is described and characterised in detail in Section 3.3, and shown to emit entangled photon-pairs in Sections 3.4 and 3.5. Under the experimental conditions chosen for the quantum relay, the biexciton and exciton photons are at wavelengths of 1319.5 nm and 1329.0 nm, respectively, the exciton FSS is 9.05 ± 0.01 μeV, and the biexciton coherence time was measured as 95 ± 8 ps, hence the values used in the previous paragraph's estimate calculation. The biexciton and exciton photon streams have intensities of 300 kHz and 400 kHz, respectively. This is roughly a factor two increase compared to the minimum requirement, so we should see approximately eight times as many coincidences, since the rate of triple coincidences scales with the cube of the combined intensities.

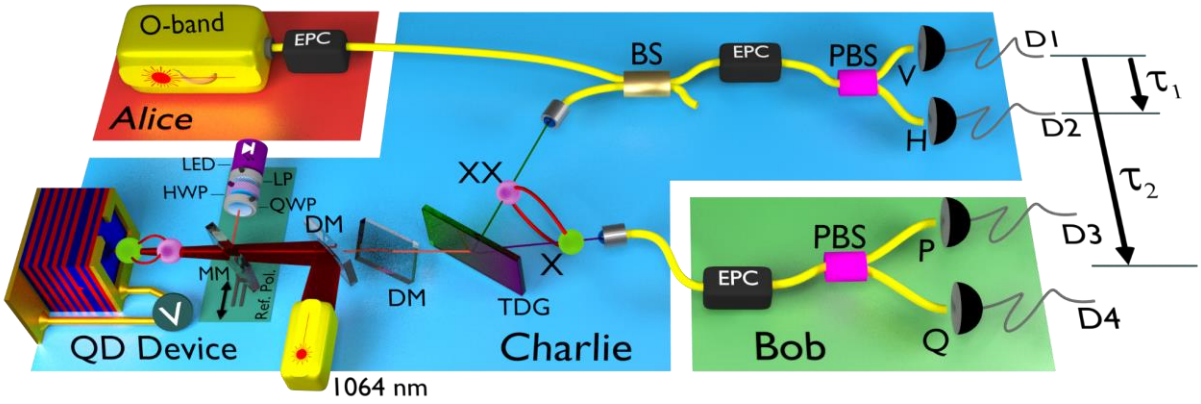

Figure 4.4: (Presented similarly in Huwer *et al.*[105]) The experimental setup of our quantum relay. Alice, Bob, and Charlie could in principle be separated by many kilometres of optical fibre.

The quantum relay setup, with the incorporated telecom-wavelength QD source, is presented in Figure 4.4. In line with conventions of QKD, the source of the control qubit is named Alice, the receiver of the target qubit is named Bob, and the node in between is named Charlie. A qubit is encoded in the polarisation of a weak coherent state by Alice, and sent into Charlie's node of the quantum relay. Meanwhile, Charlie is generating pairs of polarisation-entangled spectrally-distinct photons. One photon is sent to Bob, who measures the polarisation state of his photon, while Charlie performs a projective $\Psi^+\left(=[|HV\rangle + |VH\rangle]/\sqrt{2}\right)$ Bell state measurement on the other photon and Alice's flying qubit. A positive Ψ^+ result heralds the mapping of a control qubit from Alice onto a target qubit at Bob, without any encoded information being sent directly between Alice and Bob. More concisely, a qubit is teleported from Alice to Bob.

In the experiment, the QD device was excited with a CW 1064 nm laser, injected with a longpass dichroic mirror. In order to mitigate the wavelength-dependent birefringence and polarisation of the longpass mirror, a second identical dichroic mirror from the same coating batch was placed in the μPL beampath between the spectral filter and the injection mirror, oriented at 90° relative to the beampath. The μPL was spectrally filtered with a transmission diffraction grating such that the X and XX photons were spatially separated into different single mode fibres. Alice used a commercial O-band diode laser with a 400 kHz linewidth, with an attenuator and electronic polarisation controller to generate a beam of weak coherent photons with well-defined polarisations. Alice's laser photons and Charlie's XX photons impinged on a 96:4 non-polarising beam splitter, such that 96 % of the XX photons and 4 % of the laser photons were sent to a polarising beam splitter. A spectrometer was used to spectrally overlap the laser line with the XX photons, using Gaussian fits to overcome the instrument resolution of ~60 μeV, achieving a precision of ±480 MHz between the detuning of the two sources. The polarisation measurement bases at Charlie and Bob's detectors were calibrated using an O-band LED with a well-defined polarisation relative to the QD rectilinear eigenbases, as described n Section 3.4.1, by searching for settings of Charlie and Bob's EPCs that alternately extinguished the signal from the LED to D1 or D2, and D3 or D4. Alice calibrated the polarisation of her photons by setting her EPC to minimize the laser signal to one of D1 or D2, with Charlie's EPC set to the appropriate collinear measurement basis.

The detectors D1 to D4 are superconducting nanowire single photon detectors (SNSPDs), and the arrival times relative to a count at detector D1 were recorded with a 1 ps measurement precision using time-correlating electronics running in time-tagged-time-resolved mode. The times τ_1 and τ_2 in Figure 4.4 refer to the relative delays $t_{D2} - t_{D1}$ and $t_{D3/4} - t_{D1}$, respectively. From this data, histograms of triple coincidences according to their (τ_1, τ_2) times was constructed, and normalised to the mean values at delays $|\tau_{1,2}|, |\tau_2 - \tau_1| \gg 1/\Gamma_X$, to provide the

third-order correlation function $g^{(3)}(\tau_1, \tau_2)$. This function is the pillar of our teleportation measurements, from which the teleportation fidelity and correlation coefficient can be extracted. For a control qubit with polarisation P, mapped onto the target qubit as polarisation $\sigma_x P$, the teleportation fidelity F_P and correlation coefficient C_P are given as

$$F_P = \frac{g^{(3)}_{\sigma_x P}}{g^{(3)}_{\sigma_x P} + g^{(3)}_{\sigma_x Q}}, \qquad C_P = \frac{g^{(3)}_{\sigma_x P} - g^{(3)}_{\sigma_x Q}}{g^{(3)}_{\sigma_x P} + g^{(3)}_{\sigma_x Q}} \tag{4.12}$$

With this setup, two implementations of the quantum relay were tested: teleportation of the qubits required for the BB84 protocol[1], discussed in Section 4.4, and a full characterisation of the relay as a quantum black box[2,3], as explored in Section 4.5.

4.4 BB84 Protocol

In 1984, some recent observations, such as the unsuitability of photons as a storage medium, but their suitability as a communication medium, lead to advances in the field of quantum cryptography. Particularly, Charles H. Bennet and Gilles Brassard formulated their now famous BB84 quantum coin tossing method of publicly sharing a secret key[1], secure against an eavesdropper with unlimited computing power[16].

In the scheme, Alice and Bob have agreed that single photons will be sent encoded in one of two complementary bases, for example the rectilinear polarisation basis ($H = 0$, $V = 1$) and the diagonal polarisation basis ($D = 0$, $A = 1$). Alice prepares a random sequence of bits a_i, describing the basis used to encode bit number i ($HV = 0$, $DA = 1$), and another random sequence b_i, that she transmits in the chosen basis a_i. She transmits all the b_i to Bob over a quantum channel, encoded in the polarisations of single photons, but retaining the a_i, and Bob randomly chooses the basis to measure each received b_i. Alice then transmits the sequence a_i over an authenticated classical channel, informing Bob of which basis he chose correctly, but not revealing anything about the content of the b_i. Bob now has a subset b_i' of b_i in which he chose the correct measurement basis, corresponding to 50 % of the bits on average, which represents a shared secret between Alice and Bob. Bob now broadcasts a subset of the b_i' over a classical channel, and if Alice's and Bob's readings agree within a given tolerance, they use the remaining secret bits as a one-time pad. If the readings correlate poorly, this means that an unexpected source of loss is present in the quantum channel, potentially an eavesdropper, so they discard the shared bits and start again.

The first characterisation of the telecom-wavelength quantum relay was to implement this BB84 protocol, albeit without random selections of the bit sequences. Alice sent control photons with H, V, D, and A polarisations, alternating every hour, and Bob measured in the corresponding HV or DA basis. The teleportation fidelity was then evaluated according to Equation (4.12). If the average teleportation fidelity of the four states exceeds 75 %, then the relay has surpassed the limit imposed by classical physics, and exceeding 80% would allow for the implementation of error correction algorithms for secure QKD[17].

4.4.1 Teleporting control states

As in Section 4.3, Alice sends a control state to Charlie, and Charlie sends one half of an entangled photon-pair to Bob. Charlie performs a projective Ψ^+ Bell State measurement on his two remaining photons, where coincident counts at detectors D1 and D2 herald the teleportation of Alice's state onto Bob's photon, which is measured at detector D3 or D4 of Bob's polarisation analyser. The resulting triple-photon coincidences are then mapped to the third order correlation function $g^{(3)}(\tau_1, \tau_2)$, allowing evaluation of the teleportation fidelity.

4.4.1.1 Teleporting eigenstates

The top half of Figure 4.5 shows both third order correlation functions for teleportation of an *H* control state, corresponding to the 'correct' measurement at Bob, $g^{(3)}_{HVV}$, and the 'incorrect' measurement, $g^{(3)}_{HVH}$. The plots of F_H confirm that the teleportation fidelity does indeed approach unity for delays $\tau_1 \simeq 0$ and $\tau_2 \geq 0$. Furthermore, the teleported state is above the 50 % limit of uncorrelated coincidences for nearly 4 ns, demonstrating the long biphoton lifetime. In the case of teleporting an *H* control photon, the τ_1 and τ_2 clocks will always be started by a biexciton, if we assume that the intensities of leaked laser photons and detector dark counts are negligible in comparison, which is reasonable. Ideally, the biexciton will not be re-excited and an entangled exciton photon will be measured at time $\tau_2 > 0$, and a laser photon will be measured at any time τ_1. This gives rise to the strong vertical stripe in the $g^{(3)}_{HVV}$ plot.

However, sometimes the biexciton will be re-excited, radiatively decay a second time, and decay to the ground state, such that there exists an uncorrelated XX photon and a subsequent entangled XX-X photon-pair. Note that the biexciton emission is characteristically anti-bunched, such that there is a diminished probability of seeing two XX photons at τ_1 delays close to zero. One possibility in this situation is that the correlated XX photon will go to detector D1, the X photon will reach detector D3 at time $\tau_2 > 0$, and the uncorrelated XX photon will reach detector D2 at time $\tau_1 < 0$. This explains the enhancement in the three-photon coincidences seen in the $g^{(3)}_{HVV}$ plot at $\tau_1 < 0$ and $\tau_2 > 0$, away from $\tau_1 = 0$. The other possibility is that the uncorrelated XX photon will arrive at detector D1, upon which the correlated XX photon reaches detector D2 at time $\tau_1 > 0$, and the X photon reaches detector D4 at time $\tau_2 > \tau_1$. This is the cause of the enhanced coincidences seen in the $\tau_2 > \tau_1, \tau_1 > 0$ octant of the $g^{(3)}_{HVH}$ plot.

A similar but weaker contribution arises from a biexciton state decaying fully to the ground, and then being reexcited and radiatively decaying again. This results in an initial entangled XX-X photon pair, and a subsequent uncorrelated XX photon. In one case, the correlated XX photon triggers detector D1, the X photon reaches detector D3 at time $\tau_2 > 0$, and the uncorrelated XX photon reaches detector D2 at time $\tau_1 > 0$. This gives rise to the enhancement in $g^{(3)}_{HVV}$ at times $\tau_1 > 0$ and $\tau_2 > 0$. Alternatively, the uncorrelated XX photon will reach detector D1, the correlated XX photon will reach D2 at $\tau_1 < 0$, and the X photon will reach detector D4 at time $\tau_2 > \tau_1$. This is the cause of the weaker enhancement seen in the left-hand $\tau_2 > \tau_1, \tau_1 < 0$ octant of $g^{(3)}_{HVH}$. Higher-order reexcitation effects can be neglected, since these contributions decrease geometrically with the number of excitation photons involved. As such, the biggest contributions of undesired coincidences are due to reexcitation of the QD from the exciton or ground level to the biexciton level. These contributions, however, are all minimized along $\tau_1 = 0$.

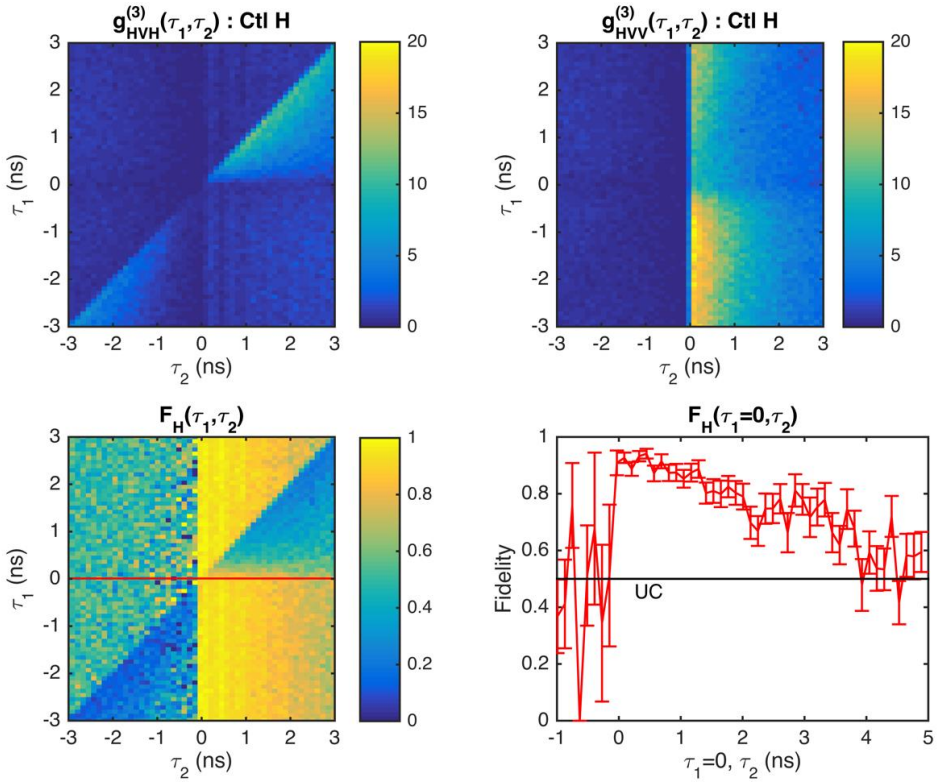

Figure 4.5: Teleportation of *H*-polarised laser photons onto *V*-polarised exciton photons, with time bins of size $\Delta\tau_1 \times \Delta\tau_2$ = 88 ps × 120 ps.

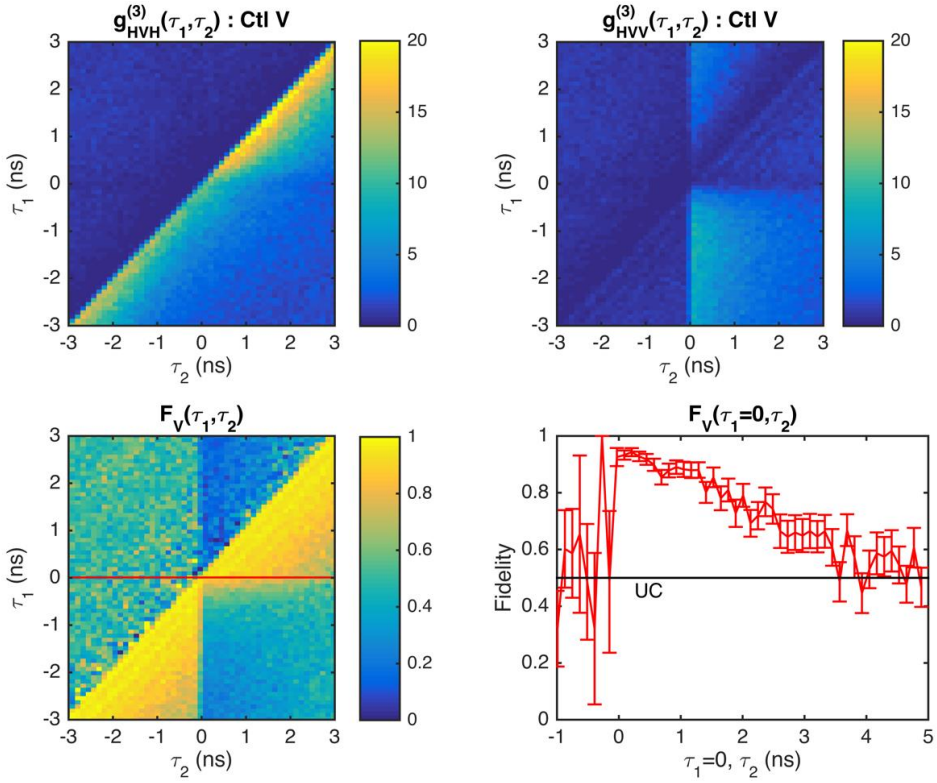

Figure 4.6: Teleportation of a *V* control state, nominally mapped onto *H*-polarised photons at Bob, with time bins of size $\Delta\tau_1 \times \Delta\tau_2$ = 88 ps × 120 ps.

Figure 4.6 shows the same set of plots as Figure 4.5, but for a teleported V control state. This time $g^{(3)}_{HVH}$ is the 'correct' measurement. In the absence of the undesired contributions, a V-polarised laser photon will reach detector D1, an H-polarised XX photon will reach D2 at any time τ_1, and an H-polarised X photon will reach Bob at time $\tau_2 \geq \tau_1$. The measurements in Figure 4.6 demonstrate the same high fidelity and long biphoton lifetime as in Figure 4.5, expected for teleportation of an eigenstate of the quantum dot. The exact same enhancements of the coincidences that occur in the two $g^{(3)}$ functions for a teleported H control state are present here, for the same reasons of reexcitation to the biexciton level. The degradation of the teleportation fidelity due to the coherence time of the XX photons is not present here, because in the case of teleporting eigenstates the laser and XX photons are completely distinguishable at the BSM. Also, degradation due to the FSS of the X level is not present, since the precession of the target state about the Bloch sphere yields only an unobservable global phase.

4.4.1.2 Teleporting superposition states

It is now that the coherence properties and FSS of the QD have an effect. Referring back to Equation (4.10), in the absence of TPI (take the limit $\tau_c \to 0$), the conditioned probability of Bob detecting a photon while observing in a superposition basis $|S\rangle = (|H\rangle + \exp(\mathrm{i}\phi)\,|V\rangle)/\sqrt{2}$ is the same for both of his detectors. Reintroducing the TPI, there is now an enhanced probability of Bob observing a photon at one of his detectors for delays $|\tau_1| \lesssim \tau_c$, in the temporal region where Alice's $|S\rangle$ control photons and Charlie's XX photons are indistinguishable. Additionally, the target state will accrue a relative phase $s(2\tau_2 - \tau_1)/2\hbar$ between the H and V polarisations. As discussed in Section 4.2.3, this gives rise to an oscillatory contribution in the correlation functions that will further degrade the teleportation correlation coefficients. However, utilising two complementary bases is necessary for the BB84 protocol, since in the trivial scenario of only one basis of qubits being sent, an eavesdropper Eve could implement a simple intercept-measure-resend scheme. Using the eigenbasis and a superposition basis minimizes the information that Eve could acquire from such a scheme, as well as making the eavesdropping detectable through diminished correlations. Adopting further privacy amplification schemes [116] would allow Alice and Bob to tolerate losses in the channel, and a certain level of eavesdropping.

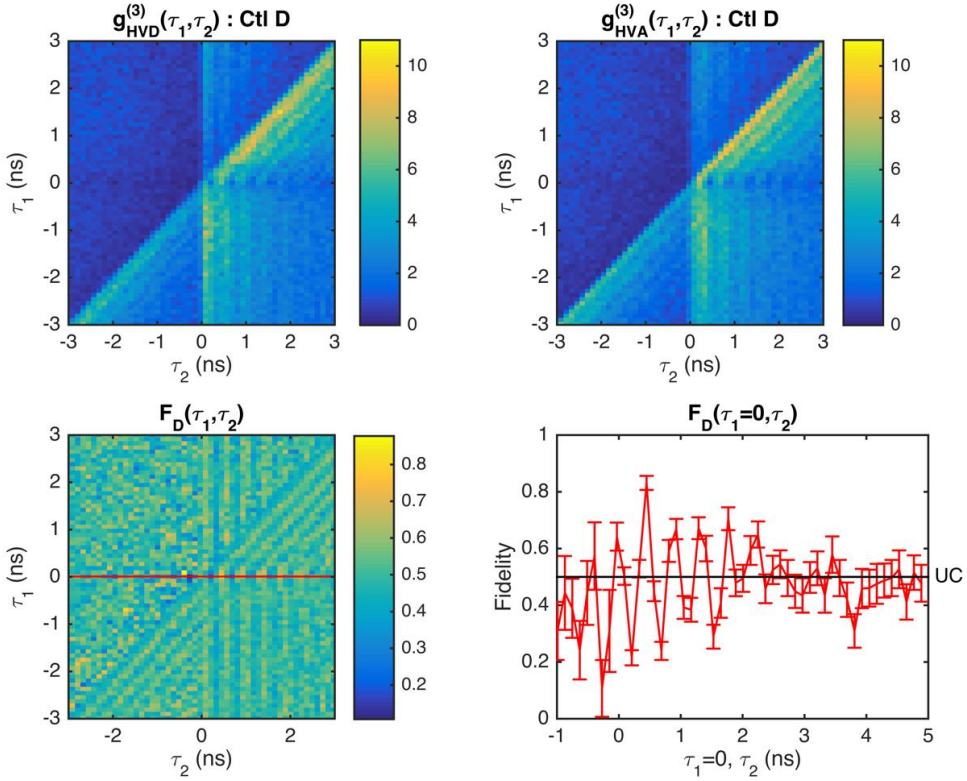

Figure 4.7: Teleportation of a *D* control state, nominally mapped onto a *D*-polarised photon at Bob, with time bins of size $\Delta\tau_1 \times \Delta\tau_2$ = 88 ps × 120 ps.

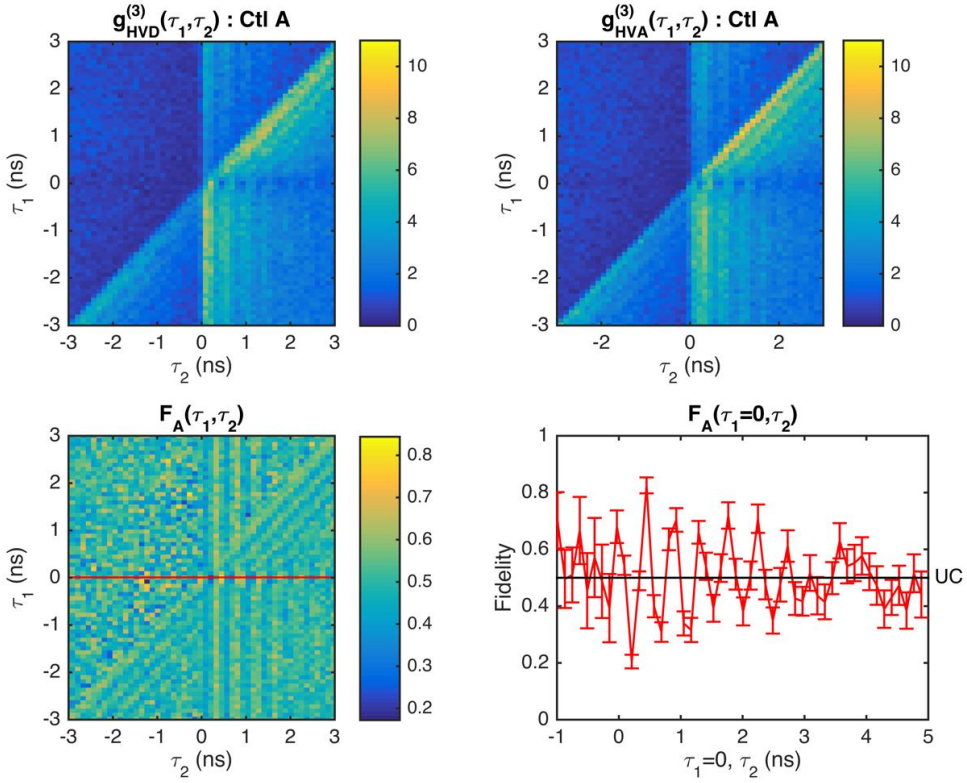

Figure 4.8: Teleportation of an *A* control state, nominally mapped onto an *A*-polarised photon at Bob, with time bins of size $\Delta\tau_1 \times \Delta\tau_2$ = 88 ps × 120 ps.

Figure 4.7 and Figure 4.8 show the teleportation correlation measurements for D and A teleported states, respectively. Note that, under the expected bit flip operation of the teleporter, these two diagonally-polarised states are mapped onto themselves. Now relying on the degree of XX/laser photon indistinguishability arriving at the Bell state analyser, the correlations are limited in the τ_1 delay on the order of the XX coherence time (95 ± 8 ps), as expected. The fine structure splitting also has a visible influence, causing the teleportation of the superposed target photon to oscillate in time. The result is an oscillatory stripe of the teleportation fidelity along $|\tau_1| \lesssim \tau_c$, with a period in the τ_2 delay of h/s. The oscillations in the teleportation fidelity are evident in the plots of $F(\tau_1 = 0, \tau_2)$. The fidelities are sufficiently high, given the high fidelity measured for the H and V teleported states, to be above the threshold of correlations explicable through classical mechanics. The teleportation fidelities for the diagonal states do not reach as high as the rectilinear teleported states, because the period of the oscillations (457 ± 0.5 ps in Section 3.5.2) and the XX coherence time are comparable to the 70 ps timing jitter of the detectors.

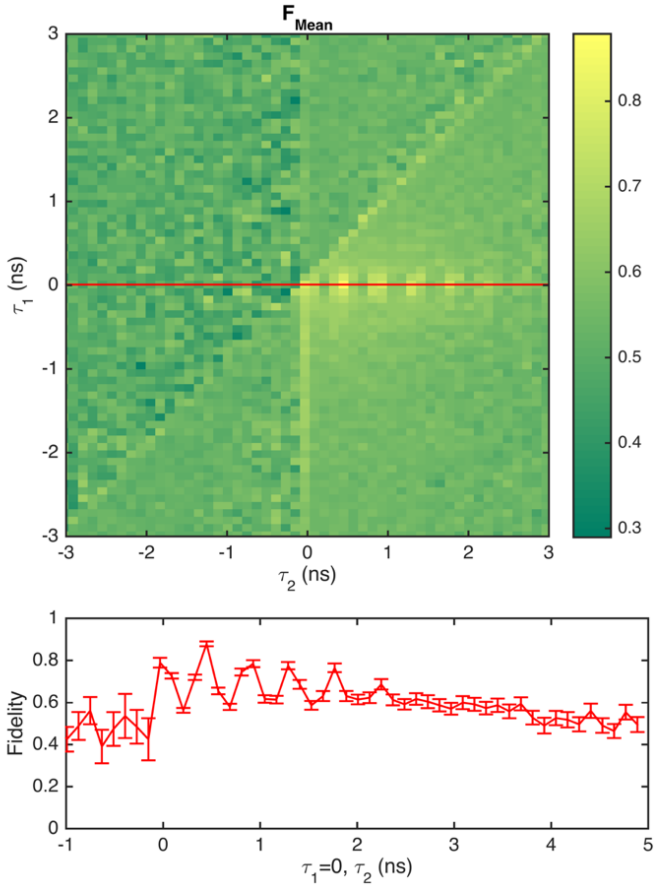

Figure 4.9: The mean fidelity across the four teleported states, H, V, D, and A, for time bins of size $\Delta\tau_1 \times \Delta\tau_2$ = 88 ps × 120 ps.

Additionally, there is a significant undesired background, in addition to the contributions discussed in Section 4.4.1.1, in the form of vertical and diagonal stripes. This was a result of a small misalignment in the reference polarisation used to calibrate the detectors D1 and D2, away from the poles of the Poincare sphere. This highlights the sensitivity of the teleportation experiment to the QD eigenbasis, and the importance of exhaustively calibrating the polarisation bases. Later in the quantum process tomography of Section 4.5, where mitigating the unwanted background was of even greater importance, the lessons learned here were used to significantly reduce this contribution.

4.4.1.3 Analysis

The mean fidelity for all four teleported state, *H*, *V*, *D*, and *A*, is shown in Figure 4.9. For two pairs of complimentary bases, the classical limit for the mean fidelity is 75 %. In a binning configuration of $\Delta\tau_1 \times \Delta\tau_2$ = 88 ps × 120 ps, this limit has been violated by eleven standard deviations. Thus, we have demonstrated, for the first time, quantum teleportation at telecommunication wavelengths with a sub-Poissonian photon-pair source.

Quantum teleportation has been demonstrated, but for use in a quantum communication channel, a teleportation fidelity above 80 % allows implementation of error correction algorithms, as well as being provably secure [17]. The magnitude and statistical significance of the teleportation fidelity can be investigated in post-processing of the data by considering triple coincidences in different sized temporal windows. The maximum size of the temporal post-selection window is limited by several physical mechanisms. In this case the dominating contributions are from the biexciton coherence time τ_c = 95 ± 8 ps along the τ_1 delay, and the exciton fine structure splitting s = 9.05 ± 0.01 μeV along the τ_2 delay. The estimated size of a useful temporal window will be on the order of $\Delta\tau_1 \times \Delta\tau_2 \simeq \tau_c \times 4h/s = 95$ ps × 114 ps. The lower limit on the size of the temporal windows is characterised by the detector timing jitter of 70 ps. Larger windows admit more photons, and thus provide more statistically significant results, while smaller windows increase the contrast in the observed damped oscillation and thus give a higher teleportation fidelity. The results of the mean fidelity vs time binning analysis are displayed in Figure 4.10. In the near-continuum of results, three sets of time-bin configurations are remarked upon, corresponding to three performance measures of teleportation:

(1) Maximum fidelity. The binning configuration for the highest average teleportation fidelity was a time window of $\Delta\tau_1 \times \Delta\tau_2$ = 64 ps × 24 ps. The mean fidelity here was 94.5 ± 2.2 % for 117 teleported photons, with individual fidelities of 91.3 ± 5.9 %, 97.0 ± 3.0 %, 92.9 ± 4.9 %, and 96.7 ± 3.3 %, for the control states *H*, *V*, *D*, and *A*, respectively.

(2) Most teleported photons. Keeping all individual fidelities above 75 %, a time window of size $\Delta\tau_1 \times \Delta\tau_2$ = 216 ps × 104 ps allowed for the teleportation of 1,817 photons. For this binning configuration, the mean fidelity was 82.8 ± 0.9 %, with individual fidelities of 89.7 ± 1.5 %, 90.5 ± 1.4 %, 76.0 ± 1.9 %, and 75.0 ± 2.0 %, for the control states *H*, *V*, *D*, and *A*, respectively.

(3) Highest quality teleportation. A quality factor was constructed as $(F_{Mean} - 0.75)/\sigma_{Mean}$, where σ_{Mean} is the measured uncertainty in the mean teleportation fidelity, describing how many standard deviations the fidelity is above the 75 % threshold. The binning configuration with the highest quality factor was found to be $\Delta\tau_1 \times \Delta\tau_2$ = 88 ps × 120 ps, closely matching the best expected window size. The mean fidelity here was 87.9 ± 1.1 % for 808 teleported photons, more than 11 standard deviations above the classical limit, with individual fidelities of 94.1 ± 1.7 %, 91.7 ± 1.9 %, 83.1 ± 2.5 %, and 82.5 ± 2.8 %, for the control states *H*, *V*, *D*, and *A*, respectively.

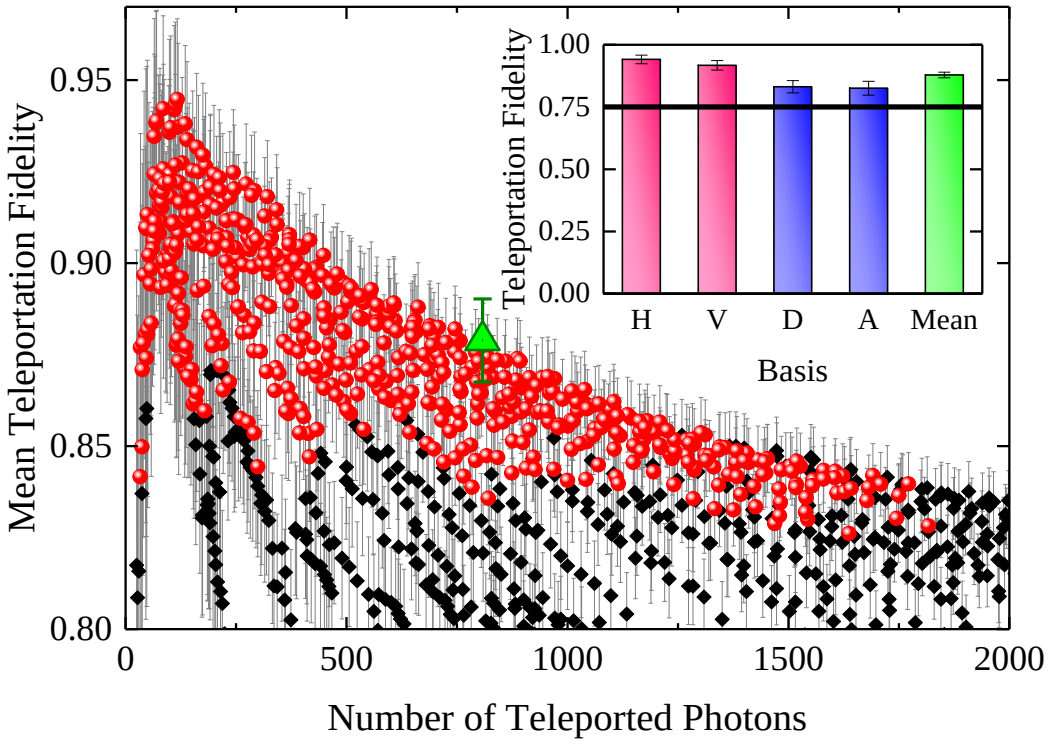

Figure 4.10: Variation of the mean teleportation fidelity for different configurations of time bins $\Delta\tau_1$ and $\Delta\tau_2$. Case (3) from Section 4.4.1.3, denoting the highest quality teleportation with a temporal window of $\Delta\tau_1 \times \Delta\tau_2$ = 88 ps × 120 ps, is displayed as the green triangle, and expanded upon in the inset bar plot. The red circles denote the results where every individual teleported state (*H*, *V*, *D*, and *A*) had a fidelity above 75%. The apparent stripes in the plot are the result of $\Delta\tau_1$ and $\Delta\tau_2$ being quantised to multiples of 8 ps. This data is also plotted in Huwer *et al.*[105].

There is a continuum of possible binning combinations, although in this experiment the bins were discretized in 8 ps steps due to computing power constraints. Figure 4.10 shows the near-continuous variation of binning configuration with observed teleportation fidelity, with case (3) from the analysis above highlighted as a green triangle and expanded in the inset bar plot. The red data points show all of the time binning windows where each of the individual teleportation fidelities exceeded 75 %.

To summarise, operating in the telecommunication O-band with a semiconductor QD entanglement source, two pairs of complementary states have been teleported, with a mean fidelity 11 standard deviations above the limit required to implement error correction algorithms.

4.4.2 Teleporting detuned control states

Discussed in Section 4.2.3, and evident in Equation (4.10), another important parameter determining the quality of teleportation is the spectral detuning between the laser and the average biexciton energy. The dynamics of the teleportation of superposition states has a crucial dependence on the XX-laser detuning. Coupled with the detector response, larger detunings are expected to degrade the teleportation fidelity more strongly, but it would be useful to characterise this change in a quantified manner.

As can be seen in Equation (4.10), there is no dependence on the teleportation of rectilinear control states with this detuning, since the photons in the BSM need not be indistinguishable for this special case. All other teleported states, however, do have a dependence on the detuning, and the strongest dependence is expected for balanced superposition states of the form $|S\rangle = (|H\rangle + \exp(\mathrm{i}\phi)\,|V\rangle)/\sqrt{2}$. Figure 4.11 shows the result of teleporting a superposition (D) control state for five different values of the laser/biexciton detuning, given in terms of the correlation coefficient C_D, and the dependence according to the semi-empirical model of the teleportation. The detuning is given in units of temporal frequency ν, as opposed to angular frequency $\omega = 2\pi\nu$ as we have been using, to make comparisons to telecommunication wavelength division multiplexing (WDM) schemes simpler.

The numerical model predicts a greater than 8 GHz range across which the correlations remain in the quantum regime, above 50 %. For reference, a typical telecom-wavelength light source has a spectral stability of approximately 1 GHz, and the bandwidth for the ultradense WDM scheme is 12.5 GHz. As such, with a degree of precision typically found in a modern higher-end optical data link, this quantum relay could be successfully operated within a present-day optical network infrastructure.

Notice that the maximal correlation does not occur at zero detuning, but instead at a slightly negative value. In fact, the maximally correlated teleportation events happen at a

detuning corresponding to half of the FSS, such that the laser is overlapped with one of the biexciton eigenstates, specifically the state being sent to detector D1 in Figure 4.4, triggering the experimental timers. This occurs because the two-photon interference effect is strongest for this detuning, given the arbitrary choice of triggering detector. This non-zero-detuning maximum has not been remarked upon in similar quantum relay experiments, since the spectral resolution of the biexciton/laser overlap is usually on the order of the fine structure splitting, about 2 μeV. However, the effect is apparent in numerical simulations behind a similar work on teleportation utilising a quantum dot[29], which dealt with an analogous experiment, save for operating at a lower wavelength (~885 nm) with a lower FSS (2.0 ± 0.1 μeV). In the desirable case of a zero FSS, the maximum correlation would occur at zero detuning.

The non-zero detuning correlation maximum occurs as a consequence of the method of data acquisition. Performing teleportation simulations considering different timing jitter between detector pairs D1-D2, and D1-D3/4, tells us that the effect arises due to timing jitter along the former, and is independent of the latter. Suspending knowledge of the XX/laser photon indistinguishability, the triple coincidences are most enhanced when the XX photons are spectrally overlapped with the laser photons, and when the XX photons trigger detector D1 (due to the finite detector response). The combined effect is that the overall highest correlation coefficient occurs for a detuning of $s/2h$.

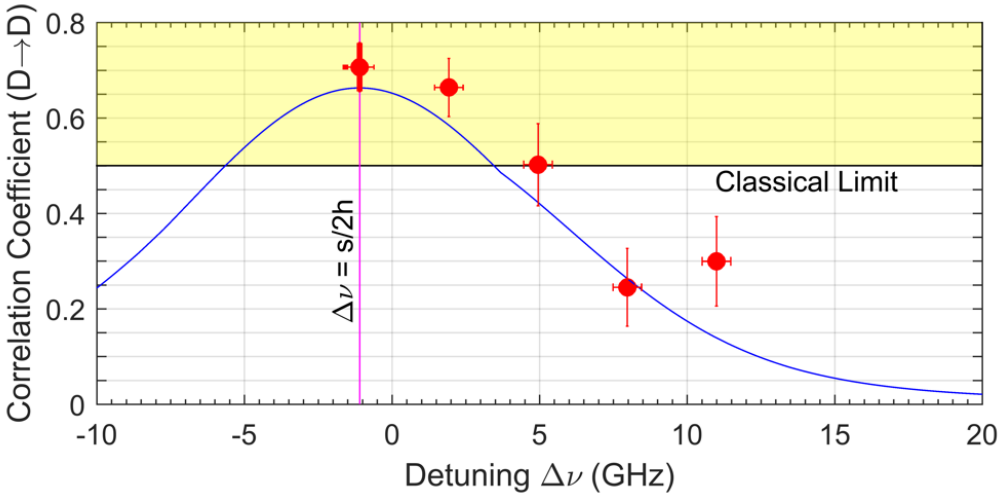

Figure 4.11: Comparison of experimental data with the semi-empirical model for teleportation of a superposition state (*D* in this case). This data is also plotted in Huwer *et al.*[105].

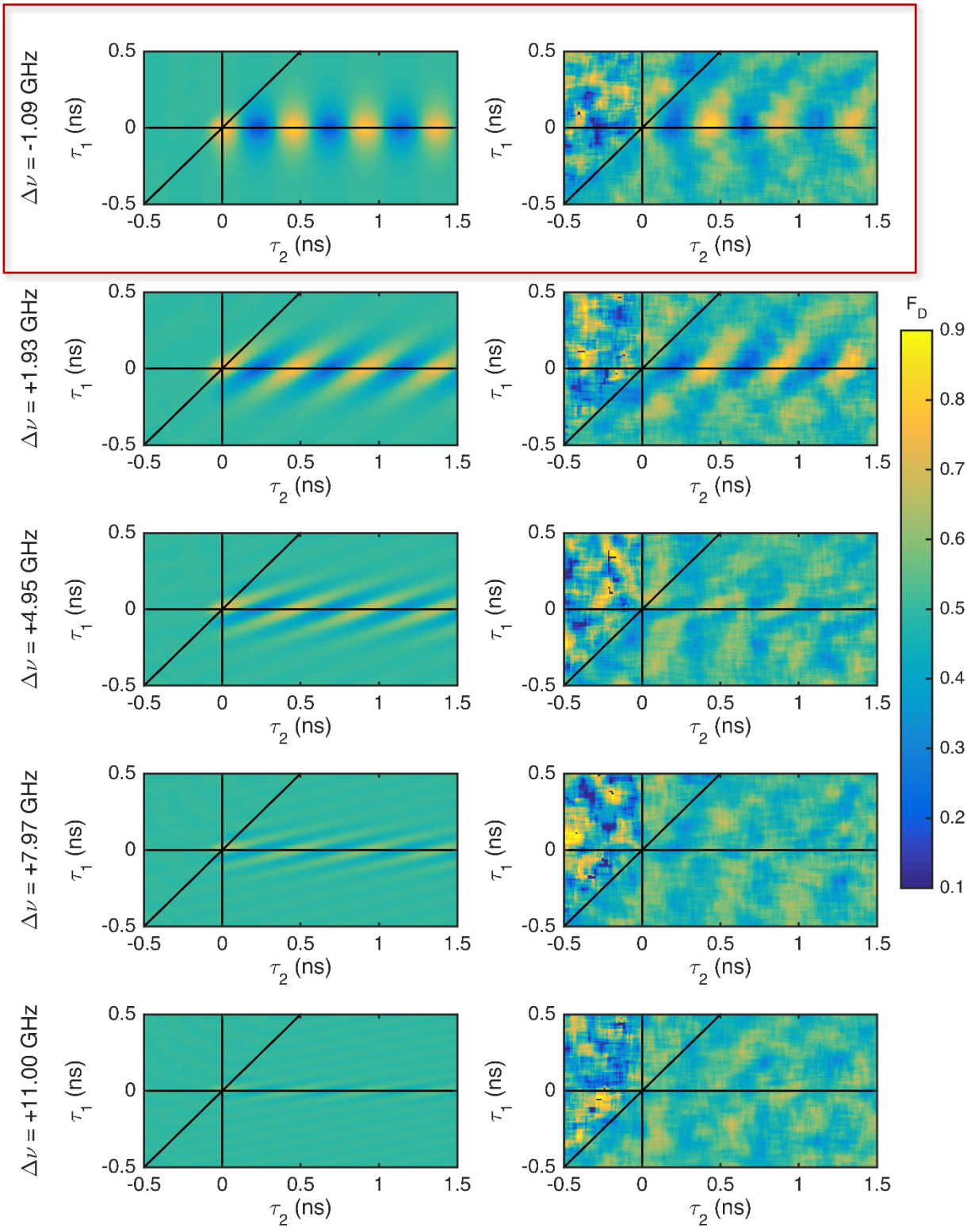

Figure 4.12: Experimental teleportation fidelities for a *D* control state, for different detunings between the laser and average biexciton energies. Each successive step corresponds to an extra 12.5 μeV of detuning. The top measurement in the red box was performed with the original BB84 measurement from Section 4.4.1, while the other four measurements were performed together in a single experimental cycle.

From Equation (4.10), we see a sinusoidal term in the teleportation probability, with a $\left(\Delta\omega - \frac{s}{2\hbar}\right)\tau_1$ dependence. With infinitely fast detectors, this term can be brought to zero by setting τ_1=0, and the curve in Figure 4.11 would be uniformly high. However, a finite time response 'blurs' the measured correlations along τ_1=0, so $\left(\Delta\omega - \frac{s}{2\hbar}\right)$ must simultaneously be set to zero to observe the strongest correlations. A lower timing jitter essentially allows smaller and smaller time intervals to be measured, which in turn increases the uncertainty in the photon energy, reducing the importance of spectral detuning. In the limit of arbitrarily small time bins, the spectral uncertainty is infinite, and the peak teleportation correlations will approach unity, no matter how large the detuning. Shown here, it is evident that the performance of this quantum relay can be guaranteed when using commercially available telecom-wavelength lasers.

4.5 Quantum Process Tomography

A rigorous test of the telecom-wavelength quantum relay is to measure the quantum process matrix via process tomography[2,3]. That is, by treating the relay as a quantum black box with single input and output qubits, it is possible to ascertain the mapping of an arbitrary control qubit to the resultant target qubit. Notably, the quantum process matrix can tell us both the process fidelity—to what level of reliability does the relay fulfil its task—and the teleportation fidelity for an arbitrary input state.

4.5.1 General prescription

The following treatment is summarised and interpreted from Chuang & Nielsen[2]. In a general quantum system, without limiting the input and output to single qubits, an input state ρ will be mapped onto an output state $\mathcal{E}(\rho)$, which can be expressed in the operator-sum representation as $\mathcal{E}(\rho) = \sum_i A_i \rho A_i^\dagger$. These A_i are normalised operators completely describing the evolution of the system. By deciding on a set of operators $\tilde{A}_i$ to form a basis for the operators on the state space in question, we arrive at the expression

$$\mathcal{E}(\rho) = \sum_{mn} \tilde{A}_m \rho \tilde{A}_n^\dagger \chi_{mn} \tag{4.13}$$

Here, we call χ the process matrix, which can be used to describe the output of our quantum black box for a general input state. Next, we choose a basis ρ_j to form a basis for the quantum state in our system. We can express the output state $\mathcal{E}(\rho_j)$ for an input ρ_j in terms of this basis, giving

$$\mathcal{E}(\rho_j) = \sum_k \lambda_{jk} \rho_k \tag{4.14}$$

The coefficients λ_{jk} can be evaluated as $\sum_s \mathrm{Tr}(\mathcal{E}(\rho_j)\rho_s)[\mathrm{Tr}(\rho_s \rho_k)]^{-1}$. The $\tilde{A}_i$ can also be expressed in terms of the basis ρ_i:

$$\tilde{A}_m \rho_j \tilde{A}_n^\dagger = \sum_k \beta_{jk}^{mn} \rho_k \tag{4.15}$$

The coefficients here can be determined as $\beta_{jk}^{mn} = \sum_s \mathrm{Tr}(\tilde{A}_m \rho_j \tilde{A}_n^\dagger \rho_s)[\mathrm{Tr}(\rho_s \rho_k)]^{-1}$, similarly. By letting κ be the inverse of the matrix β, we can then express the process matrix as

$$\chi_{mn} = \sum_{jk} \kappa_{jk}^{mn} \lambda_{jk} \tag{4.16}$$

By ascertaining the process matrix, we can evaluate the expected output state for an arbitrary input state, taking into account systematic imperfections of the teleporter.

4.5.2 Basis choices

For a single qubit, one requires four linearly independent input states and measurement operators to extract the process matrix; three states to probe the state space, and a further state for normalisation purposes. The input and measurement bases were chosen to correspond to calibrated laboratory conditions. The choices for the $\tilde{A}_j$ operators and ρ_j matrices were:

$$\tilde{A}_j = \{\mathbb{I}, \sigma_x, \sigma_y, \sigma_z\}$$
$$\rho_j = \left\{\begin{pmatrix}1 & 0\\ 0 & 0\end{pmatrix}, \begin{pmatrix}0 & 0\\ 0 & 1\end{pmatrix}, \frac{1}{2}\begin{pmatrix}1 & 1\\ 1 & 1\end{pmatrix}, \frac{1}{2}\begin{pmatrix}1 & -\mathrm{i}\\ \mathrm{i} & 1\end{pmatrix}\right\} = \frac{1}{2}\{\mathbb{I}+\sigma_z, \mathbb{I}-\sigma_z, \mathbb{I}+\sigma_x, \mathbb{I}+\sigma_y\} \quad (4.17)$$

The $\tilde{A}_j$ operators correspond to, respectively, the qubit undergoing no transformation, a bit flip, a simultaneous bit flip and phase flip, or just a phase flip. The ρ_j matrices are the density matrices associated with inputs of $H, V, D = (H+V)/\sqrt{2}$, and $R = (H - \mathrm{i}V)/\sqrt{2}$.

4.5.3 Quantum state tomography

Evaluating the process matrix for a single qubit requires state tomography[117] of four input and output qubits. In terms of the formalism of Section 4.5.1 and with the basis choices in Equation (4.17), the density matrices $\mathcal{E}(\rho_H)$, $\mathcal{E}(\rho_D)$, $\mathcal{E}(\rho_R)$, and $\mathcal{E}(\rho_V)$ are measured. In order to fully measure each resultant state $\mathcal{E}(\rho_i)$, identically prepared input states would need to be probed in three sets of linearly independent bases, usually chosen as the rectilinear, diagonal, and circular polarisations. However, since we have a time-evolving entanglement resource with FSS s, it is possible to observe in the diagonal measurement basis, wait a time $h/2s$, and then consider the measurement basis to now be circular. This is akin to having a static entanglement resource and a rotating reference frame. Taking this into account, the number of measurements required are reduced by 1/3, and Bob need only measure each of the four $\mathcal{E}(\rho_i)$ in the rectilinear and diagonal bases.

The HV projections of Figure 4.13 (H) and Figure 4.14 (V), and the DA projection of Figure 4.15 (D), resemble three of the four teleportation measurements of Section 4.4.1, except that now the correlation coefficient is being considered, rather than the teleportation fidelity (Equation (4.12)). The uncorrelated background contributions are the same as those discussed in Section 4.4.1. The correlations in Figure 4.16, however, demonstrate teleportation of an R-polarised control state. This gives a result similar to the D-polarised case, save for a $\pi/2$ shift in the oscillations along the τ_2 delay.

The DA projections of Figure 4.13 and Figure 4.14 demonstrate near-zero correlation coefficients, as hoped. There are some residual vertical and diagonal stripes however, similar to those observed in Figure 4.7 and Figure 4.8, but they have greatly reduced in amplitude thanks to improved polarisation calibration. The HV projections of Figure 4.15 and Figure 4.16 also show near-zero correlation coefficients in the vicinity of $|\tau_1| \lesssim \tau_c$, though this is less obvious when

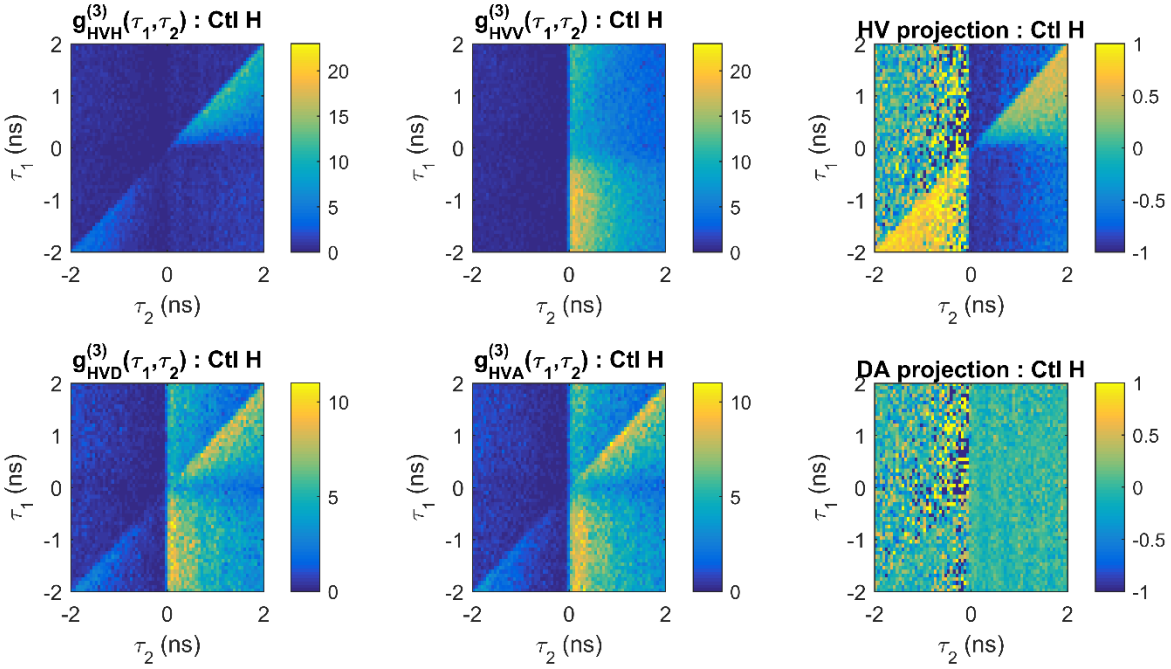

Figure 4.13: Correlation measurements for teleportation of an input H qubit. The top (bottom) row shows the rectilinear (diagonal) measurements, with the rightmost column showing the correlation coefficient extracted from the left pair of third-order cross-correlations. As expected, the HV projection is strongly anticorrelated with the input along $\tau_1 = 0$, and the DA projection is flat everywhere, except for noise at $\tau_1 < 0$ and a weakly correlated background at $\tau_1 \geq 0$. The time bins here are overlapping, with size $\Delta\tau_1 \times \Delta\tau_2 = 72$ ps $\times$ 56 ps, at 8 ps spacings.

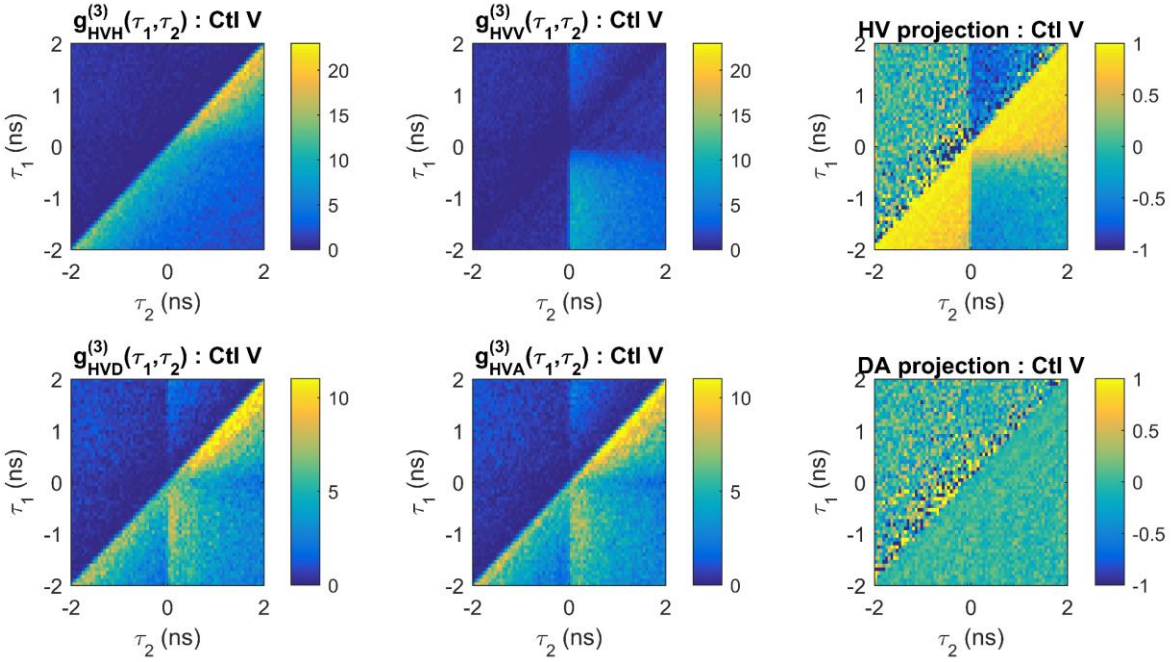

Figure 4.14: Correlation measurements for teleportation of an input V qubit. This time, the HV projection shows a strong positive correlation with the input, and we see a mostly flat DA projection. Overlapping time bins, with size $\Delta\tau_1 \times \Delta\tau_2 = 72$ ps $\times$ 56 ps, at 8 ps spacings.

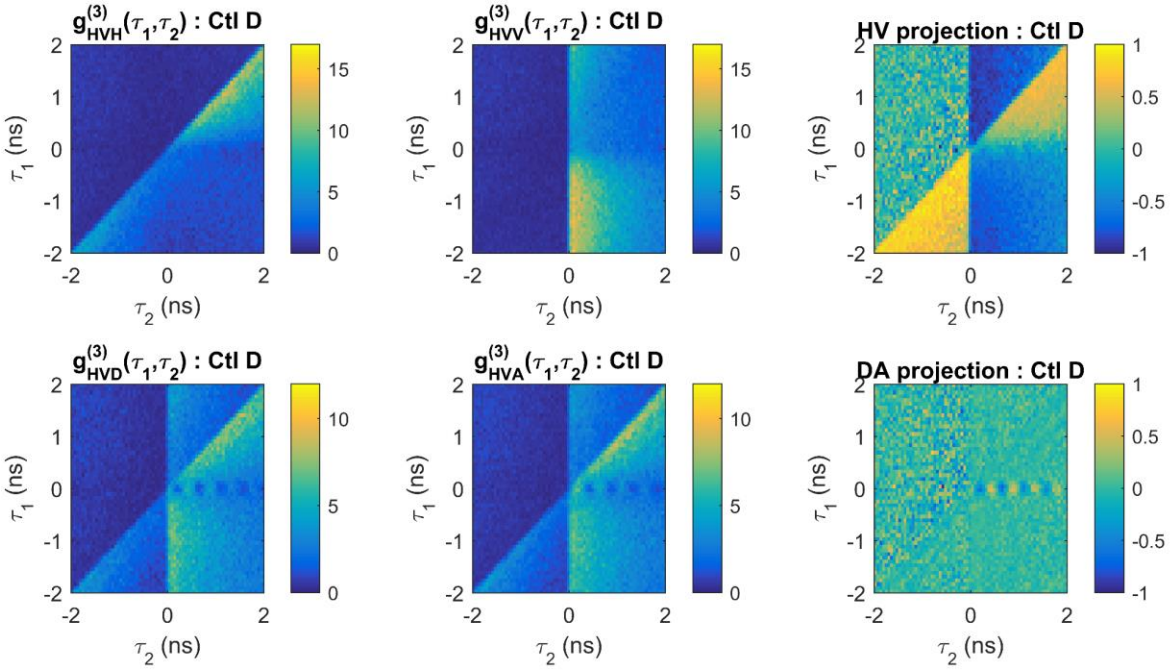

Figure 4.15: Correlation measurements for teleportation of an input D qubit. This time, the HV projection is close to zero at $\tau_1 \simeq 0$. The DA projection is flat away from $|\tau_1| \lesssim \tau_c$, but we see the characteristic oscillation of the correlation inside this region (and $\tau_1 > 0$), arising as a result of the time-evolving entanglement. Overlapping time bins, $\Delta\tau_1 \times \Delta\tau_2 = 72$ ps $\times$ 56 ps, 8 ps spacings.

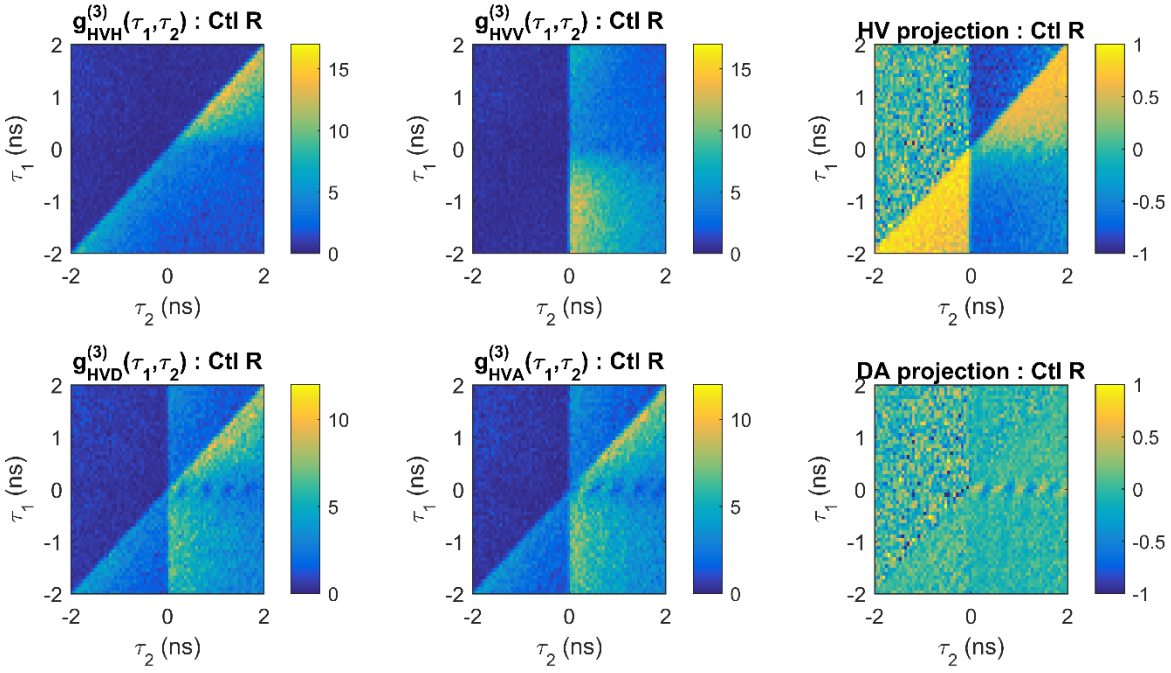

Figure 4.16: Correlation measurements for teleportation of an input R qubit. Again, as a superposition state, the HV projection is close to zero near $\tau_1 \simeq 0$. The diagonal correlations are nominally identical to the D control measurement in Figure 4.15, except that the oscillations have an additional $\pi/2$ phase along τ_2. Overlapping time bins, $\Delta\tau_1 \times \Delta\tau_2 = 72$ ps $\times$ 56 ps, 8 ps spacings.

observed by eye, due to the unbalanced unwanted triple coincidences in $g^{(3)}_{HVV}$ and $g^{(3)}_{HVH}$ giving non-zero correlation coefficients away from this region.

Plots A and B of Figure 4.17 show a comparison between the experimental data and the semi-empirical model, respectively, for teleportation of a *D*-polarised control state, showing good qualitative agreement between the two. Plot C of Figure 4.17 demonstrates the method for extracting the off-diagonal elements of the target state density matrix for the control states *D* and *R*. A portion of the measured DA correlation coefficient corresponding to the first two periods of the observed oscillations was fitted to a simple sinusoidal fitting function, extracting an amplitude A_0 and a zero-offset t_0.

$$C_{DA}(\tau_1 = 0{,}0 \leq \tau_2 \lesssim 2h/s) \rightarrow A_0 \cos\left(\frac{s}{\hbar}(\tau_2 - t_0)\right) \tag{4.18}$$

Considering these time-evolving correlations at times zero and $h/4s$, the density matrices could be evaluated as:

$$\mathcal{E}(\rho_i) = \frac{1}{2}\left(\mathbb{I} + \bar{C}_{HV}\sigma_z + A_0 \cos\left(\frac{st_0}{\hbar}\right)\sigma_x + A_0 \sin\left(\frac{st_0}{\hbar}\right)\sigma_y\right) \tag{4.19}$$

where $\bar{C}_{HV}$ is the mean value of the HV-projection across the same range of the sinusoidal fitting, $\mathbb{I}$ is the identity operator, and σ_i are the Pauli matrices. $\bar{C}_{HV}$, A_0, and t_0 were unique for each of the four control states. The measured density matrices for the four control states (*H*, *V*, *D*, and *R*), are shown in Figure 4.18. These evaluations were performed with time bin windows of size $\Delta\tau_1 \times \Delta\tau_2 = 72\ \text{ps} \times 56\ \text{ps}$. From these sets of measurements, it was then possible to evaluate the quantum process matrix, according to the treatment in Section 4.5.1.

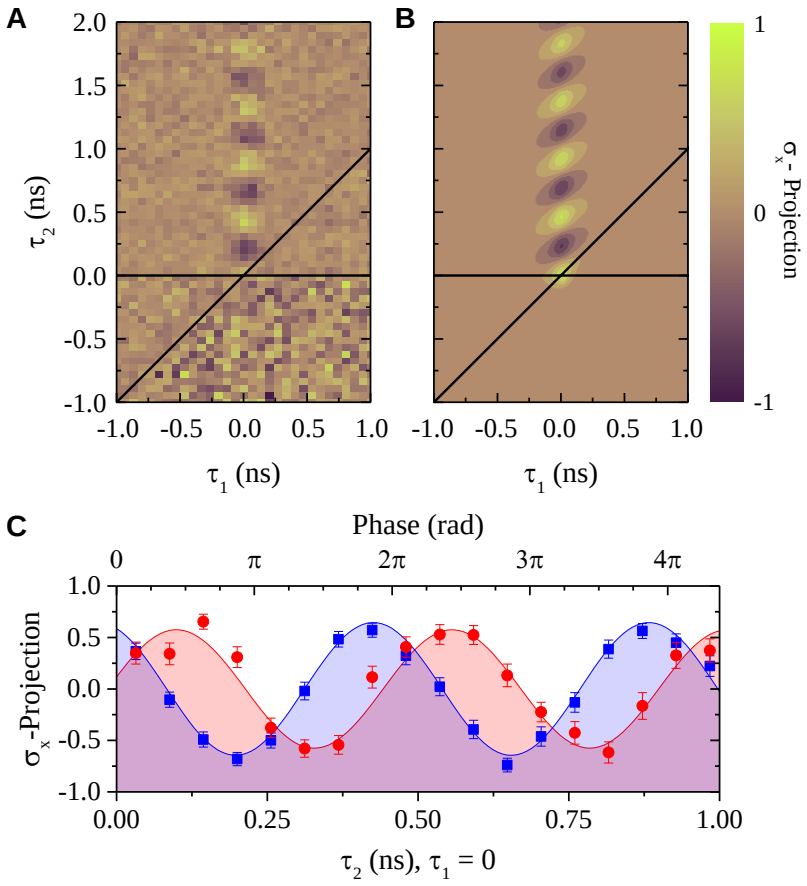

Figure 4.17: (Shown in Huwer *et al.*[105]) Extracting projected values for the σ_x and σ_y operator contributions to the target density matrix from the DA correlation coefficients. The time bins of the experimental data have size $\Delta\tau_1 \times \Delta\tau_2 = 72$ ps $\times$ 56 ps. Plot A shows the DA-projection for the teleported *D* control state, and plot B shows the corresponding semi-empirical model. Plot C demonstrates the evolution of the DA-projection along $\tau_1 = 0$ for the *D*- and *R*-polarised control states.

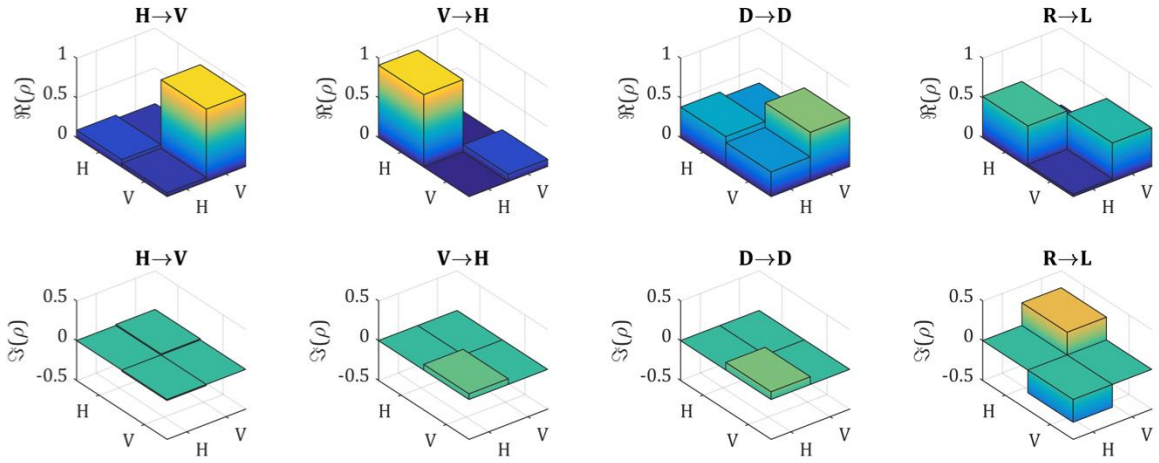

Figure 4.18: The density matrices for the four teleported control states, where the control state $|\psi_c\rangle$ is mapped as $|\psi_c\rangle \rightarrow \sigma_x|\psi_c\rangle$ under transmission through the quantum relay. The real and imaginary components are shown for the four measured density matrices.

4.5.4 The process matrix

From the density matrices measured in Section 4.5.3, and with the treatment of Section 4.5.1, it was possible to ascertain the process matrix χ for the telecom-wavelength quantum relay. The result of this calculation, as plotted in Figure 4.19, reveals a process fidelity of 75.4 ± 1.6 % to the expected bitflip operation, with a 15.5 ± 1.7 % chance of a simultaneous bitflip and phase flip, 6.0 ± 1.8 % chance of just a phase flip, and a 3.0 ± 1.7 % chance of no change in the quantum state. Uncertainties were calculated using a standard Monte-Carlo approach, incorporating the statistics of simulated sets of output states.

Having evaluated the process matrix, it is possible to calculate the expected teleportation fidelity for an arbitrary input state, by applying the formula

$$F(\theta,\phi) = \mathrm{Tr}\left(\rho(\theta,\phi)\sum_{j,k}\tilde{A}_j\rho(\theta,\phi)\tilde{A}_k\chi_{jk}\right) \tag{4.20}$$

where $\rho(\theta,\phi)$ is the density matrix for the control state $|\psi\rangle = \cos(\theta/2)\,|H\rangle + \mathrm{e}^{\mathrm{i}\phi}\sin(\theta/2)\,|V\rangle$, after undergoing the expected bitflip operation of the teleporter ($|\psi\rangle \rightarrow \sigma_x|\psi\rangle$), and $\tilde{A}_j$ are the operators chosen in Equation (4.17). This expected teleportation fidelity is plotted for the full range of θ and ϕ in Figure 4.20. Importantly, at no point does the predicted teleportation fidelity fall below 2/3, the average classical limit for an arbitrary input state.

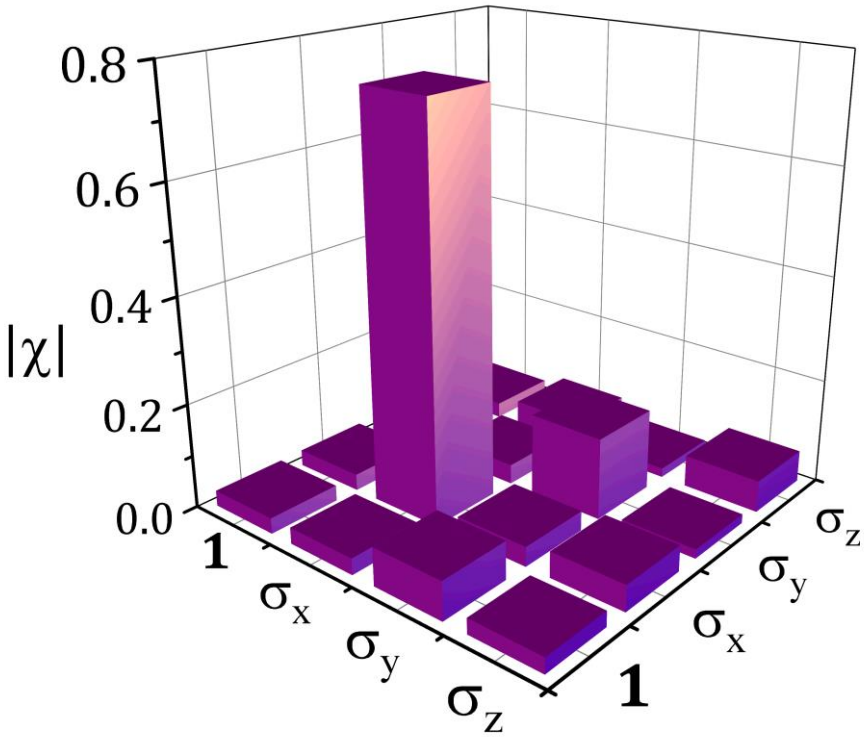

Figure 4.19: The process matrix extracted from the density matrices of Figure 4.18, also plotted in Huwer *et al.*[105].

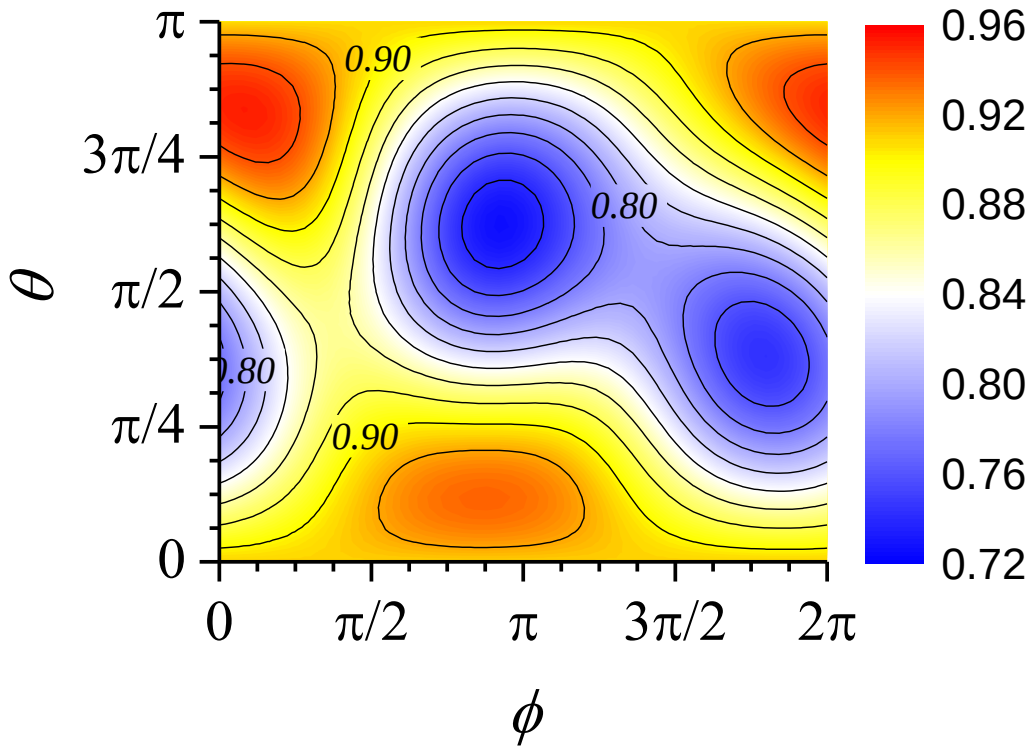

Figure 4.20: The expected fidelity of an output state as a function of its input, for arbitrary polarisations, also plotted in Huwer *et al.*[105]. This highlights that for no input state do we expect our teleportation to go below the 2/3 upper limit set by classical dynamics.

4.6 Conclusions

A semiconductor quantum dot source of telecom-wavelength entangled photon pairs has proven capable of operating as the central entanglement source in a quantum relay. To our best knowledge, this is the first implementation of a quantum relay with a sub-Poissonian entanglement resource operating in the telecom O-band (1260-1360 nm).

The quantum relay proved sufficient to operate the BB84 protocol[1], a simple and well-known implementation of quantum key distribution. *H*, *V*, *D*, and *A*-polarised photons were used as the control qubits in this experiment, and were teleported with fidelities convincingly above the threshold imposed by classical mechanics. The most statistically significant result yielded 808 teleported photons with an average teleportation fidelity of 87.9 ± 1.1 %, more than 11 standard deviations above the classical limit of 75 % for such scheme. It is also above the threshold required to ensure security on a quantum channel[17].

The process matrix, evaluated through quantum process tomography[2,3], was ascertained for the quantum relay. From this, a process fidelity of 75.4 ± 1.6 % was evaluated, and the teleportation fidelity remains above the average classical limit of 2/3 for an arbitrary input state, averaging 83.6 ± 1.1 %. This demonstrates the robustness of the quantum relay, allowing implementation for arbitrary QKD schemes of greater complexity than the BB84 protocol.

Having successfully implemented a quantum relay, the next step would be to take advantage of the low absorption in optical fibre at the operating wavelengths, and teleport qubits across metropolitan distances on the order of tens of kilometres. This will require development of sources whose light can be more efficiently collected, such as a QD embedded in a photonic crystal or a nanopillar microcavity, and sources with lower fine structure splitting and better coherence times. In the interest of making a more compact entanglement source, it would also be desirable to develop the source into an electrically-excited entangled-LED[46,47,118].

Quantum Dot Entangled-LED at 1.55 µm 5

5.1 Current state of the art

As an alternative to the InAs/GaAs quantum dots used in the experiments in Chapters 2 to 4, InAs QDs on a matrix of indium phosphide (InP) were being concurrently investigated as sources of coherent telecom-wavelength entangled photons. The initial results as described in this chapter (up to and including Section 5.5) have been summarised in Skiba-Szymanska *et al.*[104], and at the time of writing this thesis, a paper on the 1.55 µm InAs/InP entangled-LED experiment is being prepared.

Quantum dots of InAs/GaAs have been shown to exhibit single photon emission at wavelengths around 900-1300 nm[36,119], as well as the excitonic energy level structure that can lead to polarisation-entangled light[120], and can be doped into a diode structure and excited electrically[46,49,121]. Recently, such a QD source, namely an InAs/GaAs QD entangled-LED device emitting at 886 nm, was the basis of a 1 km quantum relay implementation[46]. More recently, as described in Chapter 4 of this thesis, an optically excited InAs/GaAs QD device was the entanglement source for an O-band telecom wavelength quantum relay.

However, it is impractical to extend InAs/GaAs dots to emit in the telecom C-band (1530 to 1565 nm), due to the strong confinement required to reduce the bandgap energy. A more promising material system involves growing InAs dots on an indium phosphide matrix. InAs/InP QDs have been shown to exhibit non-classical single photon statistics in the telecom O-band[122] and the coveted C-band[98,123]. They have also been experimentally observed to have exciton transitions at these wavelengths[124]. What more, InAs/InP QDs are theorized to have much lower exciton fine structure splittings than their GaAs counterparts[125], crucial for high-quality entanglement.

While using the same material to form the dots, it has been shown that using InP rather than GaAs as a matrix material significantly alters the electron and hole wavefunctions[126]. This leads to exciton emission wavelengths of about 1.55 µm in these dots, largely due to the smaller lattice mismatch, which is 3% for InAs/InP compared to 7% for InAs/GaAs[126]. We found that the growth shape of InAs QDs on (100) InP is dependent on the substrate doping, buffer layer chemical composition, and buffer morphology.

InAs/InP QDs are of particular interest for telecom laser implementations, since quantum dot lasers tend to have a lower threshold current, higher temperature stability, and higher material differential gain than quantum well lasers[127]. However, we are interested in configurations with lower dot densities, to look at single dots as sources of entangled telecom-wavelength photons, rather than as a well-performing gain medium. Dot densities on the order of 5 dots μm^{-2} have already been achieved[98], making single dot micro-photoluminescence practically achievable.

All of the work with InAs/InP dots presented in this chapter was performed with dots obtained by metalorganic vapour phase epitaxy (MOVPE) growth. The samples were grown by Dr Andrey Krysa (AK) at the National Centre for III-V Technologies at the University of Sheffield. Characterisation of the semiconductor wafers and processing of electrical devices were performed by Dr Joanna Skiba-Szymanska (JSS) and Dr Tina Müller (TM), both from the Toshiba Cambridge Research Lab. Modelling and design of optical cavities was carried out by Dr Jan Huwer (JH), also from the Toshiba Cambridge Research Lab. The author was a major contributer up to and including the work in Section 5.5, performing μPL characterisation of samples, measuring exciton fine structure splittings, and performing surements. The work in Section 5.6 was performed by JSS and TM, and the author assisted TM in preparing the entanglement experiment of Section 5.7.

5.2 Stranski-Krastanow InAs/InP QDs

The first attempt at InAs/InP QD growth resulted in rather high density dots, as can be seen in the micro-photoluminescence (µPL) spectrum and an AFM image in Figure 5.1, but natively emitting at the wavelengths of interest. Based on prior experience in InAs/GaAs QDs, it was believed that the fluorescence around 1100 nm is due to the QD wetting layer (WL), and that the dots were emitting between ~1200-1600 nm. Etching away the quantum dot layer revealed that the feature around 900 nm is fluorescence from the InP substrate.

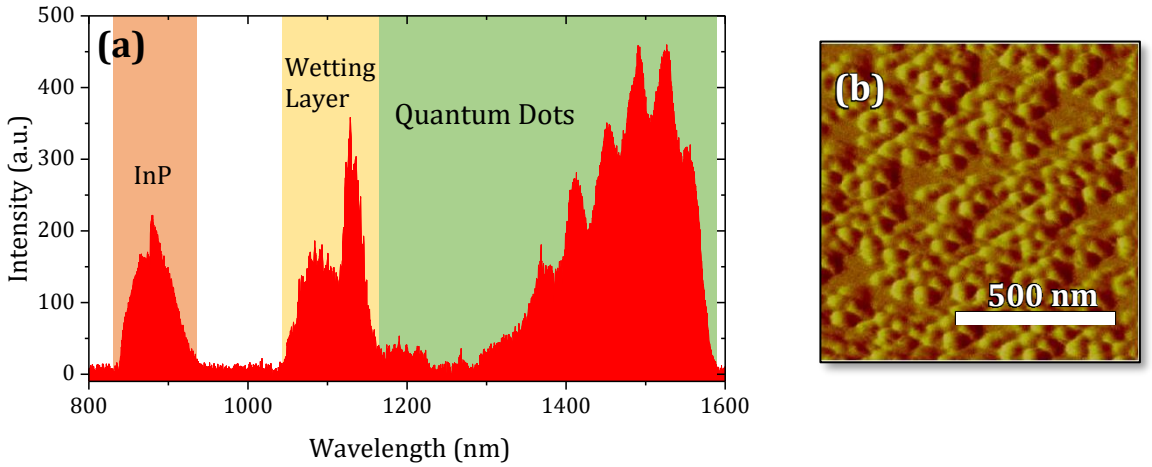

Figure 5.1: (a) A micro-photoluminescence spectrum of a sample from the initial growth run of Stranski-Krastanov InAs/InP quantum dots. (b) AFM scan performed by JSS confirming that the sample had a high density of quantum dots, at least several hundred per square micron, which was too high to isolate emission from single dots under micro-photoluminescence.

5.2.1 Growth optimization

The first challenge was to decrease the dot density, to an extent that individual dots could be resolved in µPL. It was discovered that, through controlling the amount of InAs deposited during the dot growth phase, densities as low as 1 dot µm^{-2} could be reached.

However, because the QDs were being grown in a horizontal flow reactor, and the wafers were not being rotated, significant non-uniformity in the dot number density was observed, varying between around 1 and 35 µm^{-2}, even under the optimised growth conditions, as exemplified in Figure 5.2. The non-uniformity is pronounced due to different group V elements in the substrate and QDs, making the QD growth surface very sensitive to the effects of the arsine/phosphine exchange reaction[128]. Although only about half of the wafer has tolerable densities ($\lesssim$ 10 dots µm^{-2}), the distribution is reproducible, suggesting that it is not due to a

systemic instability in the dot growth process. This has the benefit that pieces from similar locations on wafers from different growth runs are directly comparable.

The Stranski-Krastanov (S-K) QDs were grown at a temperature of 500 °C, growing 2 monolayers of InAs at 0.05 nm/s, by simultaneously exposing the surface to trimethylindium and arsine gas. The dots were then capped with 30 nm of InP, firstly at rates of 0.05 nm/s at 500 °C and then 0.43 nm/s at 640 °C. Some variables of the growth with which the dot properties could be controlled were the growth temperature, here ~500 °C, and the growth rate (by varying the vapour pressure), here ~0.05 nm/s. Through experimentation, these allowed some control over the characteristics, including the dot density and emission wavelength, and as will be seen later in this chapter, the exciton fine structure splitting.

Another important tuning knob to control the dot density was the quantity of material deposited in the dot formation stage. After several iterations of the growth recipe, dot densities sufficiently low (~10 μm^{-2}) to resolve single QDs through μPL were achieved. If not enough InAs was deposited during the dot growth stage, 4 Å thickness or less, the QD layer does not build up enough strain to bifurcate into the dot formation regime. Too much InAs, roughly 8 Å of material or more deposited, and the nice single μPL lines start to merge into a broad spectrum, due to too many dots forming. The optimal region appears to be a deposition of around 5.5 Å of InAs, where reasonable spectrally pure emission in both the O and C-bands is seen. Under SEM measurement, as seen in Figure 5.3, the dot density was visibly smaller and less clumped together at 5.5 Å compared to 8 Å, whereas with 4 Å of InAs (not pictured) no dots were observed.

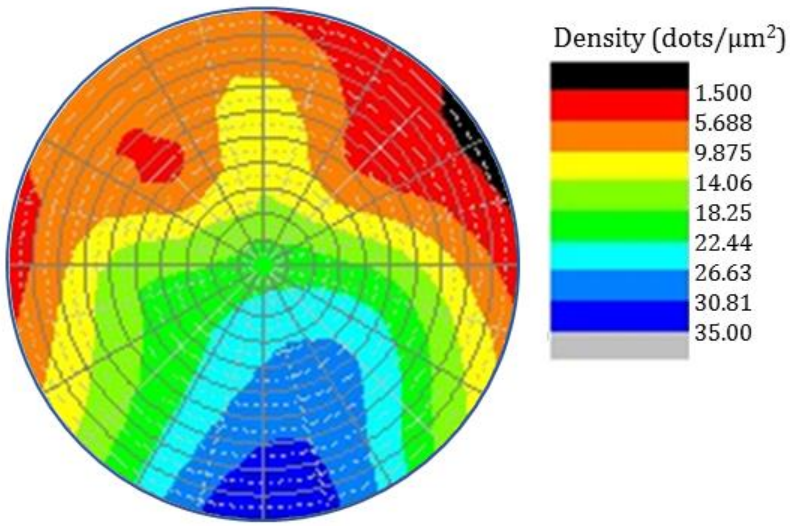

Figure 5.2: A density map of QDs across one of the optimized InAs/InP S-K QD wafers, measured by JSS, showing significant but largely tolerable changes in density, where around 1 QD μm^{-2} is ideal, but $\lesssim$ 10 QD μm^{-2} is usable.

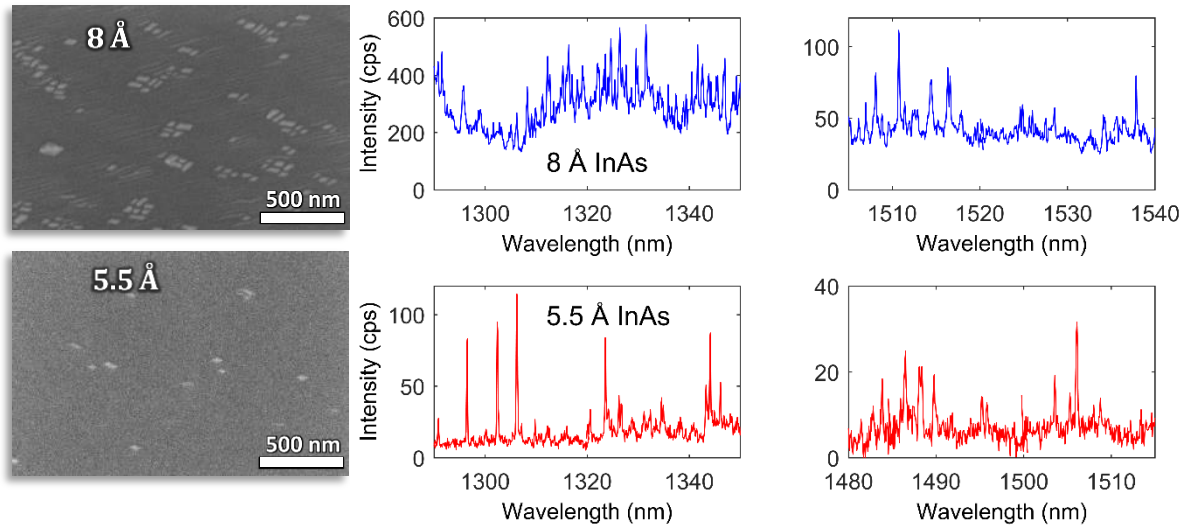

Figure 5.3: SEM scans (left images), measured by JSS, and µPL spectra, illustrating how dot density varies with the amount of InAs deposited. Too little (4 Å, not shown) material, and not enough strain has built up to cause the InAs layer to create any dots. Too much (8 Å), and too many dots form, such that it becomes difficult to resolve single spectral lines. The 'Goldilocks' region seems to be about 5.5 Å of InAs deposited, where enough strain has built up to form dots, but not enough to form too many, and spectral lines from individual dots are resolvable.

5.3 Droplet Epitaxy Quantum Dots

The exciton fine structure splitting (FSS), as discussed in Section 3.3, typically consists of an "intrinsic" contribution[125] from the zincblende structure of the semiconductor material, and external contributions arising from the shape and charge environment of the dot. Historically, S-K dots require a great deal of bandgap engineering or active control over some degree of freedom of the sample to reduce the FSS to acceptable levels. S-K growth relies on local strain to form dots, whereupon they will typically elongate along the [110] crystal axis of the substrate. The FSS was expected to be smaller here than if equivalent dots were grown at these wavelengths on GaAs[125], but minimum splittings of tens of μeV for S-K QDs were still anticipated. This would cause an entangled state to evolve in time too quickly to be useful, where a maximum of roughly 15 μeV can be tolerated with a detector timing jitter of 70 ps. Also, since it was hoped to develop more compact electrically-actuated devices, it was preferable not to rely on external electric fields to reduce the FSS.

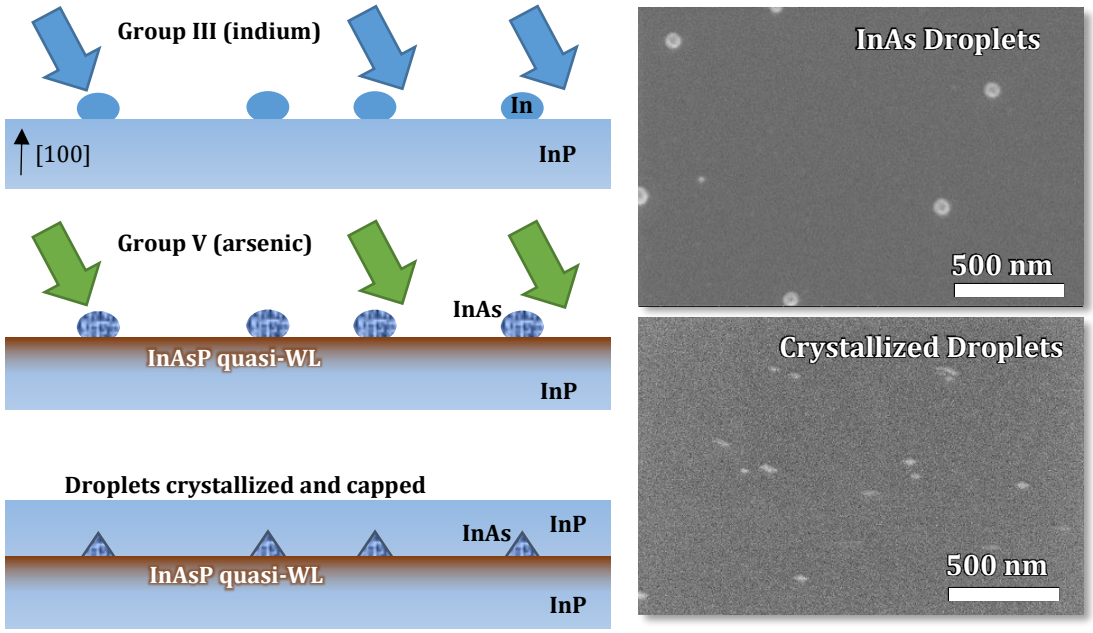

Figure 5.4: Illustrations of the of D-E growth mode of QD formation, with images measured by JSS, as shown in Skiba-Szymanska *et al.*[104]. A flux of indium is exposed to the InP substrate, forming droplets of indium metal. Arsenic is then exposed to the growth surface, seeding the metal droplets to form InAs droplets, but also interacting with the substrate interface to form a detrimental quasi-wetting layer of InAsP[128]. Finally, the droplets are crystallized into QDs and capped with 30 nm of InP. The top right image shows an SEM scan of InAs droplets prior to crystallization, demonstrating the high level of symmetry of each near-spherical droplet. Upon crystallization, in the bottom right image, the symmetry is lifted and the QDs are slightly elongated along a preferred axis. This effect is anticipated to be less pronounced for D-E QDs than for S-K QDs.

Keeping all this in mind, an alternate mode of QD growth known as droplet-epitaxy (D-E)[129] was investigated. These dots were formed by sputtering indium metal droplets onto the InP matrix, and seeding the droplets with arsenic, as shown in Figure 5.4. The sputtering was achieved by pyrolysis of trimethylindium at 400 °C, and the seeding step is achieved by introducing a flow of arsine gas at 400 °C, and building up the temperature of the substrate to 500 °C. The dots were then capped with 30 nm of InP[104].

Since these dots weren't being formed by strain propagation, but instead by seeding nearly spherical metal drops with a group V compound and crystallising, improved symmetry properties were observed, as seen in Figure 5.5. The S-K dots are visibly elongated along the [110] crystal axis, with a mean aspect ratio of 0.53. The D-E dots appear more circular, and have a mean aspect ratio of 0.91, closer to unity as hoped. From this, the D-E dots could be expected to be less influenced by an energetically favourable emission axis, reducing major contributions to the FSS, such that a value closer to the intrinsic FSS is seen.

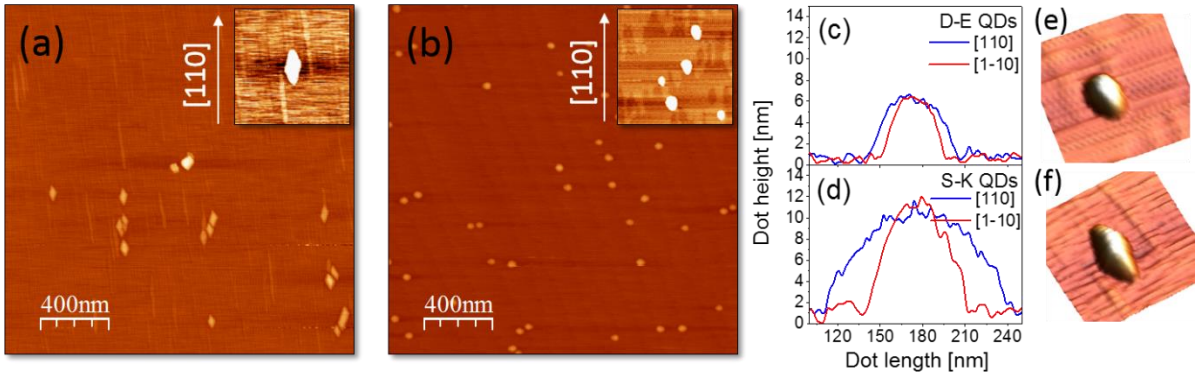

Figure 5.5: AFM scans of Stranski-Krastanov QDs (a,d,f) vs Droplet-Epitaxy QDs (b,c,e), taken from Skiba-Szymanska *et al.*[104]. Images (a) and (b) show 2 µm × 2 µm scans of the [100] plane, whereas (c) and (d) show the height of two dots along the [110] (blue) and [1-10] (red) crystal axes. There are also two zoomed-in images of single dots, qualitatively demonstrating the improved symmetry of D-E QDs (e) over S-K QDs (f).

5.3.1 Growth optimization

Again, the QD growth had to be optimized, taking what had been learnt about InAs/InP dot growth from the S-K growth experiments, to bring the dot density to a small enough level, and growing QDs with spectrally pure emissions. The annealing step was found to be a source of trouble, due of III-V intermixing in the InP matrix, leaving undesirable by-product on the wafer after the arsine flow/crystallization step, as exemplified in Figure 5.6. This figure also shows how increasing the arsine flow during the seeding step decreases the dot density. A possible explanation for this is that due to the As-P exchange interaction[128] there is a quasi-wetting layer made up of InAsP, similar to the S-K mode of dot growth, and that as more arsenic is deposited, it

becomes easier for the QDs to lose confinement and disappear into this layer, decreasing the overall dot density.

These dots represented the first observation of single C-band emission lines from our InAs/InP QDs, with single-line O-band emissions also present, though they are at least an order of magnitude too dim to verify the single-photon statistics in a sensible timeframe. μPL spectra corresponding to several values of attenuation of the excitation laser (in units of optical depth) are shown in Figure 5.6, demonstrating that the emission starts to saturate, and a broad background arises, before any usefully bright single lines appear.

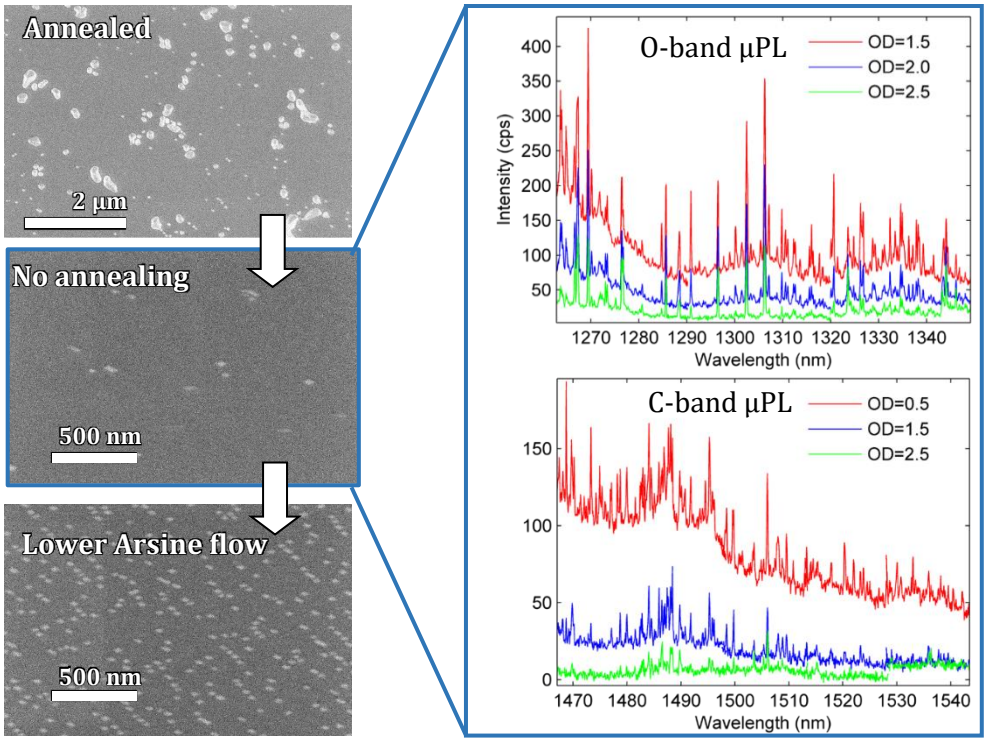

Figure 5.6: Demonstration of the annealing step and arsine flux on the dot quality and density. As seen in SEM scans performed by JSS, the annealing step leaves a tolerable density of QDs, but there is additional undesired by-product on the QD layer, leading to degraded spectral properties of the QDs and a broad background. Lowering the arsine flow increases the dot density.

5.4 Intra-cavity quantum dots

So far, InAs/InP QDs had been grown and measured to emit natively in both fibre telecommunication bands of interest. However, the photon intensities were too low to perform any of this thesis' earlier quantum optics experiments in a reasonable timeframe, and they were also low enough to make spectral characterisation problematic. A solution to this was to embed the dots in an optical cavity[130], enhancing the emission efficiency normal to the plane of the sample surface.

The microcavities were modelled by JH as alternating sections of two dielectric materials, independently considering the number of repeats in the top and bottom mirrors, the chosen materials, the size of the cavity, and the position of the dot layer within this cavity. From these models, it was possible to design weak planar cavities with an arbitrary central wavelength, with a bandwidth of about 50 nm. Growth recipes corresponding to the predicted models were then formulated by JH, JSS, and AK, and their performance confirmed with reflectometry measurements.

There were several choices to make in the cavity design, balancing quality with practicality. First and foremost was the material composition of the DBR mirrors. Alternating layers of InP and AlGaInAs were chosen, which gives an adequate refractive index contrast around wavelengths of 1.55 µm, and the materials were readily available in the growth system. Unfortunately, the AlGaInAs has a luminescence peak around 1250 nm, drowning out any QD light in the O-band. Since the C-band is the more useful wavelength window and remained unaffected, this material choice was tolerable. Initially, it was elected to only have a bottom reflector of 20 repeats of InP/AlGaInAs. The InP/vacuum interface itself acts as a mirror, enhancing the angle-dependant interference effects of the bottom DBR, creating a weak planar cavity, allowing the proportion of light sent to the collection optics to be significantly increased. It was decided to place the dots in a $3\lambda/4$ cavity, where the QD layer was 2/3 of the cavity length from the top plane of the sample, as shown in Figure 5.7. The result was an approximately ten-fold enhancement in the collection efficiency of the C-band light emitted by the InAs/InP QDs.

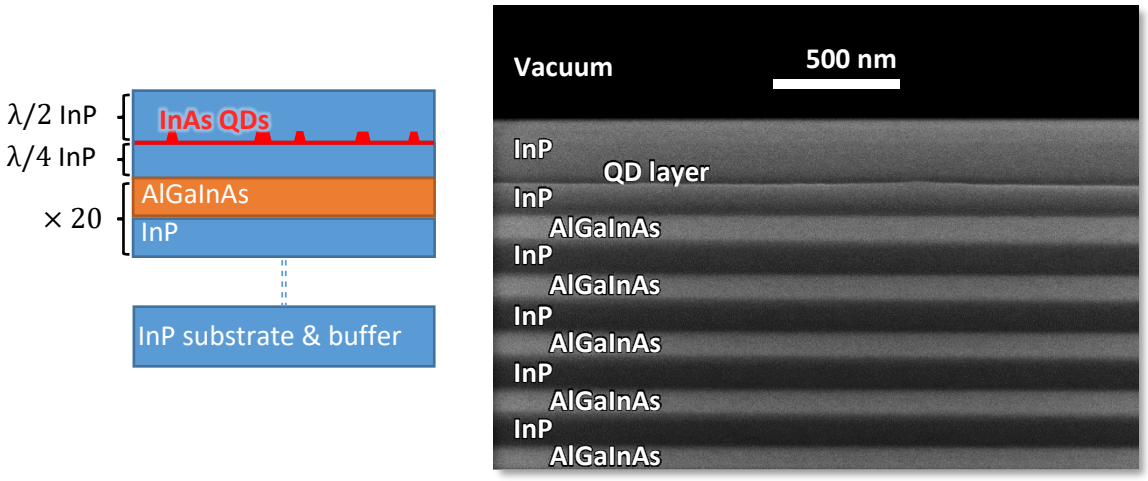

Figure 5.7: Representation of the weak optical cavities. Grown on the InP buffer are 20 repeats of 112 nm AlGaInAs and 123 nm InP layers, making up the bottom DBR mirror. The top mirror is made by the interface of the InP (n=3.1[131]) with the air/vacuum (n=1). The quantum dot layer is embedded two thirds of the way down in a 3λ/4 layer of InP.

5.4.1 Characterisation

With the increased collection efficiency, it was possible to perform some quantum optics experiments. Reflectometry measurements showed the cavities to be centred around wavelengths near 1520 nm, with a spectral width of 50 nm, with the precise central wavelength varying by ±50 nm depending on the location of the sample on the wafer. For the first time, the dots were bright enough to perform two-photon correlation measurements, such as required to measure second-order autocorrelation functions to determine the statistics of the source, and the polarisation cross-correlations required to observe entanglement.

Figure 5.8 shows a second-order autocorrelation function measurement of an S-K QD embedded in an optical cavity, optically excited by a 785 nm CW laser. The measurement used a pair of superconducting nanowire single-photon detectors (SNSPDs) with cross-channel timing jitter of 70 ps in a Hanbury Brown Twiss (HBT) configuration, achieving a $g^{(2)}(0)$ of 0.098 ± 0.037. The non-zero background comes primarily from detector dark counts, which had a combined photon rate of approximately 600 Hz compared to 11 kHz of QD light. This measurement provided the first evidence that the light was indeed coming from a single-photon source, and not some coincidentally spectrally narrow but classical source, such as weak lasing of a quantum well formed in the wetting layer of the dot growth plane.

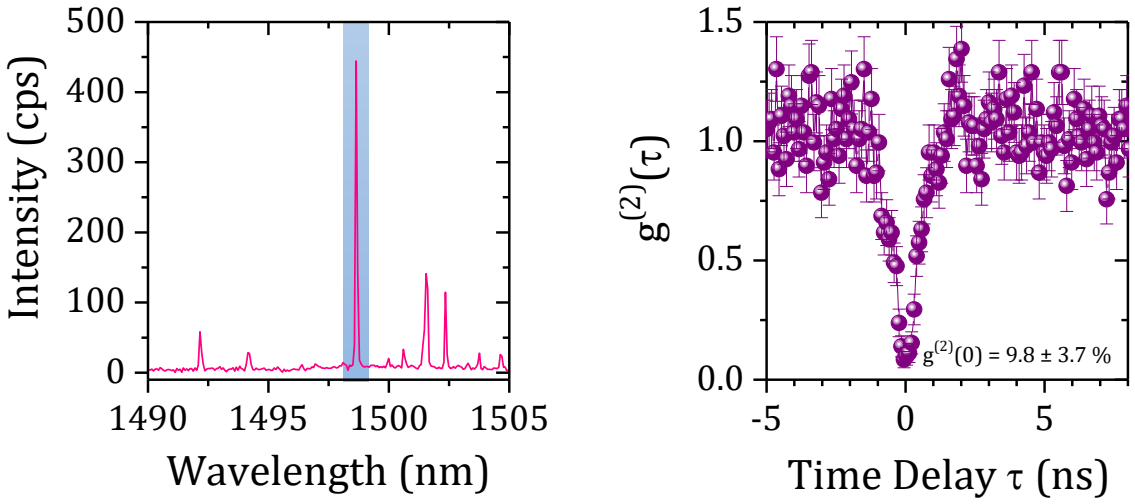

Figure 5.8: (a) µPL spectrum from an S-K InAs/InP QD embedded in an InP/AlGaInAs optical cavity. (b) Second-order autocorrelation measurement from the blue shaded excitonic emission in (a), demonstrating a distinctly sub-Poissonian characteristic.

5.5 Towards entanglement

At this point, InAs QDs had successfully been grown embedded in C-band-centred planar DBR microcavities, on an InP substrate, by two different growth modes. The dots demonstrate the characteristic excitonic energy level structure under μPL, such that biexciton and exciton transitions could be differentiated through optical power-dependence measurements. However, a picture of how the FSS varies across the S-K and D-E growth modes had not yet been built up, it has merely been postulated that the D-E dots would have lower splittings due to improved dot-shape symmetry.

Figure 5.9 shows a μPL spectrum, from a single D-E InAs/InP QD, where the neutral exciton (X) and biexciton (XX) lines have been ascertained via power-dependence measurement. With these lines identified, it was possible to use the quarter-wave plate method of FSS measurement as described in Section 3.3.1.

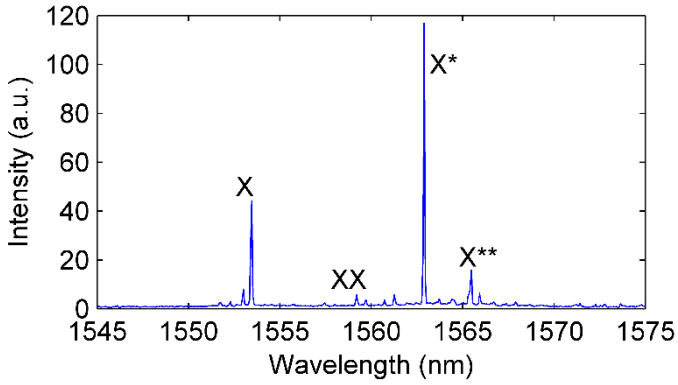

Figure 5.9: μPL from an InAs/InP cavity-embedded droplet-epitaxy quantum dot, showing exciton energy levels confirmed via excitation power-dependence measurements. Further characterisation of this QD is shown in Figure 5.10.

5.5.1 Fine structure splitting survey

In characterising the FSS statistics of the QDs, two nominally identical samples of InAs/InP QDs, save for their QD growth mode, were measured under optical excitation. One sample had dots grown by the S-K growth mode, and the other by the D-E growth mode, both with microcavities centred close to 1550 nm.

The QWP method was used to measure the FSS of 51 D-E dots and 36 S-K dots. Figure 5.10 shows some examples of the μPL spectra and FSS measurements for an S-K dot and a D-E dot that go into extracting an FSS value. The lower plots demonstrate how the spectra changing with the QWP angle, with the dot emission shifting between the two non-degenerate emission eigenstates per the dependence given in Equation (3.19). The FSS is sufficiently large in the S-K dot (Figure 5.10 (a)) that the eigenstates are spectrally resolvable (1 pixel = 60 μeV), so there are two distinct anti-correlated lines for both the X and XX. Here, the FSS was found by fitting Gaussian

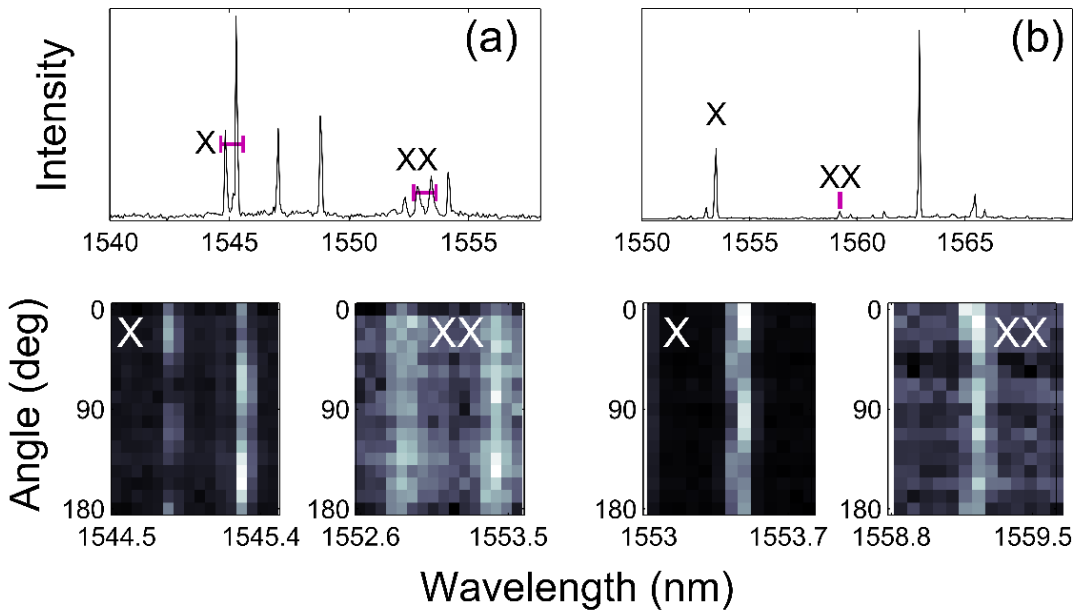

Figure 5.10: µPL spectra of two quantum dots, one grown via the S-K mode (a), with an FSS of 235 ± 3 µeV, and one in the D-E mode (b), with an FSS of 31 ± 1 µeV. This data is plotted in Skiba-Szymanska *et al.*[104].

curves to each of the X lines, and simply taking the FSS as the difference in energy. The shift in energy of the D-E QD (Figure 5.10 (b)) is below the resolution of the spectrometer, so the QWP dependence is seen as a 'wiggle' in the X and XX spectra. The FSS here was evaluated by performing Gaussian fits on each of the X spectra to find the central energies, and fitting to Equation (3.19), achieving uncertainties approximately 30 times better than the resolution of the spectrometer.

The two dots shown in Figure 5.10 are representative of the QDs measured. From 36 measurements, the splittings of the S-K dots are rather large, with a mean value of 176 ± 9 µeV, and a standard deviation of 58.8 µeV. The D-E dots, across 51 measured QDs, however, showed over a factor four decrease in FSS, with a mean value of 42 ± 2 µeV, and standard deviation of 17.7 µeV. This difference in FSS is statistically significant given the sample sizes (n>30). There is no clear dependence on the FSS with emission wavelength, as has been seen previously[132], shown in Figure 5.11. The difference in wavelengths of the two sets of QDs are not due to differences in the dots themselves, but slight variation of the optical cavity between the two samples. The FSS of the S-K dots are all too large to be able to observe XX-X entanglement experimentally, with the smallest splitting still several times larger than the 15 µeV upper limit. The smallest FSS from the D-E QDs was 12.0 ± 2.0 µeV, however, which means that the oscillations in the XX-X polarisation cross-correlations would be above the lower limit of temporal resolvability.

The limiting factor of such a measurement would now be the intensity of the QD light. Figure 5.10 (b) demonstrates the characteristic distribution of intensities of the excitonic

transitions, and it is clear that the XX is excited poorly, perhaps due to the above-band optical excitation in use being a poor means of injecting carriers into the XX level. This means that the correlations required to build up a convincing measurement of entanglement could not be performed in a sensible time frame. However, the sub-15 μeV FSS result is an important step forward in creating a C-band entangled photon-pair source.

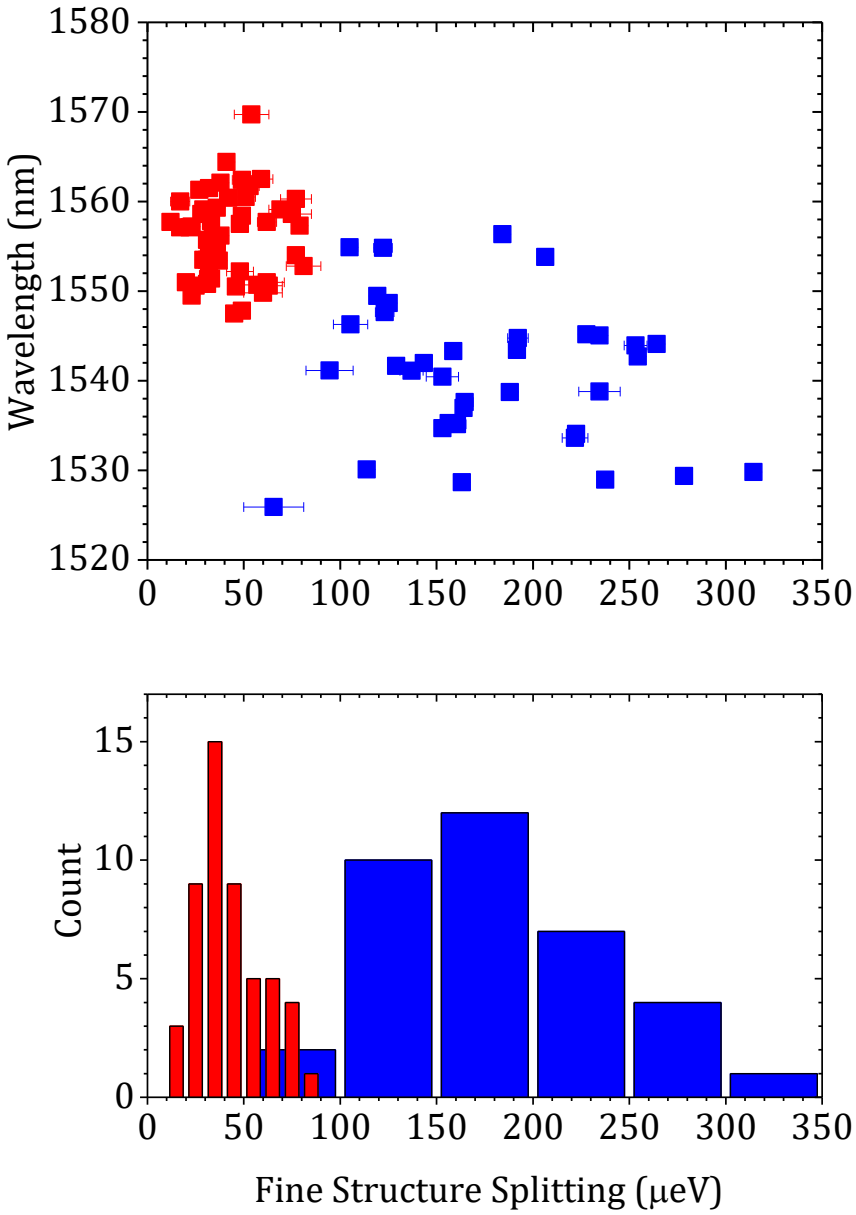

Figure 5.11: A sample of FSS measurements for 51 D-E QDs (red), and 36 S-K QDs (blue), as shown in Skiba-Szymanska *et al.*[104]. There is no strong correlation of wavelength with splitting in each grouping, as can be seen in the top plot. The mean FSS for the D-E dots is 42 ± 2 μeV, with a standard deviation of 17.7 μeV, while the mean for the S-K dots is over four times larger at 176 ± 9 μeV, with a standard deviation of 58.8 μeV.

5.6 Electrical excitation

At this point, optically-excited C-band QD light sources, ready to observe polarisation entanglement, had been achieved. However, it was hoped to replicate prior research on lower-wavelength entangled light emitting diodes (ELEDs)[29,37,46,47,49]. The proceeding work was performed by TM and JSS during the writing of this thesis.

Chapters 2 to 4 all utilised QDs embedded in *p-i-n* doped optical cavities, processed into electrical devices that would allow control over the fine structure splitting and coherence properties of the QD emission (Section 3.4.2). Until this point in the development of an InAs/InP quantum light source, however, doping the QD samples had been avoided. This was because we hoped to develop QDs that had a natively good FSS and spectral purity, not requiring tuning from an external field to improve performance, and then embed them in a diode structure such that the dots could be excited electrically.

The morphology of the QD contributing to a low FSS and the improved collection efficiency from an optical cavity could be expected to be directly transferrable between an optically excited and an electrically excited device[47,118]. However, the ability to inject holes and electrons into a QD to form excitons and biexcitons, have them recombine radiatively, and achieve the same degree of spectral purity would not be guaranteed between the two excitation schemes.

Figure 5.12 shows the design of the electrical device, as produced by JSS and TM. The dopants for the N-doped bottom layer and P-doped top layer were silicon and zinc, respectively. Early designs of the InAs/InP QD-based electrical devices saw problems of dopant segregation and diffusion[133,134] in the top-mirror, so it was decided to process the devices such that the electrical contacts were intra-cavity, primarily in contact with the doped InP. The optical cavity consisted of both top and bottom DBR mirrors, 20 repeats of undoped InP/AlGaInAs beneath the

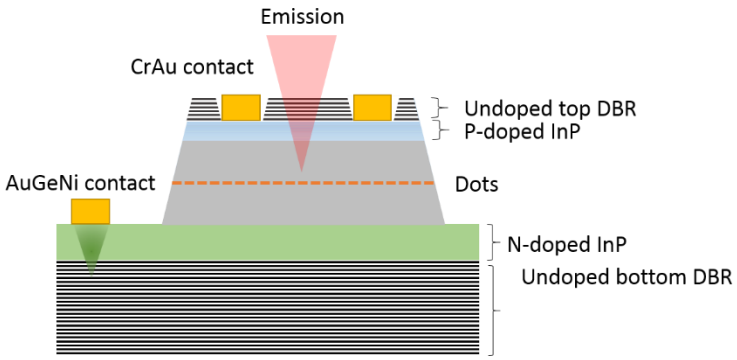

Figure 5.12: A general outline of the InAs/InP QD LED design. To mitigate the problem of Zn diffusion and segregation, most of the cavity was left undoped, and the device was processed to have intra-cavity electrical contacts. Various spacings of the QD layer were investigated, with the final design having the QD layer 3λ/4 above the bottom mirror in a 2λ cavity. placed at as large a distance from the top mirror as seemed practical.

QD layer, except for the top-most layer of N-doped InP, and three repeats of undoped InP/AlGaInAs above the QD layer, save for the bottom-most P-doped layer of InP. To further mitigate the problem of Zn diffusion, the cavity was made larger, with the dots placed at a height of 3λ/4 from the bottom mirror in the 2λ cavity. This distanced the QDs from the Zn-containing mirror, here at a remove of 5λ/4, more than double the λ/2 depth from the top mirror used in Section 5.4.

The improvements made in the LED design showed success, and a device made by JSS and TM made it possible to collect μEL from a single QD. Figure 5.13 shows the results of an autocorrelation measurement from such a dot, achieving a $g^{(2)}(0)$ value of 0.20 ± 0.04 for an excitonic transition emitting at 1597.5 nm. This result demonstrated the successful development a C-band single-photon LED.

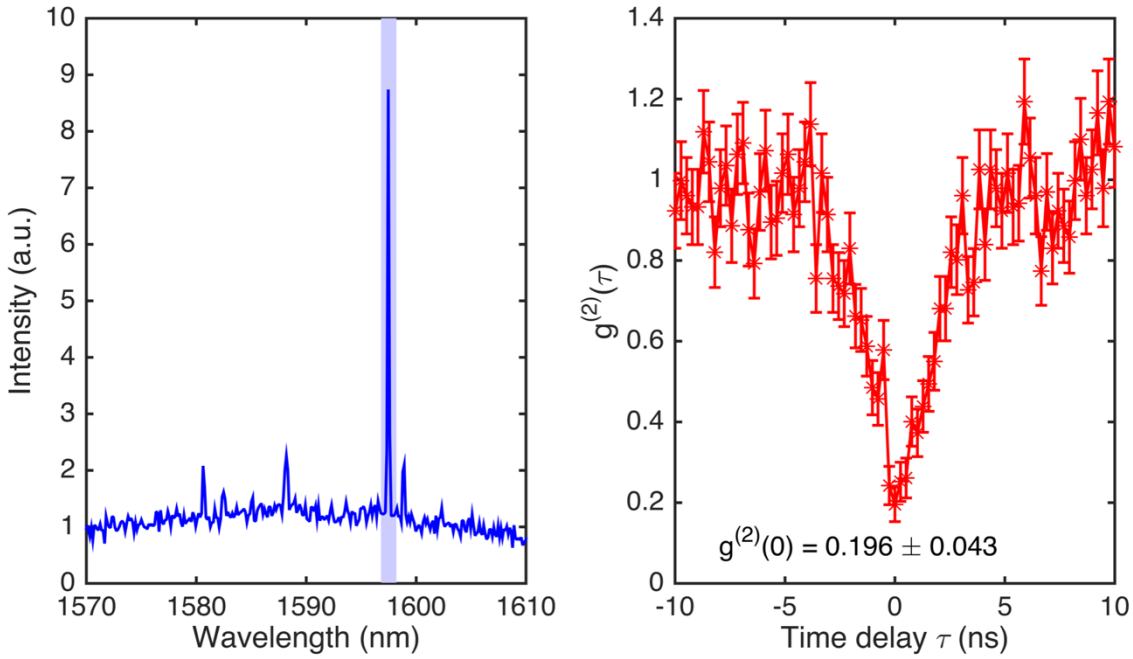

Figure 5.13: Micro-electroluminescence (μEL) in the telecom C-band from a single QD was achieved, shown in the left-hand plot. A second-order autocorrelation measurement was performed on the μEL in the shaded part of the spectrum, shown in the right-hand plot, demonstrating the single-photon nature of this electrically-excited C-band QD light source. The μEL spectrum and autocorrelation were both measured by TM.

5.7 Entanglement from an LED

In the climax of this chapter's work, JSS and TM had developed what was believed to be a QD entangled-LED (ELED), based on excitation-power dependence measurements and polarisation-correlated variation in the LED µPL spectra with QWP angle. To show that these QDs are sources of entangled photon pairs, polarisation-filtered cross-correlations between the exciton and biexciton photons were performed, exactly as performed in Chapter 3. The same treatment as performed in Section 3.2.3 of Chapter 3 was used, performing the cross-correlation measurements in the HV, DA, RL, $E_{RD}E_{LA}$, and $E_{RA}E_{LD}$ polarisation bases. From this, the fidelity $F(\phi)$ to a Bell-like state $|\Phi(\phi)\rangle = (|HH\rangle + \exp(i\phi)\,|VV\rangle)/\sqrt{2}$, and the Bell parameter $S_B(\phi)$, could be extracted. Repeating these expressions from Equations (3.11) and (3.12), these were evaluated from the correlation coefficients C_{AB} as:

$$F(\phi) = \frac{1}{4}\left(1 + C_{HV} + (C_{DA} - C_{LR})\cos\phi + \left(C_{E_{LD}E_{RA}} - C_{E_{LA}E_{RD}}\right)\sin\phi\right)$$

$$S_B(\phi) = \frac{1}{\sqrt{2}}\left[\left(C_{E_{LD}E_{RA}} - C_{E_{LA}E_{RD}}\right)\sin(\phi) + (C_{DA} - C_{LR})\cos(\phi) + 2C_{HV} + C_{DA} + C_{LR}\right]$$

In the case of the time-evolving two-photon state, ϕ is expressed as $s\tau/\hbar$ in the above two equations, while fidelity to the Φ^+ or Φ^- Bell state corresponds to $\phi = 0$ or π, respectively. Values of the fidelity above 50 % signify non-classical correlations, but the strongest known indicator of quantum entanglement is through violation of the CHSH inequality ($|S_B| \leq 2$)[27].

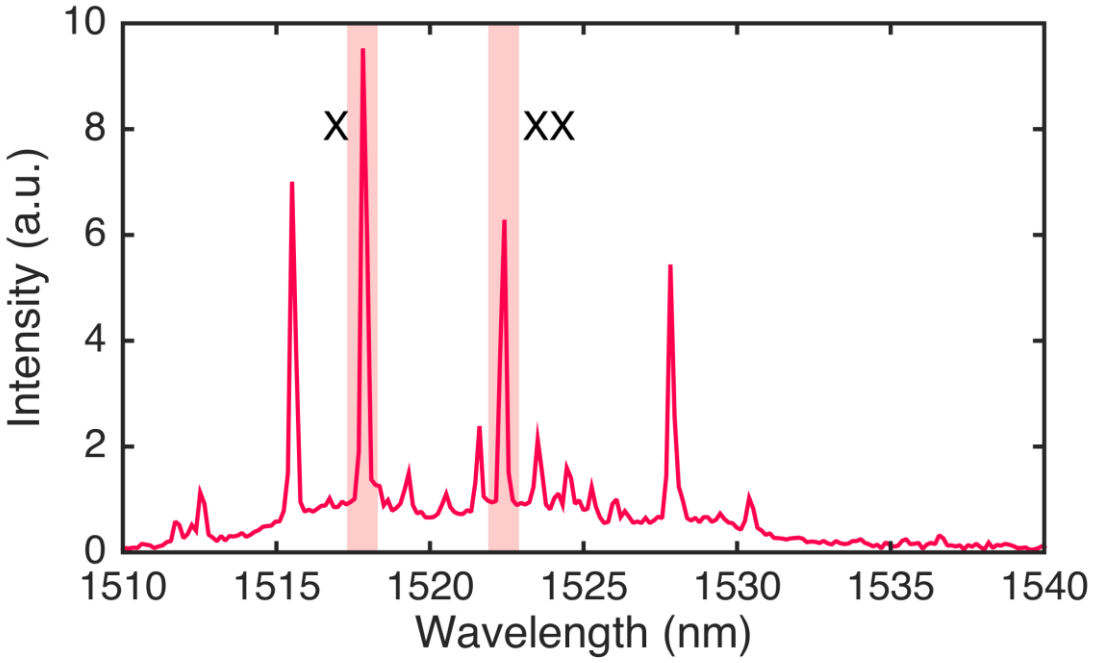

Figure 5.14: The micro-electroluminescence spectrum of the QD used to observe entanglement, with the X and XX transitions shaded for clarity.

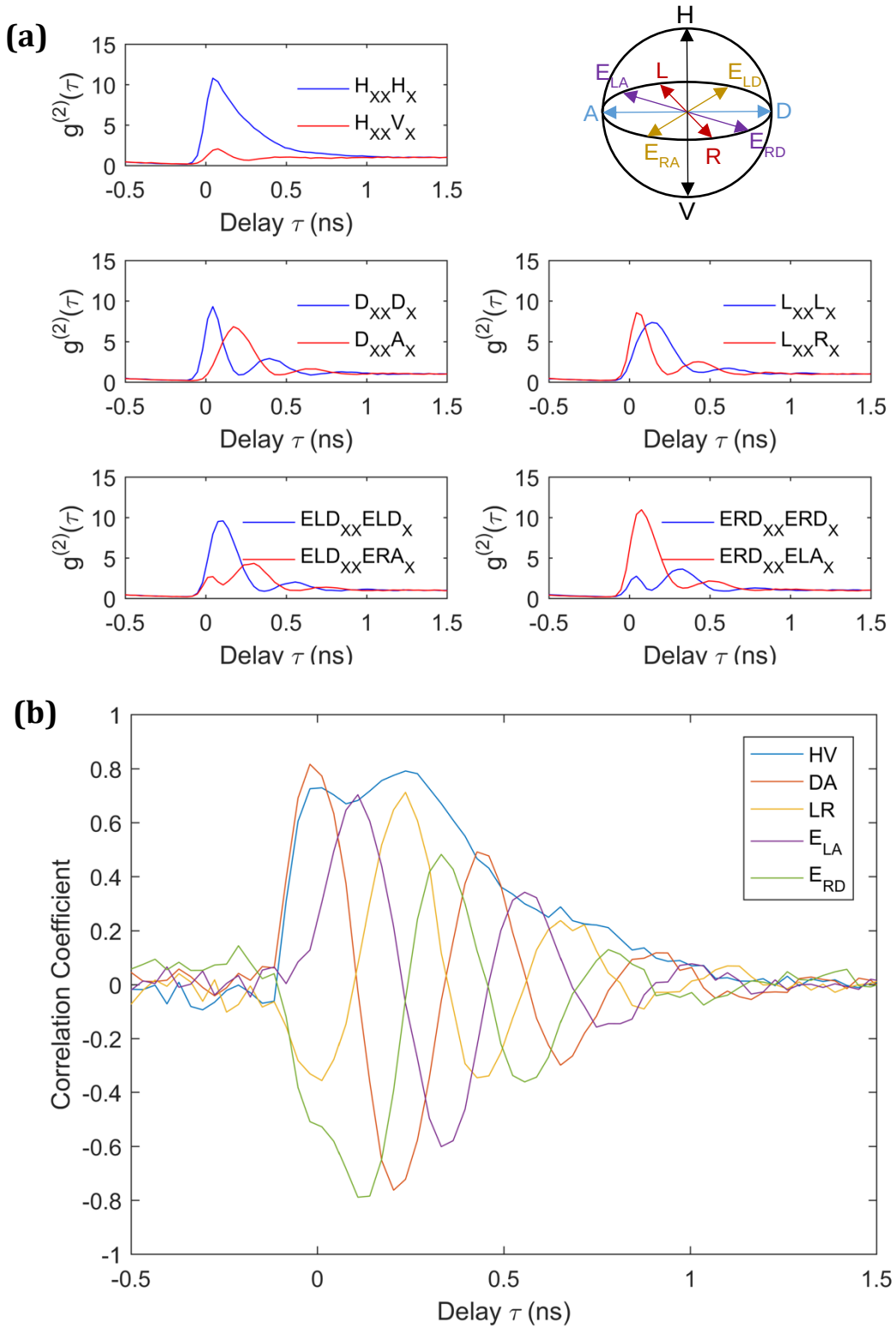

Figure 5.15: (a) Second-order polarisation correlations, as measured by Dr Tina Müller, with 32 ps bins. (b) The correlation coefficients for the five bases (rectilinear, diagonal, circular, E_{LD}-E_{RA}, and E_{LA}-E_{RD}), extracted from the data in (a), again with 32 ps bins.

Using a nominally identical setup to the configuration in Figure 3.10 of Chapter 3 constructed by TM and the author, save for the replacement of the excitation laser with a current source for the QD device and the removal of the dichroic mirrors, the second-order cross-correlations were measured. With a QD found by TM to have a sufficiently low FSS, the ELED was excited under a bias voltage of 1.8 V, chosen as a compromise between light intensity and mitigation of the broad electroluminescence background. The problem of charge segregation persisted through the improvements in the LED design, with the effect that the device would not work at temperatures below 40 K, so the measurements were conducted at this minimum temperature. The exciton photons were at a wavelength of 1517.8 nm with a total intensity of 180 kHz at the SNSPDs, while the XX photons were at a wavelength of 1522.4 nm with an intensity of 90 kHz. Figure 5.14 shows the spectrum of the electroluminescence. Figure 5.15 (a) shows the polarisation-correlation measurements, measured by TM, and Figure 5.15 (b) shows the associated correlation coefficients. Figure 5.16 (a) contains the extracted entanglement fidelity and Figure 5.16 (b) plots the extracted Bell parameter, as interpreted by the author.

The maximum entanglement fidelity for a static state was to the $|\Phi^-\rangle = (|HH\rangle - |VV\rangle)/\sqrt{2}$ Bell state, with a value of 80.63 ± 0.58 %, 53 standard deviations above the classical limit. For a time-evolving state, the peak entanglement fidelity was measured as 83.63 ± 0.47 %, this time being 71 standard deviations above the 50 % classical limit. Due to contributions from reexcited exciton states, the correlation coefficients are degraded close to the zero delay, in part explaining why the Φ^+ state does not correspond to the strongest entangled state measured as expected.

However, to convincingly prove that quantum entanglement is indeed occurring, we require that the CHSH inequality is violated, such that the magnitude of the Bell parameter is greater than 2. Figure 5.16 (b) shows just this; for four of the five values of ϕ considered, S_B exceeds 2. For the static Bell parameters, the peak observed values are 2.180 ± 0.035, 2.054 ± 0.018, 2.126 ± 0.026, and 1.753 ± 0.027, for $\phi = 0$, $\pi/2$, π, and $3\pi/2$, respectively. With the exception of $\phi = 3\pi/2$, these values all surpass the classical limit by at least four standard deviations. The time-evolving Bell parameter reaches a peak value of 2.215 ± 0.020, more than 10 standard deviations above the classical limit, and remains in the CHSH-violating regime for 250 ps. This constitutes persuasive evidence that the emission is entangled, and as such, we have successfully developed a quantum dot-based C-band entangled-light-emitting diode.

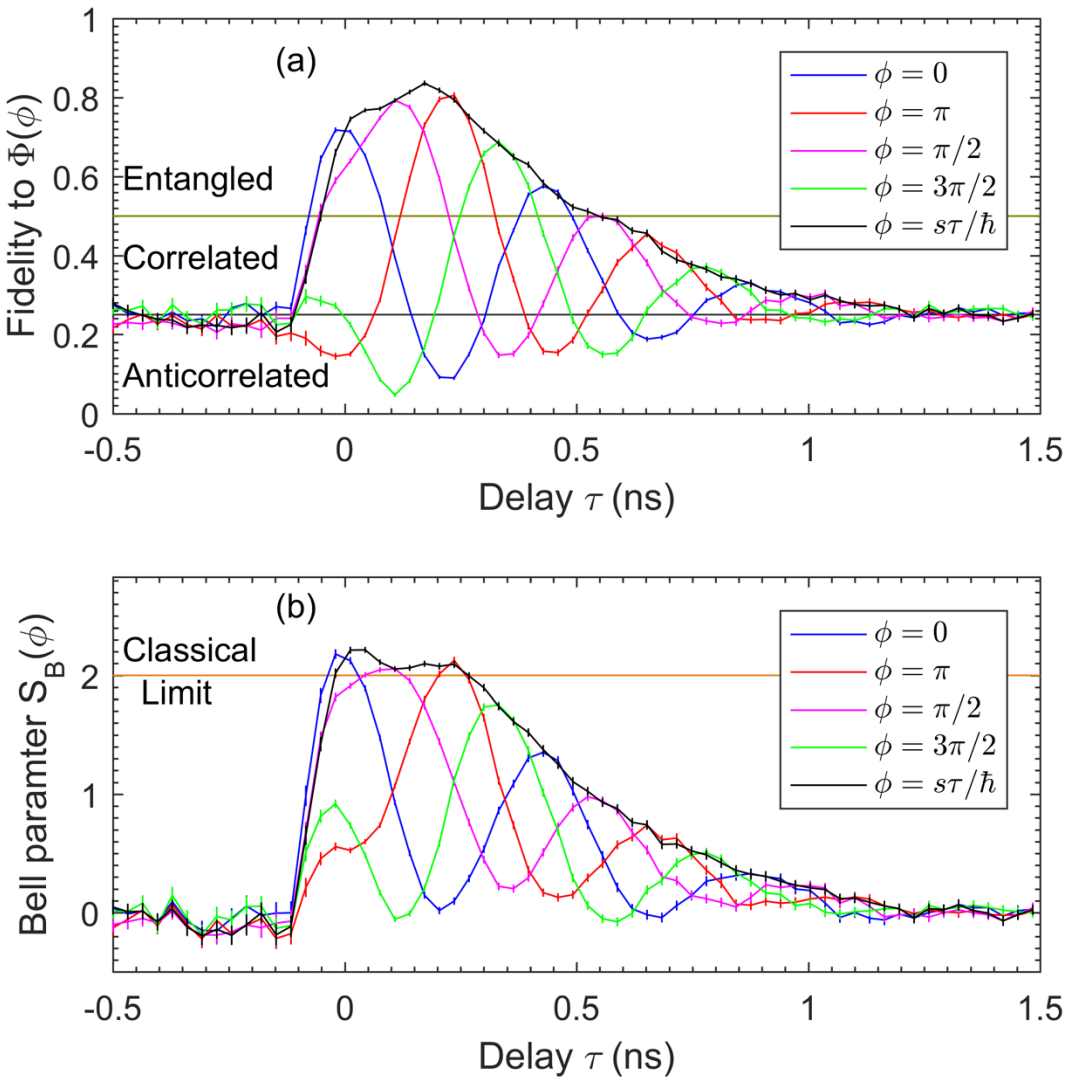

Figure 5.16: Entanglement Fidelity (a) and Bell parameter (b), evaluated from the correlation data in Figure 5.15 according to Equations (3.11) and (3.12), with 32 ps time bins.

5.8 Conclusions

Quantum dots of InAs were successfully grown onto an InP-based semiconductor matrix. The dots emit natively in the fibre telecom O- and C-bands without the need for a great deal of control over the material system's degrees of freedom, such as a strain-relaxing layer above the QDs, bandgap engineering of the surrounding semiconductor matrix, or applying an electric field.

The QDs were then embedded in an InP/AlGaInAs DBR weak planar cavity, providing an improved collection efficiency of the photons. Second-order autocorrelation measurements for an optically-excited cavity-embedded dot reached a $g^{(2)}(0)$ of 0.098 ± 0.037, with a photon intensity of 11 kHz at 1498.6 nm, providing evidence to the Fock state statistics of the telecom-wavelength QD single-photon source.

Investigating an alternate method of dot growth known as droplet epitaxy, anisotropy in the shape of the dots was reduced, lowering the fine structure splittings by a factor of four compared to equivalent S-K QDs, as low as 12.0 ± 2.0 µeV for an optically excited dot. An FSS this low would be sufficient to allow observation of quantum entanglement, as demonstrated in Chapter 3.

The surrounding semiconductor matrix of the QDs was then doped in a *p-i-n* diode structure, with the QDs in the intrinsic layer, such that a single photon LED could be produced. This was successful, and a $g^{(2)}(0)$ of 0.20 ± 0.04 was observed, from an excitonic emission line at 1597.5 nm. As hoped, this LED source also produced pairs of exciton-biexciton polarisation-entangled photons around 1550 nm, similar to the source in Chapter 3, though excited electrically rather than optically, and emitting at a more useful wavelength. The emissions violated Bell's inequality for a time-evolving state for 0.25 ns, with a peak value of 2.215 ± 0.020, and the fidelity to a maximally entangled time-evolving state reached 83.63 ± 0.47 %, for XX and X photons with wavelengths of 1522.4 nm and 1517.8 nm, respectively.

6 Conclusions

6.1 O-band quantum relay

With InAs/GaAs quantum dots grown in the Cavendish Laboratory of the University of Cambridge, and working with researchers at the Cambridge Research Lab of Toshiba Research Europe Limited, a quantum relay (or quantum teleporter) operating in the fibre telecommunication O-band wavelength window (1260-1360 nm) was successfully realised. To our best knowledge, this was the first implementation of a quantum relay with a natively telecom-wavelength sub-Poissonian source of entangled photon pairs.

There are two important features required for successful quantum teleportation: quantum entanglement, which is the resource through which the teleportation is mediated, and a high degree of indistinguishability, necessary for the two-photon Bell state measurement step that heralds each teleportation event. Two photon interference was measured between photons from an InAs/GaAs quantum dot and a laser, spectrally overlapped at 1305 nm, with a raw interference visibility of 60 ± 6 %[36], confirming a high level of indistinguishability between the QD and laser photons. Later, with another QD, entanglement between O-band photons generated from the radiative cascade of the biexciton state to the ground state was observed, with a fidelity of 92.0 ± 0.2 % to the symmetric Bell state $|\Phi^+\rangle = (|HH\rangle + |VV\rangle)/\sqrt{2}$. By considering a time-evolving state $|\Phi(\tau)\rangle = (|HH\rangle + \cos(s\tau/\hbar)\,|VV\rangle)/\sqrt{2}$, incorporating the dynamics of the fine structure splitting s = 9.05 ± 0.01 μeV in the exciton levels, an entanglement fidelity of 96.3 ± 0.3 % could be observed.

Given these results involving two different quantum dots, it proved technically possible to construct a telecom-wavelength quantum relay[105]. It was directly shown that the teleporter is sufficient to implement a BB84 protocol[1] over a quantum channel, demonstrating an average teleportation fidelity of 87.9 ± 1.1 % for input H, V, D, and A polarized states. This is more than 11 standard deviations above the 75 % classical limit, and above the 80 % threshold enabling error correction algorithms for secure QKD[17]. By decreasing the size of the temporal postselection window in the data analysis, a maximum teleportation fidelity of 94.5 ± 2.2 % could be observed, which would contribute as much as 0.385 secure bits per detected three-photon coincidence[16]. By performing quantum process tomography[117,135] of the teleporter, the teleportation fidelity for

an arbitrary input state could be extracted, the average of which was 83.6 ± 1.1 %. The minimum gate fidelities would still be above 72.4 %, the threshold for secure 6-state protocols[17,136].

6.2 C-band entangled LED

Concurrently, alternative QDs of InAs grown on an InP substrate were investigated, grown in the III-V Centre at the University of Sheffield. The reduced lattice mismatch of InAs and InP (3 %) relative to InAs and GaAs (7 %) allowed the emission from excitonic transitions to be extended up to 1550 nm without a great deal of band gap engineering, and other degrees of freedom were left open to control other QD properties, such as coherence and fine structure splitting. Experiments with the dot growth conditions, including variation of the material deposition quantities, growth rates, and growth temperature, allowed dot densities as low as 1 dot μm^{-2} to be achieved. Switching from the Stranski-Krastanow growth mode to the droplet-epitaxy growth mode reduced the fine structure splittings in the QDs by over a factor of four, below the threshold required to experimentally observe entanglement. Second-order autocorrelation measurements confirmed that the QDs were single-photon sources.

During preparation of this thesis, these QDs were successfully incorporated into *p-i-n* doped cavities and processed into LED devices by colleagues at Toshiba Research Europe Ltd, with the single-photon statistics of the electroluminescence again confirmed by autocorrelation measurements. This yielded a QD-based entangled LED, emitting pairs of polarisation-entangled photons from the cascade of the neutral biexciton state, demonstrating entanglement fidelities of 80.63 ± 0.58 % and 83.63 ± 0.47 % to the static Φ^- and time-evolving $\Phi(\tau)$ maximally entangled states, respectively. This represents a considerable advancement to producing a deterministic source of telecom-wavelength entangled photon-pairs.

6.3 Future work

In the short term, the results of this thesis will contribute to improved quantum communication channels, through the development of practical deterministic telecom-wavelength quantum relays. In the longer term, however, these results can be developed into some of the resources required for a distributed quantum computer[4], i.e. quantum computations performed over a non-local quantum network. For example, the need for deterministic sources of entangled qubits[40,96], and the implementation of a quantum repeater[22,4,58].

6.3.1 Improved entanglement

To recap, the entanglement resource in our quantum relay experiment exists in the polarisations of the photons emitted in the biexciton cascade of our quantum dots. Under the conditions of this

thesis' quantum relay, several tens of metres of optical fibre were in use, anchored to a large thermal mass, serving to stabilise the birefringence in the fibres over the timeframe of the experiment. However, in a real-world application, tens of kilometres of fibre will be coupled to an external uncontrolled environment, which will cause the polarisation reference frame between the generation and measurement of a qubit to evolve unpredictably in time. To that end, some means of polarisation stabilisation must be implemented.

Referring to Figure 4.4, it would be possible for Alice to send a well-defined polarisation to Charlie, in order for him to periodically recalibrate the measurement basis of his Bell state analyser. This could be done passively, cutting out the stream of qubits at predetermined intervals for calibration, with the beam at the same wavelength, thus desensitizing the recalibration to any wavelength-dependant birefringence. Or, it could be achieved actively, with the reference beam multiplexed onto the signal beam at a sufficiently close wavelength to experience effectively identical fluctuations. Alternatively, the entanglement could be translated from the polarisation domain into time-bin entanglement, through a pair of Mach-Zehnder interferometers; one placed at Alice and one at Charlie, in the arm receiving Alice's photons. This would desensitize the quantum relay to drifts in the fibre, at the expense of some parasitic losses from use of the interferometers.

Aside from the question of stabilising the measurement reference frame, it is important to minimize the fine structure splitting, to maximize the number of photons exhibiting high fidelity entanglement. Reducing the FSS of the QDs towards the intrinsic FSS (~2 μeV), will have the effect that the window of high fidelity entanglement is extended from about 100 ps (as in Chapter 3 of this thesis) to greater than 500 ps. This could be achieved through numerous techniques in the InAs/GaAs material system, such as an improved strain-relaxing layer grown on top of the dots, both improving the QDs' symmetry and extending their wavelength of emission, or growing larger dots through techniques such as ultraslow or bimodal S-K growth.

However, while the parameter space of InAs/GaAs growth has not been fully explored, it seems that the InAs/InP material system will be more likely to yield low-FSS telecom wavelength QDs. In this thesis, C-band emissions from InAs/InP QDs have exhibited reasonably low fine structure splittings under no externally applied field, and no advanced band-gap engineering or strain relaxing layers. These are similar to splittings seen in Chapters 3 and 4, in O-band emissions from InAs/GaAs dots that have had considerable efforts in engineering of the QD growth, and a large externally applied field. Continuing this line of investigation, exercising the methods discussed for InAs/GaAs QDs[39,46,47,118] as have been applied to shorter-wavelength emitters, it should be possible to develop an InAs/InP QD-based device with minimized FSS in the telecom C-band.

6.3.2 Improved Bell state analyser

The second limiting factor in a practical implementation of a QD-based quantum relay is the Bell state analyser. Performing a Bell state measurement requires a good degree of indistinguishability between the two input modes, which in Chapter 4 of this thesis was limited by the ~100 ps coherence time of the biexciton photons.

An enhanced coherence time could be achieved simply by searching through more QDs, to find the statistically very small sample with high coherence times. More reliable, however, would be to exercise methods of direct excitation of the biexciton state. For example, two-photon excitation, which addresses single electrons making up the biexciton state, could be implemented. This would be instead of flooding the charge environment of the surrounding semiconductor matrix, increasing the resultant charge noise that decreases the coherence of the emitted photons. In this way, it could be possible to generate photons with coherence times towards the transform limit of $\tau_c \leq 2T_1$, potentially several nanoseconds long.

6.3.3 A practical quantum relay

In the quantum relay experiment, we aimed to measure around one teleported photon per hour, which is not close to optimal for any sensible data channel. However, since a teleportation event requires a triple-coincidence, the rate of teleported photons will go up with the cube of the intensity of the QD source. This means that, to go up the nine or ten orders of magnitude from one photon per hour to a megahertz rate, the light source only needs to be around three to four orders of magnitude brighter.

This can be achieved in a number of ways, especially in the InAs/InP system, where there is still a lot of room for improvement. Optimizing the InAs/InP QD growth will likely yield another order of magnitude in brightness, perhaps two. Improving the collection efficiency of the emitted light will also benefit the observed intensity, first by optimizing the cavity design[130], experimenting with optical horn structures or in-situ processing of microlenses on the sample surface, and perhaps investigating in-plane light collection. All this could serve to fill the required gap in intensity needed to see megahertz operation of the quantum relay.

However, it is not good enough to have a real quantum relay running under the conditions of our experiment. Rather than having continuous operation, where the photons are created at random, though anti-bunched, intervals, practical operation would require synchronisation with a clock signal, where the operator would know in which intervals to expect a teleported qubit. For this, a more deterministic photon-pair source is required, which would require running the QD device under pulsed operation, either optically or electrically, synchronised to the aforementioned clock pulse. In an ELED such as seen in Chapter 5, this will require a more

advanced design of the diode to minimize the electrical time constant, to ensure they can apply such a time-varying field sufficiently quickly.

6.3.4 Entanglement swapping

With the advancements described above, as well as some other technological developments, the quantum relay described in this thesis could be modified into a quantum repeater[22,4,58]. Switching Alice's laser for another entangled photon-pair source, with one half of each photon pair being sent to Charlie's Bell state analyser, and the two instances of entanglement can be swapped between the two distinct photon pairs, to the two photons that weren't incident on the Bell state analyser. The requirement of longer XX coherence times is now even stronger, where the time interval over which the Bell state analyser sees identical photons will have roughly halved, all else being the same.

In addition, as a quantum repeater will depend on quadruple coincidences of photons, a quantum memory[137] must be incorporated on one of the measurement arms. Without the ability to coherently store and recall photons on-demand, with count rates and coherence times typically observed from QD entanglement sources in this thesis, we would see less than one quadruple coincidence per year in the time bin of interest. Such a quantum memory could coherently store one of the output photons and recall it once a triple coincidence measurement had occurred, bringing experimental rates closer to the quantum relay implementation of this thesis. However, such a memory would need to operate with near-unity efficiency, and, if incorporated into a quantum channel on the order of tens of kilometres long, would need storage times of around a millisecond. There are numerous schemes being investigated for their use as quantum memories, such as single atoms[138], quantum dots[139], and electromagnetically induced transparency in atomic gas ensembles[140], but developing a quantum memory with a simultaneously high storage time and storage efficiency remains a highly ambitious pursuit. As such, a practical sub-Poissonian telecom-wavelength quantum repeater would represent another considerable technological advancement, and be of considerable scientific interest.

Bibliography

1. C. H. Bennett & G. Brassard, “Quantum Cryptography: Public-Key Distribution and Coin Tossing”, Proc IEEE Int. Conf. Comput. Syst. Signal Process. Bangalore India 175–179 (1984).

2. I. L. Chuang & M. A. Nielsen, "Prescription for experimental determination of the dynamics of a quantum black box", *J. Mod. Opt.* **44,** 2455–2467 (1997).

3. M. Riebe, M. Chwalla, J. Benhelm, H. Häffner, et al., "Quantum teleportation with atoms: quantum process tomography", New J. Phys. 9, 211 (2007).

4. H. J. Kimble, "The quantum internet", *Nature* **453,** 1023–1030 (2008).

5. R. L. Rivest, A. Shamir, & L. Adleman, "A method for obtaining digital signatures and public-key cryptosystems", *Commun. ACM* **21,** 120–126 (1978).

6. C. H. Bennett & D. P. DiVincenzo, "Quantum information and computation", *Nature* **404,** 247–255 (2000).

7. T. D. Ladd, F. Jelezko, R. Laflamme, Y. Nakamura, *et al.*, "Quantum computers", *Nature* **464,** 45–53 (2010).

8. P. W. Shor, "Algorithms for quantum computation: discrete logarithms and factoring", in *Foundations of Computer Science, 1994 Proceedings., 35th Annual Symposium on* 124–134 (1994). doi:10.1109/SFCS.1994.365700

9. L. M. Vandersypen, M. Steffen, G. Breyta, C. S. Yannoni, *et al.*, "Experimental realization of Shor’s quantum factoring algorithm using nuclear magnetic resonance", *Nature* **414,** 883–887 (2001).

10. B. Lanyon, T. Weinhold, N. K. Langford, M. Barbieri, *et al.*, "Experimental demonstration of a compiled version of Shor’s algorithm with quantum entanglement", *Phys. Rev. Lett.* **99,** 250505 (2007).

11. E. Martín-López, A. Laing, T. Lawson, R. Alvarez, *et al.*, "Experimental realization of Shor’s quantum factoring algorithm using qubit recycling", *Nat. Photonics* **6,** 773–776 (2012).

12. L. K. Grover, "A Fast Quantum Mechanical Algorithm for Database Search", in Proceedings of the Twenty-eighth Annual ACM Symposium on Theory of Computing 212–219 (ACM, 1996).

13. K.-A. Brickman, P. Haljan, P. Lee, M. Acton, *et al.*, "Implementation of Grover’s quantum search algorithm in a scalable system", *Phys. Rev. A* **72,** 50306 (2005).

14. P. Walther, K. J. Resch, T. Rudolph, E. Schenck, *et al.*, "Experimental one-way quantum computing", *Nature* **434,** 169–176 (2005).

15. W. K. Wootters & W. H. Zurek, "A single quantum cannot be cloned", *Nature* **299,** 802–803 (1982).

16. P. W. Shor & J. Preskill, "Simple Proof of Security of the BB84 Quantum Key Distribution Protocol", *Phys Rev Lett* **85,** 441–444 (2000).

17. H. F. Chau, "Practical scheme to share a secret key through a quantum channel with a 27.6% bit error rate", *Phys Rev A* **66,** 60302 (2002).

18. K. Patel, J. Dynes, I. Choi, A. Sharpe, *et al.*, "Coexistence of high-bit-rate quantum key distribution and data on optical fiber", *Phys. Rev. X* **2,** 41010 (2012).

19. L. Comandar, M. Lucamarini, B. Fröhlich, J. Dynes, *et al.*, "Quantum key distribution without detector vulnerabilities using optically seeded lasers", *Nat. Photonics* (2016).

20. S. Wang, W. Chen, J.-F. Guo, Z.-Q. Yin, *et al.*, "2 GHz clock quantum key distribution over 260 km of standard telecom fiber", *Opt. Lett.* **37,** 1008–1010 (2012).

21. B. C. Jacobs, T. B. Pittman, & J. D. Franson, "Quantum relays and noise suppression using linear optics", *Phys Rev A* **66,** 52307 (2002).

22. H.-J. Briegel, W. Dür, J. I. Cirac, & P. Zoller, "Quantum repeaters: the role of imperfect local operations in quantum communication", *Phys. Rev. Lett.* **81,** 5932 (1998).

23. T. Miya, Y. Terunuma, T. Hosaka, & T. Miyashita, "Ultimate low-loss single-mode fibre at 1.55 μm", *Electron. Lett.* **15,** 106–108 (1979).

24. D. Payne & W. Gambling, "Zero material dispersion in optical fibres", *Electron. Lett.* **11,** 176–178 (1975).

25. V. Giovannetti, S. Lloyd, & L. Maccone, "Quantum metrology", *Phys. Rev. Lett.* **96,** 10401 (2006).

26. V. Giovannetti, S. Lloyd, & L. Maccone, "Advances in quantum metrology", *Nat. Photonics* **5,** 222–229 (2011).

27. M. B. Ward, M. C. Dean, R. M. Stevenson, A. J. Bennett, *et al.*, "Coherent dynamics of a telecom-wavelength entangled photon source", *Nat. Commun.* **5,** (2014).

28. M. C. Dean, "Single and entangled photon sources using self-assembled InAs quantum dots", (University of Cambridge, 2013).

29. R. M. Stevenson, J. Nilsson, A. J. Bennett, J. Skiba-Szymanska, *et al.*, "Quantum teleportation of laser-generated photons with an entangled-light-emitting diode", *Nat. Commun.* **4,** (2013).

30. W. Wasilewski, P. Kolenderski, & R. Frankowski, "Spectral Density Matrix of a Single Photon Measured", *Phys Rev Lett* **99,** 123601 (2007).

31. Z. Qin, A. S. Prasad, T. Brannan, A. MacRae, *et al.*, "Complete temporal characterization of a single photon", *Light Sci. Appl.* **4,** e298 (2015).

32. J. G. Rarity, P. R. Tapster, & R. Loudon, "Non-classical interference between independent sources", *J Opt B* **7,** 171–175 (2005).

33. E. Knill, R. Laflamme, & G. J. Milburn, "A scheme for efficient quantum computation with linear optics", *Nature* **409,** 46–52 (2001).

34. R. H. Brown, R. Q. Twiss, & others, "Correlation between photons in two coherent beams of light", *Nature* **177,** 27–29 (1956).

35. W. Pauli, "The Connection Between Spin and Statistics", *Phys Rev* **58,** 716–722 (1940).

36. M. Felle, J. Huwer, R. M. Stevenson, J. Skiba-Szymanska, *et al.*, "Interference with a quantum dot single-photon source and a laser at telecom wavelength", *Appl. Phys. Lett.* **107,** (2015).

37. O. Benson, C. Santori, M. Pelton, & Y. Yamamoto, "Regulated and Entangled Photons from a Single Quantum Dot", *Phys Rev Lett* **84,** 2513–2516 (2000).

38. P. Michler, "A Quantum Dot Single-Photon Turnstile Device", *Science* **290,** 2282–2285 (2000).

39. R. M. Stevenson, R. J. Young, P. Atkinson, K. Cooper, *et al.*, "A semiconductor source of triggered entangled photon pairs", *Nature* **439,** 179–182 (2006).

40. M. Müller, S. Bounouar, K. D. Jöns, M. Glässl, & P. Michler, "On-demand generation of indistinguishable polarization-entangled photon pairs", *Nat. Photonics* **8,** 224–228 (2014).

41. R. Rossetti, S. Nakahara, & L. E. Brus, "Quantum size effects in the redox potentials, resonance Raman spectra, and electronic spectra of CdS crystallites in aqueous solution", *J. Chem. Phys.* **79,** 1086–1088 (1983).

42. M. G. Bawendi, M. L. Steigerwald, & L. E. Brus, "The quantum mechanics of larger semiconductor clusters (‘quantum dots’)", Annu. Rev. Phys. Chem. 41, 477–496 (1990).

43. J. R. Petta, A. C. Johnson, J. M. Taylor, E. A. Laird, *et al.*, "Coherent manipulation of coupled electron spins in semiconductor quantum dots", *Science* **309,** 2180–2184 (2005).

44. L. Goldstein, F. Glas, J. Marzin, M. Charasse, & G. Le Roux, "Growth by molecular beam epitaxy and characterization of InAs/GaAs strained-layer superlattices", *Appl. Phys. Lett.* **47,** 1099–1101 (1985).

45. I. N. Stranski & L. Krastanow, "Zur Theorie der orientierten Ausscheidung von Ionenkristallen aufeinander", *Monatshefte Für Chem. Verwandte Teile Anderer Wiss.* **71,** 351–364 (1937).

46. C. Varnava, R. M. Stevenson, J. Nilsson, J. Skiba-Szymanska, *et al.*, "An entangled-LED-driven quantum relay over 1km", *Npj Quantum Inf.* **2,** 16006 (2016).

47. C. L. Salter, R. M. Stevenson, I. Farrer, C. A. Nicoll, *et al.*, "An entangled-light-emitting diode", *Nature* **465,** 594–597 (2010).

48. Z. Yuan, B. E. Kardynal, R. M. Stevenson, A. J. Shields, *et al.*, "Electrically Driven Single-Photon Source", *Science* **295,** 102–105 (2002).

49. J. Nilsson, R. M. Stevenson, K. H. A. Chan, J. Skiba-Szymanska, *et al.*, "Quantum teleportation using a light-emitting diode", *Nat. Photonics* **7,** 311–315 (2013).

50. D. J. Griffiths, "*Introduction to quantum mechanics*", (Cambridge University Press, 2016).

51. P. Bhattacharya, "*Properties of lattice-matched and strained indium gallium arsenide*", (IET, 1993).

52. A. Dargys & J. Kundrotas, "*Handbook on physical properties of Ge, Si, GaAs and InP*", (Science and Encyclopedia Publ., 1994).

53. C. Cohen, B. D. Tannoudji, & F. Laloë, "Quantum mechanics, vol. I and II", *Hermann Wiley* (1977).

54. B. Urbaszek, X. Marie, T. Amand, O. Krebs, *et al.*, "Nuclear spin physics in quantum dots: an optical investigation", *Rev. Mod. Phys.* **85,** 79 (2013).

55. R. Al-Khuzheyri, A. C. Dada, J. Huwer, T. S. Santana, *et al.*, "Resonance fluorescence from a telecom-wavelength quantum dot", *Appl. Phys. Lett.* **109,** 163104 (2016).

56. C. K. Hong, Z. Y. Ou, & L. Mandel, "Measurement of subpicosecond time intervals between two photons by interference", *Phys. Rev. Lett.* **59,** 2044–2046 (1987).

57. C. H. Bennett, G. Brassard, C. Crépeau, R. Jozsa, *et al.*, "Teleporting an unknown quantum state via dual classical and Einstein-Podolsky-Rosen channels", *Phys Rev Lett* **70,** 1895–1899 (1993).

58. K. Azuma, K. Tamaki, & H.-K. Lo, "All-photonic quantum repeaters", *Nat. Commun.* **6,** (2015).

59. D. Bouwmeester, J.-W. Pan, K. Mattle, M. Eibl, *et al.*, "Experimental quantum teleportation", *Nature* **390,** 575–579 (1997).

60. C. Santori, D. Fattal, J. Vukovic, G. S. Solomon, & Y. Yamamoto, "Indistinguishable photons from a single-photon device", *Nature* **419,** 594–597 (2002).

61. H. de Riedmatten, I. Marcikic, W. Tittel, H. Zbinden, & N. Gisin, "Quantum interference with photon pairs created in spatially separated sources", *Phys Rev A* **67,** 22301 (2003).

62. T. Legero, T. Wilk, M. Hennrich, G. Rempe, & A. Kuhn, "Quantum Beat of Two Single Photons", *Phys Rev Lett* **93,** 70503 (2004).

63. A. Bennett, R. Patel, C. Nicoll, D. Ritchie, & A. Shields, "Interference of dissimilar photon sources", *Nat. Phys.* **5,** 715–717 (2009).

64. V. Josse, M. Sabuncu, N. J. Cerf, G. Leuchs, & U. L. Andersen, "Universal Optical Amplification without Nonlinearity", *Phys Rev Lett* **96,** 163602 (2006).

65. A. K. Ekert, "Quantum cryptography based on Bell's theorem", *Phys Rev Lett* **67,** 661–663 (1991).

66. N. Gisin, G. Ribordy, W. Tittel, & H. Zbinden, "Quantum cryptography", *Rev Mod Phys* **74,** 145–195 (2002).

67. W.-Y. Hwang, "Quantum Key Distribution with High Loss: Toward Global Secure Communication", *Phys Rev Lett* **91,** 57901 (2003).

68. T. Legero, T. Wilk, A. Kuhn, & G. Rempe, "Time-resolved two-photon quantum interference", *Appl. Phys. B Lasers Opt.* **77,** 797–802 (2003).

69. M. A. Nielsen & I. L. Chuang, "*Quantum computation and quantum information*", (Cambridge university press, 2010).

70. D. A. B. Miller, D. S. Chemla, T. C. Damen, A. C. Gossard, *et al.*, "Band-edge electroabsorption in quantum well structures: the quantum-confined Stark effect", *Phys. Rev. Lett.* **53,** 2173 (1984).

71. S.-S. Li & J.-B. Xia, "Quantum-confined Stark effects of InAs/GaAs self-assembled quantum dot", *J. Appl. Phys.* **88,** 7171–7174 (2000).

72. J. Schaibley, A. Burgers, G. McCracken, D. Steel, *et al.*, "Direct detection of time-resolved Rabi oscillations in a single quantum dot via resonance fluorescence", *Phys. Rev. B* **87,** 115311 (2013).

73. A. C. Dada, T. S. Santana, R. N. Malein, A. Koutroumanis, *et al.*, "Indistinguishable single photons with flexible electronic triggering", *Optica* **3,** 493–498 (2016).

74. A. Einstein, B. Podolsky, & N. Rosen, "Can quantum-mechanical description of physical reality be considered complete?", *Phys. Rev.* **47,** 777 (1935).

75. J. S. Bell, "*On the einstein podolsky rosen paradox*", (1964).

76. J. F. Clauser, M. A. Horne, A. Shimony, & R. A. Holt, "Proposed experiment to test local hidden-variable theories", *Phys. Rev. Lett.* **23,** 880 (1969).

77. N. Brunner, D. Cavalcanti, S. Pironio, V. Scarani, & S. Wehner, "Bell nonlocality", *Rev Mod Phys* **86,** 419–478 (2014).

78. B. G. Christensen, K. T. McCusker, J. B. Altepeter, B. Calkins, *et al.*, "Detection-Loophole-Free Test of Quantum Nonlocality, and Applications", *Phys Rev Lett* **111,** 130406 (2013).

79. M. Giustina, A. Mech, S. Ramelow, B. Wittmann, *et al.*, "Bell violation using entangled photons without the fair-sampling assumption", *Nature* **497,** 227–230 (2013).

80. G. Weihs, T. Jennewein, C. Simon, H. Weinfurter, & A. Zeilinger, "Violation of Bell's Inequality under Strict Einstein Locality Conditions", *Phys Rev Lett* **81,** 5039–5043 (1998).

81. T. Scheidl, R. Ursin, J. Kofler, S. Ramelow, *et al.*, "Violation of local realism with freedom of choice", *Proc. Natl. Acad. Sci.* **107,** 19708–19713 (2010).

82. B. Hensen, H. Bernien, A. E. Dreau, A. Reiserer, *et al.*, "Loophole-free Bell inequality violation using electron spins separated by 1.3 kilometres", *Nature* **526,** 682–686 (2015).

83. M. Giustina, M. A. M. Versteegh, S. Wengerowsky, J. Handsteiner, *et al.*, "Significant-Loophole-Free Test of Bell's Theorem with Entangled Photons", *Phys Rev Lett* **115,** 250401 (2015).

84. L. K. Shalm, E. Meyer-Scott, B. G. Christensen, P. Bierhorst, et al., "Strong Loophole-Free Test of Local Realism", Phys Rev Lett 115, 250402 (2015).

85. D. Bouwmeester, A. Ekert, A. Zeilinger, & others, "*The physics of quantum information*", **3,** (Springer, Berlin, 2000).

86. J. Cirac, A. Ekert, S. Huelga, & C. Macchiavello, "Distributed quantum computation over noisy channels", *Phys. Rev. A* **59,** 4249 (1999).

87. D. Collins, N. Gisin, & H. De Riedmatten*, "Quantum relays for long distance quantum cryptography", *J. Mod. Opt.* **52,** 735–753 (2005).

88. H. de Riedmatten, I. Marcikic, W. Tittel, H. Zbinden, *et al.*, "Long Distance Quantum Teleportation in a Quantum Relay Configuration", *Phys Rev Lett* **92,** 47904 (2004).

89. I. Marcikic, H. de Riedmatten, W. Tittel, H. Zbinden, & N. Gisin, "Long-distance teleportation of qubits at telecommunication wavelengths", *Nature* **421,** 509–513 (2003).

90. H. Hübel, M. R. Vanner, T. Lederer, B. Blauensteiner, *et al.*, "High-fidelity transmission of polarization encoded qubits from an entangled source over 100 km of fiber", *Opt Express* **15,** 7853–7862 (2007).

91. T. Zhong, X. Hu, F. N. C. Wong, K. K. Berggren, *et al.*, "High-quality fiber-optic polarization entanglement distribution at 1.3 μm telecom wavelength", *Opt Lett* **35,** 1392–1394 (2010).

92. K. De Greve, L. Yu, P. L. McMahon, J. S. Pelc, *et al.*, "Quantum-dot spin–photon entanglement via frequency downconversion to telecom wavelength", *Nature* **491,** 421–425 (2012).

93. A. Orieux, A. Eckstein, A. Lemaître, P. Filloux, *et al.*, "Direct Bell States Generation on a III-V Semiconductor Chip at Room Temperature", *Phys Rev Lett* **110,** 160502 (2013).

94. F. Bussières, C. Clausen, A. Tiranov, B. Korzh, *et al.*, "Quantum teleportation from a telecom-wavelength photon to a solid-state quantum memory", *Nat Photon* **8,** 775–778 (2014).

95. X.-L. Wang, X.-D. Cai, Z.-E. Su, M.-C. Chen, *et al.*, "Quantum teleportation of multiple degrees of freedom of a single photon", *Nature* **518,** 516–519 (2015).

96. M. B. Ward, O. Z. Karimov, D. C. Unitt, Z. L. Yuan, et al., "On-demand single-photon source for 1.3 μm telecom fiber", Appl. Phys. Lett. 86, (2005).

97. C. Zinoni, B. Alloing, C. Monat, V. Zwiller, *et al.*, "Time-resolved and antibunching experiments on single quantum dots at 1300 nm", *Appl. Phys. Lett.* **88,** 131102 (2006).

98. M. Benyoucef, M. Yacob, J. P. Reithmaier, J. Kettler, & P. Michler, "Telecom-wavelength (1.5 μm) single-photon emission from InP-based quantum dots", Appl. Phys. Lett. 103, (2013).

99. W. Pauli, "Über den Zusammenhang des Abschlusses der Elektronengruppen im Atom mit der Komplexstruktur der Spektren", *Z. Für Phys.* **31,** 765–783 (1925).

100. D. Gammon, E. S. Snow, B. V. Shanabrook, D. S. Katzer, & D. Park, "Fine Structure Splitting in the Optical Spectra of Single GaAs Quantum Dots", *Phys Rev Lett* **76,** 3005–3008 (1996).

101. C. Santori, D. Fattal, M. Pelton, G. S. Solomon, & Y. Yamamoto, "Polarization-correlated photon pairs from a single quantum dot", *Phys Rev B* **66,** 45308 (2002).

102. S. Ulrich, S. Strauf, P. Michler, G. Bacher, & A. Forchel, "Triggered polarization-correlated photon pairs from a single CdSe quantum dot", *Appl. Phys. Lett.* **83,** 1848–1850 (2003).

103. B. S. Cirel'son, "Quantum generalizations of Bell's inequality", *Lett. Math. Phys.* **4,** 93–100 (1980).

104. J. Skiba-Szymanska, R. M. Stevenson, C. Varnava, M. Felle, et al., "Universal Growth Scheme for Quantum Dots with Low Fine-Structure Splitting at Various Emission Wavelengths", *Phys Rev Appl* **8,** 014013 (2017).

105. J. Huwer, M. Felle, R. M. Stevenson, J. Skiba-Szymanska, et al., "A Quantum-Dot-Based Telecommunication-Wavelength Quantum Relay", *Phys Rev Appl* **8,** 024007 (2017).

106. M. Fujiwara, H. Ishizuka, S. Miki, T. Yamashita, *et al.*, "Field demonstration of quantum key distribution in the Tokyo QKD Network", in *International Quantum Electronics Conference* I403 (Optical Society of America, 2011).

107. R. Ursin, T. Jennewein, M. Aspelmeyer, R. Kaltenbaek, *et al.*, "Communications: Quantum teleportation across the Danube", *Nature* **430,** 849–849 (2004).

108. R. Valivarthi, Q. Zhou, G. H. Aguilar, V. B. Verma, *et al.*, "Quantum teleportation across a metropolitan fibre network", *Nat. Photonics* **10,** 676–680 (2016).

109. Q. Sun, Y. Mao, S. Chen, W. Zhang, et al., "Quantum teleportation with independent sources over an optical fibre network", arXiv:1602.07081 (2016).

110. X.-M. Jin, J.-G. Ren, B. Yang, Z.-H. Yi, *et al.*, "Experimental free-space quantum teleportation", *Nat. Photonics* **4,** 376–381 (2010).

111. Z. Merali & others, "The quantum space race", *Nature* **492,** 22–25 (2012).

112. X.-S. Ma, T. Herbst, T. Scheidl, D. Wang, *et al.*, "Quantum teleportation over 143 kilometres using active feed-forward", *Nature* **489,** 269–273 (2012).

113. J.-L. Smirr, R. Frey, E. Diamanti, R. Alléaume, & I. Zaquine, "Intrinsic limitations to the quality of pulsed spontaneous parametric downconversion sources for quantum information applications", *JOSA B* **28,** 832–841 (2011).

114. H.-K. Lo & H. F. Chau, "Unconditional security of quantum key distribution over arbitrarily long distances", Science 283, 2050–2056 (1999).

115. B. Alloing, C. Zinoni, V. Zwiller, L. H. Li, *et al.*, "Growth and characterization of single quantum dots emitting at 1300 nm", *Appl. Phys. Lett.* **86,** 101908–101908 (2005).

116. C. H. Bennett, F. Bessette, G. Brassard, L. Salvail, & J. Smolin, "Experimental quantum cryptography", *J. Cryptol.* **5,** 3–28 (1992).

117. J. B. Altepeter, D. F. V. James, & P. G. Kwiat, "Quantum State Tomography", (2004).

118. C. L. Salter, "Development and application of an entangled-light-emitting diode", (University of Cambridge, 2012).

119. A. Shields, R. M. Stevenson, R. M. Thompson, Z. Yuan, & B. Kardynal, "Generation of single photons using semiconductor quantum dots", in Nano-Physics and Bio-Electronics 111–146 (Elsevier, 2002).

120. M. B. Ward, P. M. Intallura, C. M. Natarajan, R. H. Hadfield, *et al.*, "Biexciton cascade in telecommunication wavelength quantum dots", *J. Phys. Conf. Ser.* **210,** 12036 (2010).

121. M. B. Ward, T. Farrow, P. See, Z. L. Yuan, *et al.*, "Electrically driven telecommunication wavelength single-photon source", *Appl. Phys. Lett.* **90,** 63512 (2007).

122. K. Takemoto, Y. Sakuma, S. Hirose, T. Usuki, *et al.*, "Non-classical photon emission from a single InAs/InP quantum dot in the 1.3-μm optical-fiber band", *Jpn. J. Appl. Phys.* **43,** L993 (2004).

123. T. Miyazawa, K. Takemoto, Y. Sakuma, S. Hirose, *et al.*, "Single-photon generation in the 1.55-μm optical-fiber band from an InAs/InP quantum dot", *Jpn. J. Appl. Phys.* **44,** L620 (2005).

124. K. Takemoto, Y. Sakuma, S. Hirose, T. Usuki, & N. Yokoyama, "Observation of Exciton Transition in 1.3–1.55 μm Band from Single InAs/InP Quantum Dots in Mesa Structure", *Jpn. J. Appl. Phys.* **43,** L349 (2004).

125. L. He, M. Gong, C.-F. Li, G.-C. Guo, & A. Zunger, "Highly Reduced Fine-Structure Splitting in InAs / InP Quantum Dots Offering an Efficient On-Demand Entangled 1.55-μm Photon Emitter", Phys. Rev. Lett. 101, (2008).

126. M. Gong, K. Duan, C.-F. Li, R. Magri, et al., "Electronic structure of self-assembled InAs⁄InP quantum dots: Comparison with self-assembled InAs⁄GaAs quantum dots", Phys. Rev. B 77, (2008).

127. Y. Arakawa, "Multidimensional quantum well laser and temperature dependence of its threshold current", *Appl. Phys. Lett.* **40,** 939 (1982).

128. S. Yoon, Y. Moon, T.-W. Lee, E. Yoon, & Y. D. Kim, "Effects of As/P exchange reaction on the formation of InAs/InP quantum dots", *Appl. Phys. Lett.* **74,** 2029 (1999).

129. T. Mano, K. Watanabe, S. Tsukamoto, H. Fujioka, *et al.*, "New self-organized growth method for InGaAs quantum dots on GaAs (001) using droplet epitaxy", *Jpn. J. Appl. Phys.* **38,** L1009 (1999).

130. G. Björk, S. Machida, Y. Yamamoto, & K. Igeta, "Modification of spontaneous emission rate in planar dielectric microcavity structures", *Phys Rev A* **44,** 669–681 (1991).

131. J. McCaulley, V. Donnelly, M. Vernon, & I. Taha, "Temperature dependence of the near-infrared refractive index of silicon, gallium arsenide, and indium phosphide", *Phys. Rev. B* **49,** 7408 (1994).

132. R. Young, R. Stevenson, A. Shields, P. Atkinson, *et al.*, "Inversion of exciton level splitting in quantum dots", *Phys. Rev. B* **72,** 113305 (2005).

133. C.-H. Chen, U. Gösele, & T. Tan, "Dopant diffusion and segregation in semiconductor heterostructures: Part 1. Zn and Be in III-V compound superlattices", *Appl. Phys. Mater. Sci. Process.* **68,** 9–18 (1999).

134. P. R. Berger, S. Chu, R. Logan, E. Byrne, *et al.*, "Substrate orientation effects on dopant incorporation in InP grown by metalorganic chemical vapor deposition", *J. Appl. Phys.* **73,** 4095–4097 (1993).

135. D. F. V. James, P. G. Kwiat, W. J. Munro, & A. G. White, "Measurement of qubits", *Phys Rev A* **64,** 52312 (2001).

136. D. Bruß, "Optimal Eavesdropping in Quantum Cryptography with Six States", *Phys Rev Lett* **81,** 3018–3021 (1998).

137. A. I. Lvovsky, B. C. Sanders, & W. Tittel, "Optical quantum memory", *Nat. Photonics* **3,** 706–714 (2009).

138. H. P. Specht, C. Nölleke, A. Reiserer, M. Uphoff, *et al.*, "A single-atom quantum memory", *Nature* **473,** 190–193 (2011).

139. A. B. de la Giroday, N. Sköld, R. M. Stevenson, I. Farrer, *et al.*, "Exciton-spin memory with a semiconductor quantum dot molecule", *Phys. Rev. Lett.* **106,** 216802 (2011).

140. M. Fleischhauer & M. D. Lukin, "Quantum memory for photons: Dark-state polaritons", *Phys. Rev. A* **65,** 22314 (2002).